THE NATURE OF VOLATILES ON 4-VESTA: CLUES FROM APATITE IN EUCRITES

Adam Robert Sarafian

(Under the direction of Michael F. Roden)

ABSTRACT

Eucrites are basaltic and gabbroic meteorites that are paired with howardites and

diogenites, all of which are thought to be from the asteroid 4-Vesta. Because eucrites are

volatile-depleted, and this volatile-depletion is poorly understood, I studied the volatiles fluorine,

chlorine and water in eucritic apatite. Partition coefficients were used to estimate the ratio of the

volatiles (hydroxyl vs. fluorine vs. chlorine) in the coexisting melt and textures of apatite and

mineral associations were used to determine the conditions of apatite crystallization. The

majority of the apatite is nearly pure fluorapatite, occurs in mesostasis, and probably crystallized

from a degassed magma, similar to lunar mare basalt magma. Chlorine-rich apatites in the GRA

98098 meteorite and vein apatites associated with pyroxene and troilite in the Juvinas meteorite

may have crystallized from a high temperature fluid.

Index words: apatite, volatile, eucrite, water, Vesta, HED, meteorite

THE NATURE OF VOLATILES ON 4-VESTA: CLUES FROM APATITE IN EUCRITES

Adam Robert Sarafian
B.S., University of Georgia, 2009

A Thesis Submitted to the Graduate Faculty of the University of Georgia in Partial Fulfillment of the Requirements for the Degree

Master of Science

Athens, Georgia

2012

THE NATURE OF VOLATILES ON 4-VESTA: CLUES FROM APATITE IN EUCRITES

By Adam Robert Sarafian

Major Professor: Michael F. Roden

Committee: Alberto E. Patiño-Douce

Douglas Crowe

Electronic Version Approved:

Maureen Grasso Dean of the Graduate School The University of Georgia December 2012

ACKNOWLEDGEMENTS

First, I would like to thank Mike Roden for his tremendous amount of help throughout this project. Alberto Patiño-Douce and Doug Crowe are thanked for their assistance while working on this project. C. Fleisher is thanked for his assistance in EMP data acquisition, camaraderie, and patience. I would like to thank B. Monteleone and N. Shimizu for assistance with SIMS analysis. I would like to especially thank N. Shimizu for funding the initial testing and results acquired by SIMS. P. Schroeder and J. Shields are thanked for assistance with SEM work. I thank E. Fritzsch, J. Gret, and D. Crowe for their donation of standards. I thank the American Museum of Natural History and J. Boesenburg for allocating samples. I thank NASA, the Johnson Space Center curatorial staff and K. Righter for allocation of Antarctic meteorites. F. McCubbin, J. Boyce, J-A Barrat, and P. Warren are thanked for their numerous conversations and insights into analytical techniques and various theories regarding Vesta/eucrites. C. Schrader is thanked for his guidance and for establishing the study of apatite at UGA. D. Susina, S. Harris, S. Singerling, and graduate/undergraduate students from the University of Georgia and the University of Tennessee are thanked for their enlightening conversations. I would like to thank C. Foggin and the UGA Athletic Association for funding during the study time. Grant-in-Aid of Research from Sigma Xi, the NASA Cosmochemistry program, the Geological Society of America, the University of Georgia Geology department, and the University of Georgia disability services provided funding during the writing of this thesis.

TABLE OF CONTENTS

Ackno	ledgements	IV
List o	ables	VI
List o	igures	VII
1	NTRODUCTION	1
	1.1 Vesta	1
	1.2 Distinguishing features of eucrites	2
	1.3 Petrology and geochemistry of eucrites	4
	1.4 Summary of the study	6
2	THE NAURE OF VOLATILES ON 4-VESTA: CLUES FROM APATITE IN	
EUCF	TES	
	2.1 Abstract	14
	2.2 Introduction	15
	2.3 Sample selection	17
	2.4 Analytical Methods	18
	2.5 Results	23
	2.6 Discussion	31
	2.7 Eucrite apatite compared to lunar apatites	40
	2.8 Conclusions	42
REFE	ENCES	54
APPE	DIX	71

LIST OF TABLES

Table 2.1 Representative apatite compositions measured by electron microprobe	50
Table 2.2 Apatite volatile concentrations determined by SIMS	53

LIST OF FIGURES

Figure 1.1 Location of Vesta relative to the orbits of Mars and Earth	8
Figure 1.2 Wavelength vs. Relative reflectance	9
Figure 1.3 Δ^{17} O vs. δ^{18} O	10
Figure 1.4 Mn vs. Fe in pyroxene	11
Figure 1.5 Plot of bulk rock K vs. Th	12
Figure 1.6 Bulk rock Hf vs. Sc for monomict and unbrecciated eucrites and Pasamonte	13
Figure 2.1 Bulk rock Hf vs. Sc for monomict and unbrecciated eucrites and Pasamonte	44
Figure 2.2 Plot of SIMS measurements of OH in apaite, plagioclase and pyroxene	45
Figure 2.3 Backscatter electron images of eucrites	46
Figure 2.4 Backscatter electron images of eucrites	47
Figure 2.5 Truncated ternary diagram of atomic proportions of F, Cl, & OH in the X site	of
apatite	48
Figure 2.6 Truncated ternary diagram of atomic proportions of F, Cl, & OH in the X site	of
apatite	49

Chapter 1:

INTRODUCTION

In the following sections I review information on the asteroid 4-Vesta, describe the distinguishing features of eucrites (basaltic meteorites), their link to Vesta, geochemical trends, and metamorphism, and finally give a brief overview of the work I have done in the past two years. This section serves to introduce the actual thesis work, which is reviewed starting in Chapter 2, and which will be submitted as a manuscript to *Meteoritics and Planetary Science*

1.1 Vesta

Heinrich Olbers discovered Vesta, the fourth asteroid, in March of 1807. It is the largest asteroid known with a metallic core and rocky mantle/crust in the main asteroid belt (Figure 1.1) (Asmar et al., 2012; Rayman et al., 2006). At ~1/3 the size of the Moon (R_{Vesta} = 265 km), Vesta makes up ~9% of the mass of the asteroid belt. Vesta is thought to be the parent body of the howardites, eucrites, and diogenites (HEDs), based on reflectance spectra (Figure 1.2) (e.g., Consolmango and Drake, 1977) and the mesosiderites, based on oxygen isotope compositions (Greenwood et al., 2006). Eucrites are basalts and gabbros, diogenites are orthopyroxenites, howardites are breccias containing both lithologies, and mesosiderites are a mixture of FeNi metal and basaltic material (Papike, 1998).

Dawn, a NASA Discovery-Class mission, entered orbit around Vesta in late summer 2011. While at Vesta, Dawn's primary mission is to map the surface features of Vesta with a visible light framing camera (FC), but Dawn is also equipped with a visible and near infrared spectrometer (VIR) to determine surface mineralogy and a wide angle gamma ray and neutron

spectrometer (GRaND) to measure the surface composition of large areas. Russell et al. (2012) summarized the accomplishments of the Dawn mission, which includes a map of most of the asteroid made with input from all three instruments, key results include VIR evidence that links different surface mineralogies on Vesta to howardites, eucrites and diogenites, but not mesosiderites, and from Doppler effects, a model for the interior structure of Vesta.

1.2 Distinguishing features of eucrites

Stony meteorites are classified into two groups, achondrites and chondrites. Achondrites are meteorites that lack chondrules, which are spheroids of quenched or crystallized melt. Achondrites can be placed into several groups that include HEDs (discussed below), Martian meteorites (relatively young basalts and ultramafic rocks), lunar meteorites (mostly breccias containing older anorthositic material and younger basaltic material), acapulcoites/lodranites (extrusive/intrusive chondritic partial melts which include plagioclase, olivine, pyroxene, and metal), angrites (basalts containing plagioclase, pyroxene, and olivine, $f_{O2} \sim QFM$), brachinites (meteoritic dunites), aubrites (orthopyroxene/enstatite breccias), ureilites (olivine-pigeonite rocks), winonaites (olivine, pyroxene, sulfide, and metal aggregates) and several ungrouped meteorites (e.g., NWA 011, and GRA 06128/9).

An important tool for classifying achondrites is oxygen isotope composition (e.g., Clayton, 1993, 1996, 2003; Clayton and Mayeda, 1983; Clayton et al., 1976; Greenwood et al., 2005; Scott et al., 2009). Various achondrite groups define fractionation lines parallel to, but distinct from, the terrestrial fractionation line, e.g., the angrites fractionation line (AFL) plots parallel to the eucrite fractionation line (EFL) and the terrestrial fractionation line (TFL) (Figure 1.3). Most HEDs are thought to be from the same parent body because they define an oxygen

isotope fractionation line parallel to, but distinct from, the terrestrial fractionation line, with $\Delta^{17}O$ = 0.239 ± 0.007‰, where $\Delta^{17}O$ is the difference in $d^{17}O$ of the sample and the TFL (Figure 1.3) (Greenwood et al., 2005). Some eucrites have $\Delta^{17}O$ values that are distinctive compared to most eucrites (e.g., Pasamonte $\Delta^{17}O$ = -0.2‰ and Ibitira $\Delta^{17}O$ = -0.1‰ compared to the eucrite fractionation line)(Greenwood et al., 2005), suggesting that these eucrites came from different parent bodies (Greenwood et al., 2005; Scott et al., 2009; Wiechert et al., 2004). Other achondrites have $\Delta^{17}O$ values that range from $\Delta^{17}O$ = ~0.30‰ for Martian rocks, $\Delta^{17}O$ = ~0‰ for lunar rocks, to $\Delta^{17}O$ = ~1.20‰ for ureilites (Clayton, 1996).

The Mn/Fe ratio in pyroxene is also used to differentiate between achondrite groups (Figure 1.4) (Goodrich and Delaney, 2000; Karner et al., 2006; Mittlefehldt, 1987; Mittlefehldt, 2005; Papike, 1998; Papike et al., 2003). Because Mn and Fe are geochemically similar, igneous processes do not generally fractionate Mn from Fe (Papike, 1998). However core formation or bulk depletion in volatile elements can lead to distinct Mn/Fe ratios in the silicate portion of a planetary body and result in distinct ratios in pyroxenes. For example during core formation Fe is concentrated in the core; as a siderophile element, Mn follows Fe. However, the relative amount of Mn that follows Fe into the core of a differentiated body is pressure dependent, so distinct Mn/Fe ratios can characterize planetary or asteroid mantles in differentiated bodies (Figure 1.4). At low pressures Mn is less siderophile. Thus, in a small body (like Vesta) Mn will not enter the core as readily, and the Mn/Fe ratio in the mantle (dunitic diogenites) and crust (eucrites) will be relatively high (Drake et al., 1989; Goodrich and Delaney, 2000). On the contrary, for a larger body, like Earth, Mn would behave more siderophile-like and follow Fe into the core. Thus the terrestrial mantle should have a relatively low Mn/Fe ratio. Secondly, Mn is slightly more volatile than Fe (Lodders, 2003), consequently a relatively low Mn/Fe ratio in pyroxene can

reflect a bulk planetary depletion in volatile elements, as in the case for pyroxenes from the Moon.

1.3 Petrology and geochemistry of eucrites

Eucrites are meteorites that sample some of the first differentiated bodies in the solar system (Greenwood et al., 2005; Misawa et al., 2005; Mittlefehldt, 2005; Scott et al., 2009; Wiechert et al., 2004). Based on their petrography and bulk rock composition, most basaltic eucrites are basalts and but some more SiO₂-rich eucrites are basaltic andesites (Warren et al., 2009). "Cumulate" eucrites are the intrusive equivalents of these rocks. Eucrites typically consist of plagioclase and pigeonite, with trace troilite, ilmenite, silica, spinel, merrillite, apatite, zircon, and baddeleyite.

Eucrites are generally considered to be volatile depleted (Papike, 1998). The K/Th or K/U ratio is an indicator of the volatile content of the parent body of a meteorite. This generalization follows from the relative volatility of K, and the refractory nature of U and Th. All three elements are lithophile and highly incompatible during igneous processes, and thus are not strongly fractionated during planetary differentiation or magmatism. The K/Th ratios for the Mercurian and Martian surfaces are ~5,500, eucrites have ratios of ~1000, the lunar surface has a much lower K/Th ratio, ~360 (Figure 1.5), and the terrestrial bulk silicate earth has a ratio of ~2570 (Newsom, 1995). The giant impact that formed the Moon (Newsom and Taylor, 1989) is likely the cause of the low K/Th ratio of that body. The low K/Th ratio seen in eucrites establishes that Vesta is probably depleted in volatiles as well, but perhaps not as depleted as the Moon (Mittlefehldt, 1987; Righter and Drake, 1997).

1.3.1 Stannern trend and Nuevo Laredo trend/main group eucrites

Two geochemical trends have been recognized in eucrites, the Stannern trend and the Nuevo Laredo trend/main group (Figure 1.6). The Nuevo Laredo trend/main group shows a positive correlation between incompatible elements, suggesting it is a crystal fractionation trend (Stolper, 1977). The eucrites of the Stannern trend are enriched in highly incompatible trace elements, and these highly incompatible elements do not closely correlate with major element indicators of crystal fractionation (Barrat et al., 2007). Over the past 35 years that eucrites have been studied in detail, the petrologic conditions under which eucrites formed has remained controversial. Stolper (1977) showed that Nuevo Laredo trend/main group eucrites could be explained by crystal fractionation from a basaltic melt. Stolper (1977) went on to suggest that Stannern trend eucrites could be generated by relatively low degrees of partial melting, with both types of eucrites originating from the same source. This hypothesis was supported using trace element systematics by Warren and Jerde (1987). In contrast, Barrat et al. (2007) suggested that a magma ocean model can explain the Nuevo Laredo trend/main group, assuming an appropriate initial starting composition (high relative Mg content). However, this model becomes problematic when attempting to explain the Stannern trend. To explain the Stannern trend as a consequence of a magma ocean, a complex mixture of eucritic melts and highly residual and/or crustal partial melts are needed (Barrat et al., 2007; Warren and Kallemeyn, 2001).

1.3.2 Metamorphism in eucrites

Almost all eucrites have undergone thermal metamorphism/equilibration (Takeda and Graham, 1991; Yamaguchi et al., 1996). The majority of eucrites have been metamorphosed at

temperatures ranging from 700-1000 °C (Takeda and Graham, 1991), although some eucrites have been metamorphosed at temperatures close to, or exceeding their solidus (~1060 °C)(Yamaguchi et al., 2001). To classify the degree of this thermal metamorphism/ equilibration, Takeda and Graham (1991) and Yamaguchi et al. (1996) developed a scheme based on petrography and pyroxene compositions. The least metamorphosed type, Type 1 eucrites, (or eucritic clasts in howardites/polymict eucrites) have extensive pyroxene zoning fully preserved; these eucrites are extremely rare and often only occur as clasts in breccias (Takeda and Graham, 1991). Type 2-6 eucrites indicate increasing degree of metamorphism, with the least metamorphosed eucrites having glassy mesostasis and unclouded pyroxenes, and more strongly metamorphosed eucrites having relict recrystallized mesostasis and clouded pyroxenes. The most highly metamorphosed eucrites, Type 7 eucrites, often developed a granular texture that overprints and obscures original igneous textures. (Yamaguchi et al., 1996)

Metamorphism is thought to be caused by impacts, heating by lava flows, and intrusions (Yamaguchi et al., 1996). Warren and Kallemeyn (2001) found a weak correlation between trace element ratios and metamorphic grades in eucrites, which reflected the fact that most Stannern trend eucrites are weakly metamorphosed (Types 1-4) and most Nuevo Laredo Trend/Main Group eucrites are more strongly metamorphosed (Types 5-7) (Yamaguchi et al., 2009). Yamaguchi et al. (1996) inferred that the highly metamorphosed eucrites were buried deep in the crust and some underwent partial melting (e.g., EET 90020).

1.4 Summary of the study

In November 2011, thin sections were selected from the American Museum of Natural History. Selection was based on bulk rock Hf vs Sc, to ensure a wide range in bulk rock

chemistry. Later (March 2011), an additional suite of thin sections of Antarctic meteorites was selected for study after examination at the Lyndon B. Johnson Space Center in Houston, TX based on bulk rock Hf vs. Sc.

The composition of apatite in all thin sections was measured first by electron microprobe with an analytical routine specifically designed to accurately measure the halogens. Then, OH was calculated by difference. To ensure this OH by difference calculation was correct, secondary ionization mass spectroscopy (SIMS) was used at the Woods Hole Oceanographic Institute (WHOI) for selected samples. Because only a few labs have measured the halogens and OH by SIMS (Caltech and Carnage Institute at Washington), a test needed to be conducted with the Cameca 1280 ion probe at WHOI. Standards were gathered and characterized, and during the summer of 2011 in collaboration with Henry Dick, Nobumichi Shimizu, and Brian Montleone the ion probe at WHOI was tested to determine the feasibility of measuring volatiles in apatite. Tests went according to plan and I was able to determine halogen and OH content of apatite from seafloor gabbos (Sarafian et al., in prep) and apatite from one eucrite. In January of 2012, the SIMS at WHOI was used again to measure the halogen and OH content of apatite from three eucrites. These measurements were consistent with the OH calculated by difference from electron microprobe measurements. During the course of working on this thesis I have also measured volatiles in apatite from several abyssal gabbros (0.36-0.49 wt% OH, 0.73-2.28 wt% F, and 0.24-2.02 wt% Cl) measured trace elements and volatiles in apatite included in zircon from Queens Maud Land, Antarctica (0-0.77 wt% OH, 2.9-3.77 wt% F, and 0-0.48 wt% Cl), and classified one meteorite (NWA 5136, LL6).

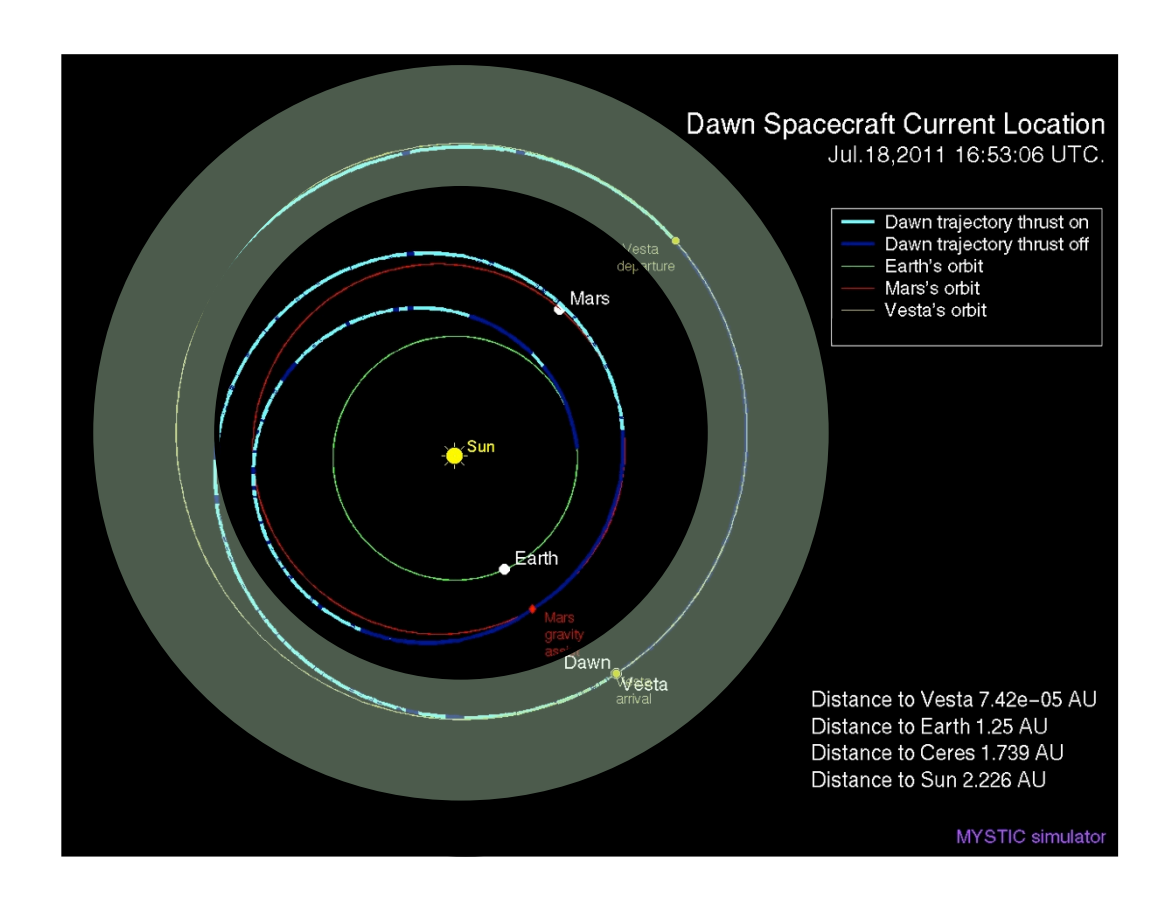


Figure 1.1 – Location of Vesta relative to the orbits of Mars (red circle) and Earth (green circle). Green shaded region is the asteroid belt. At the time this diagram was created the DAWN mission was orbiting Vesta. Blue and teal curve is the path DAWN took to reach Vesta. Figure modified from NASA DAWN website.

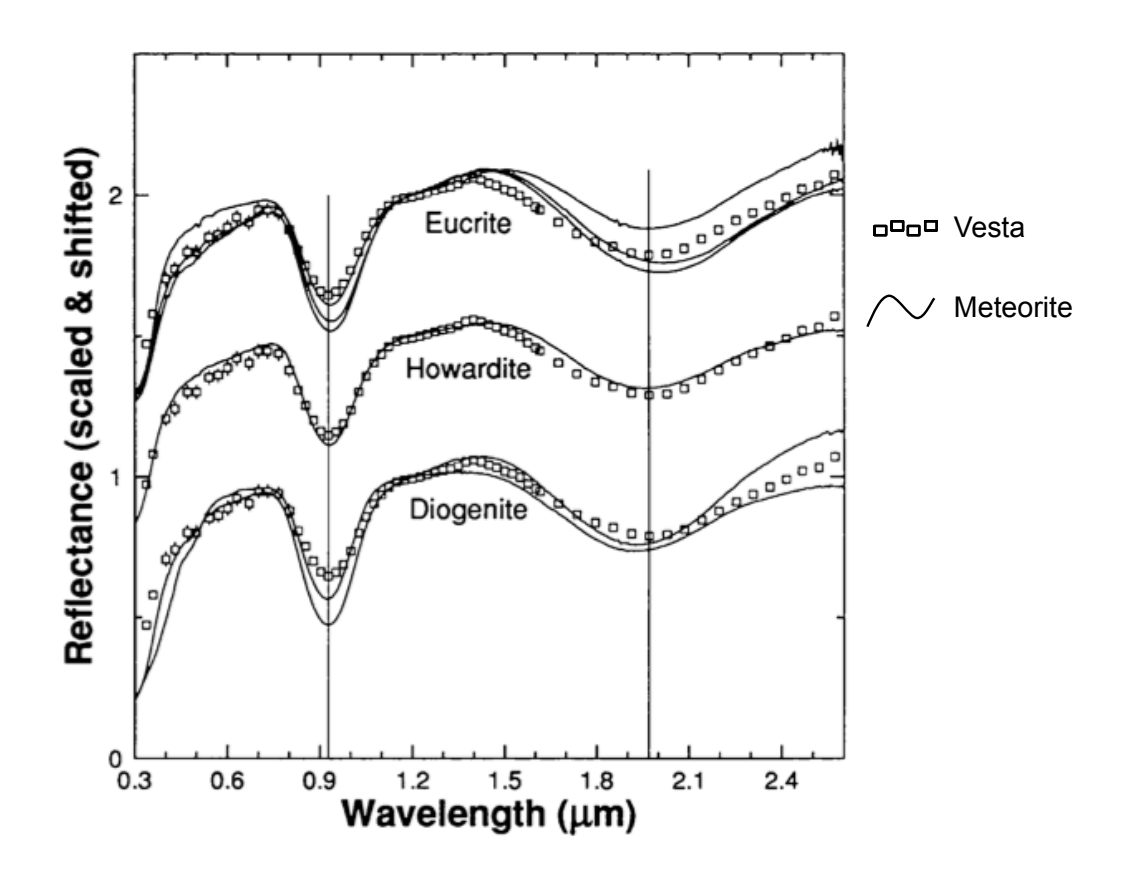


Figure 1.2 – Wavelength vs. Relative reflectance. Note the excellent fit between the spectra of the howardites and Vesta. The diogenite and eucrite also show reflectance spectra similar to that of Vesta. Figure modified from Hiroi et al. (1994)

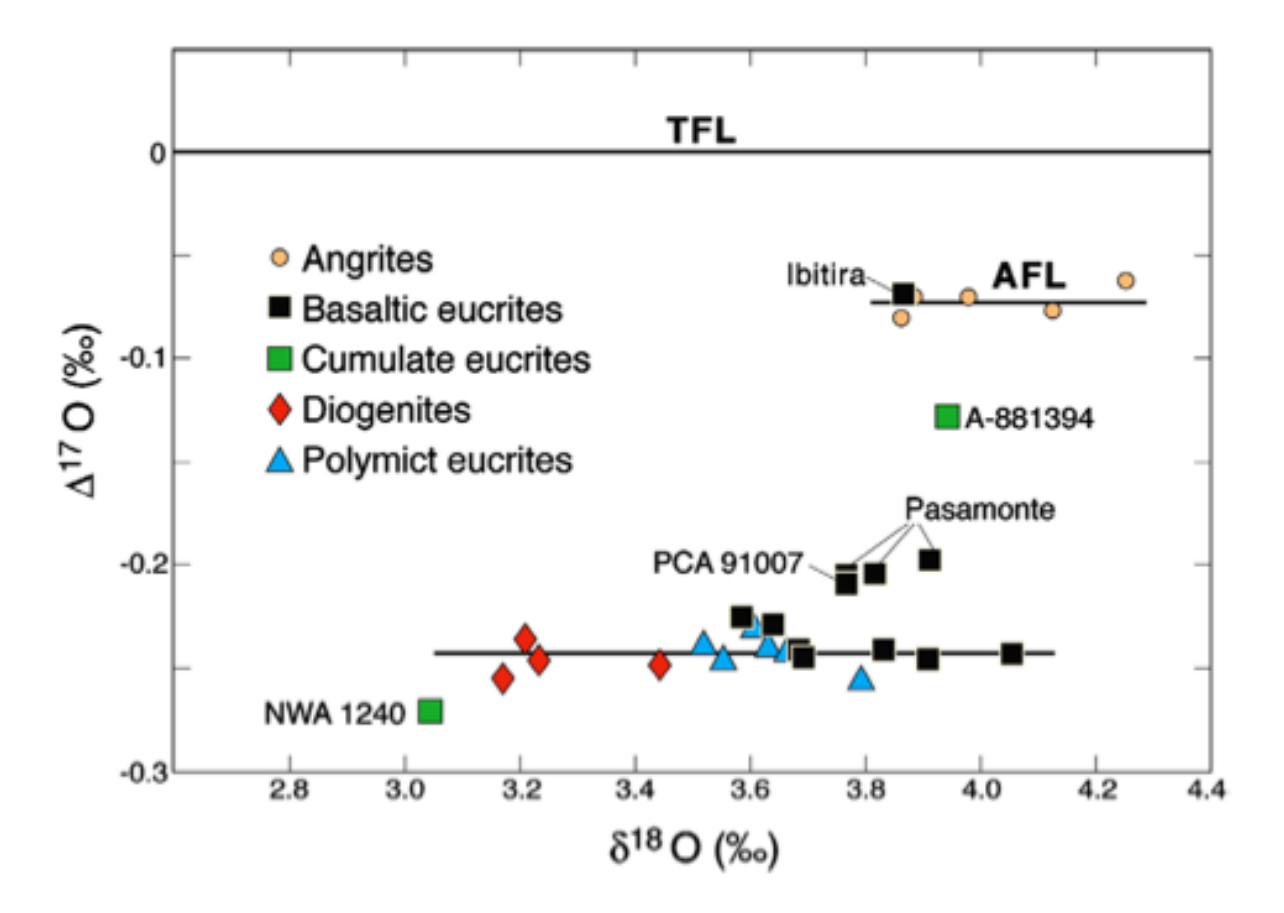


Figure $1.3 - \Delta^{17}O$ vs. $\delta^{18}O$. Most eucrites plot on a fractionation line below the terrestrial fractionation line (TFL). Note that Ibitira plots on the angrite fractionation line (AFL) and Pasamonte and cumulate eucrite A-881394 plot between AFL and the HED fractionation line. Figure from Scott et al. (2009)

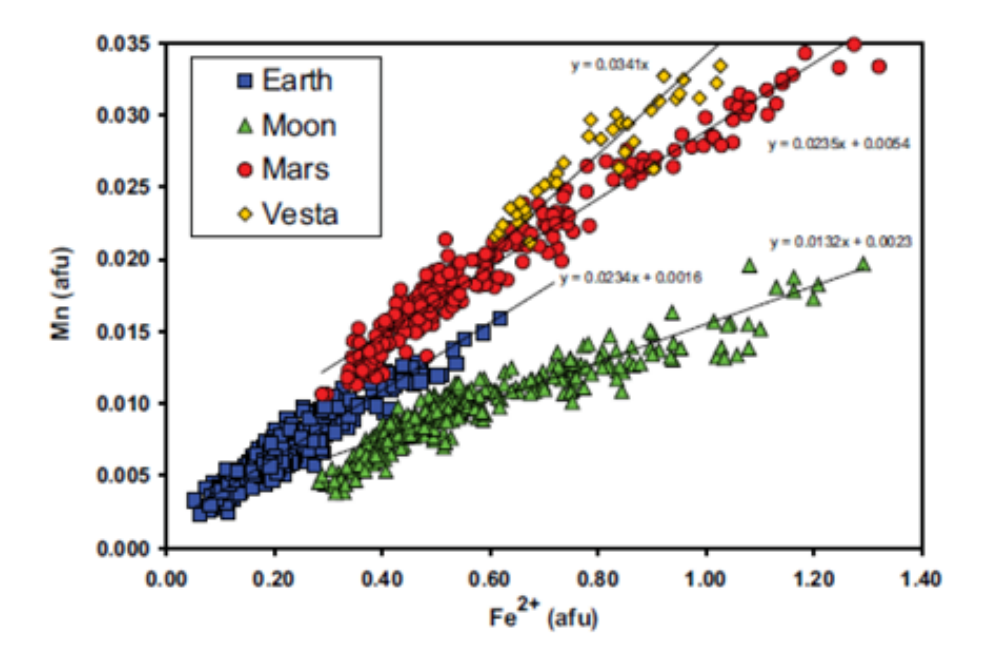


Figure 1.4 – Mn vs. Fe in pyroxene. Note that eucrite pyroxenes (Vesta) plot close to pyroxenes from Martian meteorites. Lunar pyroxenes are depleted in the relatively volatile element Mn compared to pyroxenes from Vesta, Mars and Earth. Figure from Karner et al. (2006)

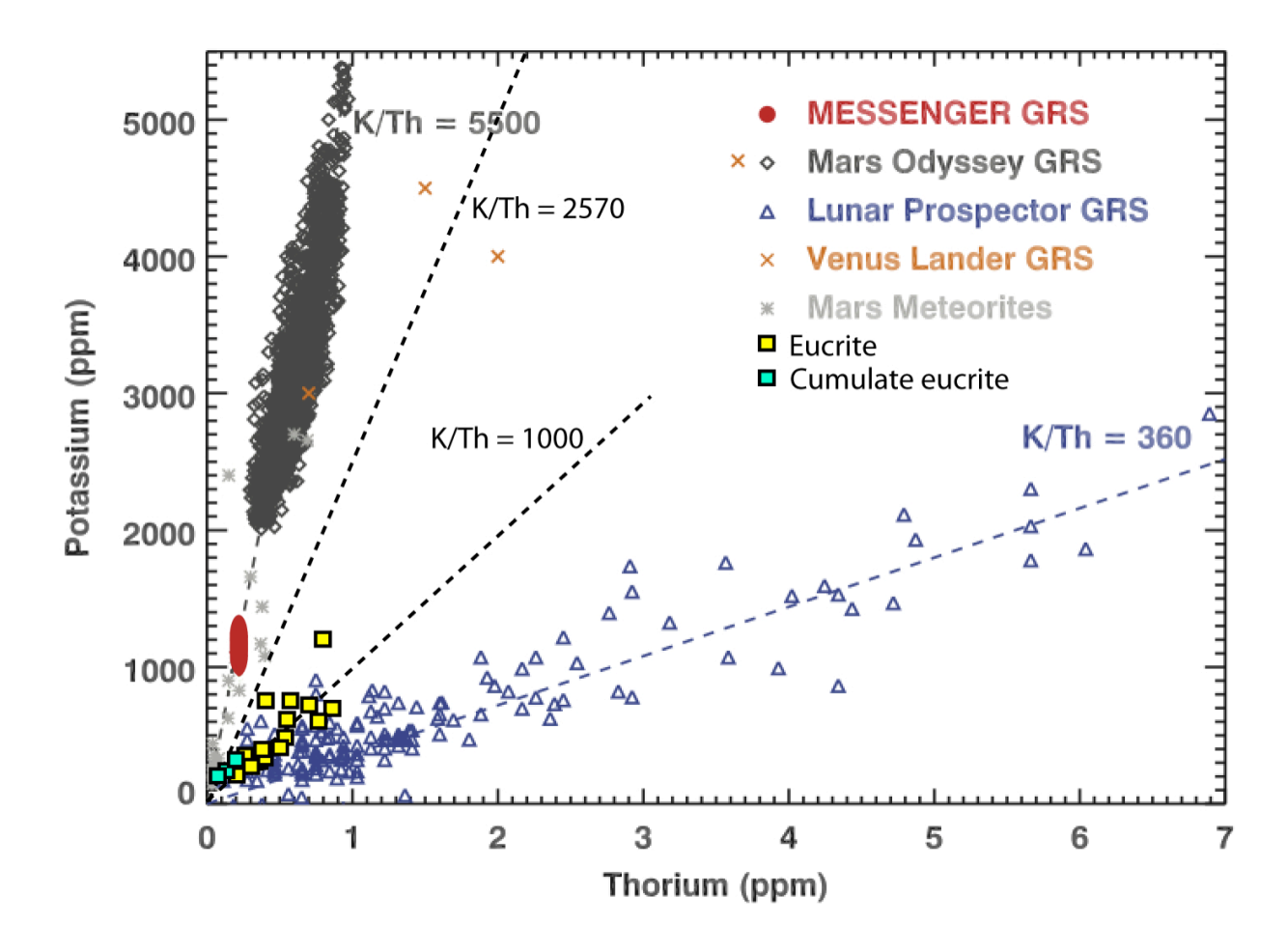


Figure 1.5 – Plot of bulk rock K vs. Th. Eucrites have low K/Th ratios compared to terrestrial bodies, but higher K/Th than lunar surface rocks. Modified from Peplowski et al. (2011), eucrite data (n=26) from Barrat et al. (2007) and Mittlefehldt (1979). The terrestrial bulk silicate earth K/Th is 2570 (Newsom, 1995; and refrences within).



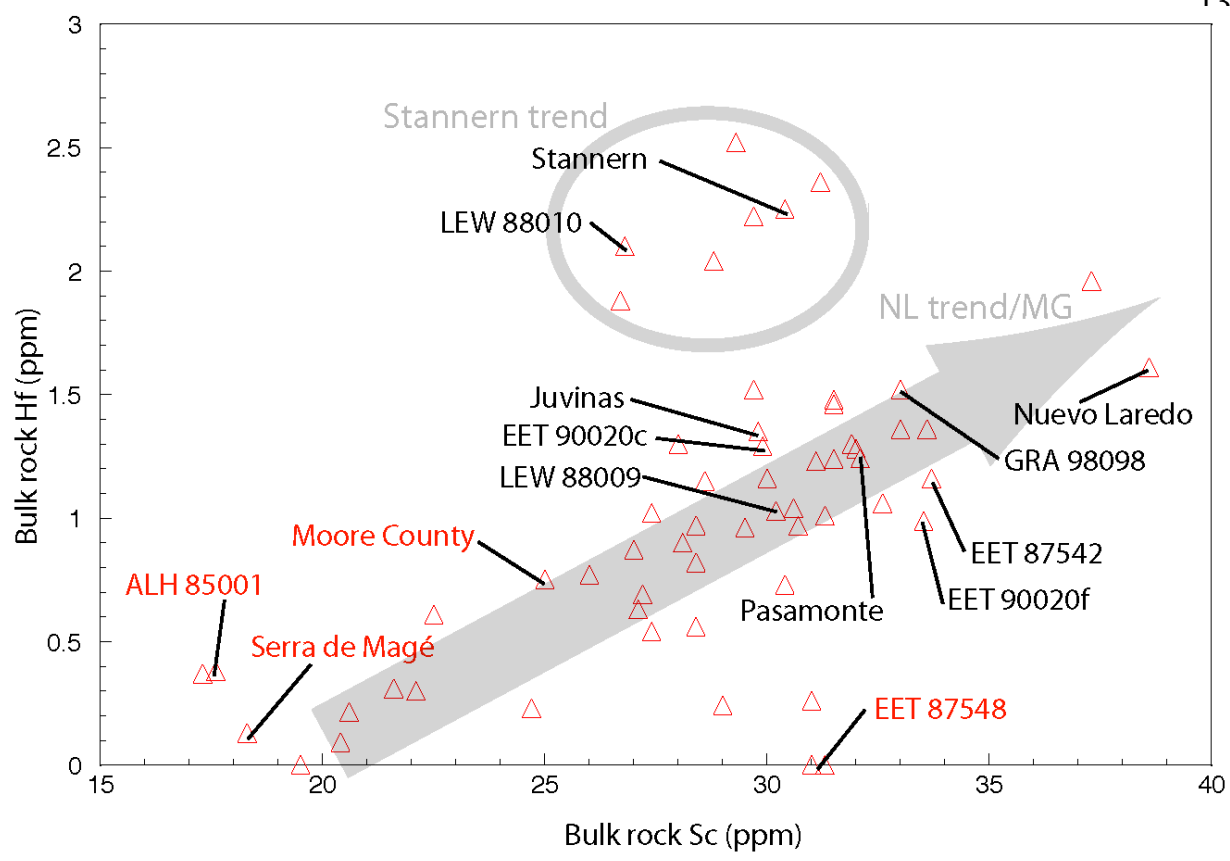


Figure 1.6: Bulk rock Hf vs. Sc for monomict and unbrecciated eucrites and Pasamonte (polymict eucrite). Labeled eucrites were selected for this study. Red labels (Moore County, Serra de Magé, ALH 85001, and EET 87548) are cumulate eucrites. Black labels are basaltic eucrites. EET 90020c is coarse-grained lithology and EET 90020f is fine-grained lithology from eucrite EET 90020. The Stannern trend is defined by enrichment in incompatible elements that causes an excursion from the linear trend of the Nuevo Laredo trend/main group (NL trend/MG). Data from Kitts and Lodders (1998), Warren et al. (2009), and Mittlefehldt and Lindstrom (2003).

Chapter 2:

THE NAURE OF VOLATILES ON 4-VESTA: CLUES FROM APATITE IN EUCRITES

2.1 Abstract

Apatite was analyzed by electron microprobe in 13 eucrites (3 cumulate and 10 basaltic). Most apatites were found in mesostasis, but in some eucrites, apatite is found as inclusions in pyroxene, as large euhedral crystals, and as veinlets. Eucritic apatite is fluorine-rich with minor chlorine and hydroxyl (calculated by difference). We confirmed the hydroxyl content by measuring hydroxyl directly in apatites from three representative eucrites (one cumulate and two basaltic eucrites), using secondary ionization mass spectroscopy. No correlation was found between volatile content of apatite and eucrite trend (i.e., Stannern trend vs. Nuevo Laredo trend/main group) or metamorphic grade of the meteorite. Partition coefficients were used to estimate the ratios of volatiles (hydroxyl vs. fluorine vs. chlorine) in coexisting melt and textures of apatite and mineral associations were used to determine the conditions of apatite crystallization. Late-stage apatite found in mesostasis has little hydroxyl or chlorine and is thought to have crystallized from a degassed magma. Several meteorites contain apatites with unusual habits and/or compositions. Euhedral early crystallizing apatites in Moore County occur as inclusions in pyroxene and are hydroxyl-rich (0.62 wt% OH), suggesting that water could have played an important role in the early crystallization of primitive eucrite magmas. Relativity large and abundant apatite in the residua eucrite EET 90020 are possibly part of a residual melt that mostly left EET 90020, confirming previous reports that eucrites probably do not sample all lithologies on Vesta. Relatively Cl-rich apatites occur in GRA 98098 (~1 wt% Cl), and these apatites as well as vein apatites in Juvinas may have crystallized from a high temperature

hydrothermal fluid. Overall, most eucritic apatites resemble fluorine-rich lunar mare apatites, but the relatively chlorine-rich apatite in GRA 98098 more closely matches the composition of apatite from lunar KREEP material, although apatite in GRA 98098 has more hydroxyl than apatite in KREEP.

2.2 Introduction

Eucrites are plagioclase pigeonite basaltic (non-cumulate) or gabbroic (cumulate) meteorites that sample one of the oldest planetary crusts, ~4.5 Ga (Misawa et al., 2005). While most eucrites are generally thought to be derived from the asteroid 4-Vesta (Clayton, 1993; Consolmango and Drake, 1977), some eucrites may be from different parent bodies (e.g., Pasamonte and Ibitira because of isotopic distinctions) (Greenwood et al., 2005; Mittlefehldt, 2005; Scott et al., 2009). Basaltic eucrites can be separated into two groups or trends based on bulk chemistry; Stannern trend eucrites are enriched in incompatible elements (e.g., Ti, Hf, Sc, etc.) compared to Nuevo Laredo trend/main group eucrites, which define a crystal fractionation trend (Figure 2.1) (BVSP, 1981). Much debate has circled around the petrologic conditions that created the two groups/trends. One model involves crystallization from a magma ocean on Vesta (e.g., Barrat et al., 2007; Righter and Drake, 1997; Takeda, 1997; Warren, 1997), with assimilation of crustal material to explain the Stannern trend; another model involves varying degrees of partial melting from a mantle source and crystal fractionation (e.g., Consolmango and Drake, 1977; Mittlefehldt, 1979; Mittlefehldt and Lindstrom, 2003; Stolper, 1977), with the Stannern trend eucrites forming by low degrees of partial melting (~5%). Eucrites have also been thermally metamorphosed to differing degrees and classified into seven different metamorphic grades/types based on pyroxene chemistry and petrography: eucrites with type 1 pyroxenes are

the least metamorphosed, and eucrites with type 7 pyroxenes are the most metamorphosed (Takeda and Graham, 1991; Yamaguchi et al., 1996). Cumulate eucrites generally have type 6 or 7 pyroxenes (Yamaguchi et al., 1996). This thermal metamorphism could have been caused by internal heat escaping by conduction through the crust, lava flows burying existing crust, and/or burial by ejecta blankets of impactors (e.g., Yamaguchi et al., 1996).

While eucrites are thought to be volatile-depleted (e.g., Papike, 1998), the cause of this depletion is poorly understood. The abundance and nature of volatiles are important bulk compositional characteristic of planetary bodies; moreover, magmatic volatiles (e.g., H₂O, F, and Cl) are important because they control phase stability, magmatic densities, and melting temperatures. F and Cl are moderately volatile elements that probably condensed as part of fluorapatite (~740K) and sodalite (~950K), respectively, from the solar nebula (Lodders, 2003). If this generalization is correct, then F is slightly more volatile than Cl. However it is important to note that in fluid-saturated magmatic systems Cl is concentrated in the fluid, whereas F is concentrated in the silica melt (Boudreau and McCallum, 1989; Brenan, 1993; Carroll and Webster, 1994). In this situation Cl is *more volatile* than F. Because eucrites are igneous rocks, and thus, crystallized from a melt, the latter behavior of the halogens may be more important than the former for this study.

Apatite $(M_{10}(ZO_4)_6(X)_2)$ where M = Ca, Na, Sr, Pb; Z = P, Si, As, V; and X = OH, F, Cl) is a volatile-bearing phase, and it is a ubiquitous, yet trace, mineral in terrestrial, lunar, and Martian igneous rocks (Patiño-Douce and Roden, 2006), chondrites (Jones et al., 2011), and eucrites (Delaney et al., 1984). While the halogens and H_2O do not partition equally into apatite, the composition of the X site of apatite is a function of the volatile composition of the coexisting melt (Boudreau and McCallum, 1989; O'Reilly and Griffin, 2000), however, quantitative

partition coefficients are limited for basaltic compositions (Mathez and Webster, 2005) and theoretical calculations suggest that the partitioning is complex (Patiño-Douce et al., 2011).

Nonetheless, McCubbin et al. (2011) recently used available partition coefficients between fluid-undersaturated melts and apatite to estimate volatile ratios in lunar magmas. Apatite textures can also give insight into magmatic conditions. Stubby (euhedral) apatite generally forms if a magma is fluid saturated, and acicular apatite generally forms when a melt is quenched (Wyllie et al., 1962). Euhedral apatite contained in early crystallizing phases crystallized relatively early, whereas apatite associated with sulfides, ilmenite, and other late-crystalizing phases in mesostasis crystallized relatively late. Thus, the texture and composition of apatite can be used as a tool to estimate the volatile composition of basaltic magmas.

As noted above, apatite composition has been used to infer volatile compositions of lunar basalts and the lunar interior (e.g, Boyce et al., 2010, McCubbin et al., 2010a, 2010b; 2011). Following this lead, we report apatite textures and compositions in eucrites with the aim of characterizing the volatile abundances in eucritic basalts and their parent asteroid, Vesta.

2.3 Sample selection

Basaltic and cumulate eucrites were selected based on 5 features.

(1) The selected eucrites showed significant variations in bulk rock Hf and Sc contents – these two elements have been used to illustrate bulk rock compositional variation in eucrites, and to delineate the Stannern trend and the Nuevo Laredo trend/main group eucrites (e.g., Mittlefehldt and Lindstrom, 2003) (Figure 2.1). Stannern and LEW 88010 were selected because they are representative of the Stannern trend. Main group-Nuevo Laredo trend eucrites (ALH 85001, Serra de Magé, Moore County, LEW 88009 Juvinas, Pasamonte, EET 87542, GRA

98098, and Nuevo Laredo) were selected to be representative of the range of Hf and Sc contents displayed by meteorites of this group. EET 87548 was selected because it has an unusually low Hf abundance (Figure 2.1).

- (2) All eucrites selected (except Pasamonte) are monomict breccias or unbrecciated to simplify interpretation of bulk rock and mineral compositions.
- (3) Some of the eucrites are intensively studied eucrites (e.g., Stannern, Nuevo Laredo, Pasamonte, Juvinas, Moore County, and Serra de Magé). These previous studies provide us with a variety of geochemical and petrological data, which help in the interpretation of our data.
- (4) Some eucrites are falls (e.g., Stannern, Nuevo Laredo, Pasamonte, Moore County, and Serra de Magé). Falls are ideal because they have minimal terrestrial weathering.
- (5) Eucrites with a variety of metamorphic grades were selected to examine if a relationship exists between metamorphic grade and volatile composition of apatite. Meteorites that are between 2.5 and 7 on the Takeda and Graham (1991) and Yamaguchi et al. (1996) thermal equilibrium scale were selected.

2.4 Analytical Methods

2.4.1 Electron Microprobe (EMP)

We followed the analytical methods of Patiño-Douce et al. (2011) for electron microprobe (EMP) analyses using a JEOL 8600 electron microprobe at the University of Georgia. Typical operating conditions were a 15kV accelerating voltage and a 5nA beam current. Grain size permitting, a 5μm defocused electron beam was used, but most apatites were too small for a defocused beam. Thus, either a focused electron beam (~1μm) or a beam raster (~1-3μm)

was used. Even with a focused or a beam raster, secondary Si and Fe fluorescence occurred during many analyses. Thirteen elements (P, Ca, Fe, Si, Na, Mg, S, As, Sr, Y, Ce, F, and Cl) were measured in apatite, as our intent was to fully characterize the apatites and to understand substitutions. After the 13-element routine was performed on all apatites, a shorter routine (consisting of P, Ca, Fe, Si, F, Cl; same count times as before) was used. This shorter analytical routine was used to limit electron beam time on the apatites (Stormer et al., 1993), to increase the number of analyses per day, and because Na, Mg, S, As, Sr, Y, and Ce were consistently below detection limits (Table 1).

Accurately analyzing apatite can be difficult due to halogen migration (Henderson, 2011; Stormer et al., 1993) and multiple substitutions for P (e.g., Si, C, S, As) and Ca (e.g., Fe, Y, REE, Mg, Sr, Na) (Pan and Fleet, 2002). To ensure accurate analyses we used the analytical routine of Patiño-Douce et al. (2011), which measures the halogens first to minimize halogen migration (Piccoli and Candela, 1994). An analytical screen described by Patiño-Douce et al. (2011) was used to reject EMP apatite analyses that are not stoichiometric. After using this screen, acceptable analyses when normalized to 25 oxygens (one formula unit), have between 9.7 and 10.1 cations in the Ca site (Ca, Y, Ce, Sr and Fe), between 5.8 and 6.1 cations in the P-site (P, Si, and As), less than 2.05 anions in the x-site and the analytical total is between 98.5 and 100.5 (see online supplement for all acceptable analyses).

In apatite, the X site is occupied by F and Cl, as well as OH, O, CO₃, and Br (Pan and Fleet, 2002). However the most common of these latter anions in terrestrial and lunar basalts is OH (Boyce et al., 2010; Greenwood et al., 2011; McCubbin et al., 2010a; Piccoli and Candela, 2002). Thus, in this paper, we assume the missing anion in the x-site is OH, and calculate the amount by difference from the sum of F + Cl.

Because this paper focuses on the volatiles, careful attention was given to analyzing F and Cl. Some writers have suggested that repeated exposure to an electron beam permanently affects fluorapatite composition (Henderson, 2011; Stormer et al., 1993) and McCubbin et al. (2011) described in detail an apparent time dependent increase in fluorine X-ray intensities during EMP analyses. These writers argued that F count rates increase during an analysis, and that count rates will stay elevated if the same spot is analyzed again. This suggests F might migrate up the crystal lattice towards the surface of the apatite crystal. Thus, using fluorapatite (i.e., Durango and Wilberforce) as a standard could be problematic. If standards are permanently damaged by exposure to the electron beam and as a result have an elevated F concentration at the surface of the crystal, one would underestimate the F content in an unknown. This underestimation of F content in an unknown would cause an overestimation of OH content due to the method of calculating OH by difference. To ensure our F analyses were accurate, a second Durango apatite grain was analyzed as an unknown during each analytical session. To address possible time dependent increase of F X-ray intensities, F was measured first with a relatively low beam current (5nA) for 10s (to minimize F migration) and an analytical screen was used to reject apatites with too much halogens (primarily F) in the X site. With these protocols in place, we tried to minimize the potential errors in F analysis of apatite unknowns. Nonetheless, given the issues with F analysis in apatite, secondary ionization mass spectroscopy (SIMS) was used as a final check to ensure accurate OH, F and Cl abundances.

2.4.1.1 Rare-earth elements (REEs) in apatite: Rare earth elements were measured with a 25nA focused beam (1μm). Only P, Ca, Ce and Y (as a proxy for the heavy REE) were measured because the goal was to determine if the REE were present in significant amounts in apatite from

eucrites. Count times for Ce and Y were increased to five minutes on the peak and background positions while keeping 10s count times for P and Ca. To assess quality of the data, P and Ca concentrations were compared to previous P and Ca measurements performed with the longer analytical routine described above.

2.4.1.2 Precision and Accuracy by electron microprobe (EMP): The apatite standards, Durango and Wilberforce, were analyzed as unknowns multiple times to examine reproducibility of the EMP data. For Durango apatite, measured F, Cl, P₂O₅, and CaO contents varied by 5.6%, 14%, 1.3%, and 1.0% (1σ). The analytical precision for OH was calculated using standard error propagation; hydroxyl varied by 15%. We assessed accuracy by comparing the compositions of Durango and Wilberforce apatite that we measured to the published values of Jarosewich et al. (1980) and the values established by the C.M. Taylor Company (Taylor standard block, information from Taylor multi element standard documentation, by C.M. Taylor, C.M. Taylor Company), respectively (Table 1). Our analyses closely match the published values.

2.4.2 Secondary Ionization Mass Spectrometry (SIMS)

To ensure our calculated OH values are accurate, SIMS was used to measure OH directly. We used the Cameca IMS 1280 ion probe at the Woods Hole Oceanographic Institution (WHOI) for SIMS analyses. Analytical methods were based on those of Hauri et al. (2002); deviations from this method will be discussed here. Before SIMS analyses began, the secondary beam was centered in the field aperture using the image plate. Then the signal for ³¹P was maximized with additional centering of the beam using the electron multiplier. Finally, masses 12 and 17 were checked on the electron multiplier for a homogenous signal, ensuring the beam was not on a

crack or contamination. A -10 kV sample voltage and a 190 pA primary current was used. Mass resolving power (M/ Δ M) was ~6800, enough to differentiate between ¹⁷O and ¹⁶O¹H. A Cs⁺ primary beam was rastered over a 30 μ m², 20 μ m², and 10 μ m² area and a field aperture was used to collect ions from the center of the secondary ion beam, ~15 μ m², ~10 μ m², and ~6 μ m², respectively, to minimize crater edge effects. Secondary negative ions ¹²C, ¹⁶O¹H, ¹⁸O ¹⁹F, ³¹P, ³²S, ³⁵Cl, ¹⁹F¹⁶O, and ³⁷Cl were collected for ten cycles; ¹⁸O and ³¹P were used as reference masses. Calibration curves were used to determine elemental concentrations and were calculated using the inversion method of Boyce et al. (in press).

2.4.2.1 Detection limit of hydroxyl in apatite by secondary ionization mass spectroscopy: To obtain a low detection limit of OH, samples must be free of any contamination containing H. All samples were repolished and ultrasonically cleaned in deionized water to remove any remnant carbon coat or polishing residua. Once the thin sections and the standard mount were cleaned and dried, they were put into an oven (70°) for 24 hours, then placed under vacuum (~5x10⁻⁷ torr) for ~3 days. Following gold coating, they were placed under high vacuum (~5x10⁻⁹ torr) for >8 hours. Because the calibration curve for OH does not intersect 0, a contaminant must be present. This non-zero intercept was also seen by Boyce et al. (2010) who attributed this observation to the presence of an unknown hydrocarbon contaminant. Plagioclase and pyroxene (assumed to be anhydrous) were used to determine instrumental "blank" values. The detection limit for OH is defined by the maximum apparent OH intensities for plagioclase and pyroxene (assumed to be anhydrous) adjacent to apatites. Hydroxyl concentrations in eucritic apatite were always above the instrumental "blank" values for plagioclase and pyroxene (Figure 2.2).

2.4.3 Scanning electron microscopy (SEM)

To help identify some phases, a Zeiss 1450EP variable pressure scanning electron microscope at the University of Georgia was used. Phase compositions were measured using an Oxford INCA energy dispersive detector and a 20 kV operating voltage.

2.5 Results

2.5.1 Textural analysis of apatite in eucrites

Apatite displays a wide range of crystal habits and sizes in the eucrites we studied.

Apatite ranges from euhedral to subhedral grains in Moore County to subhedral grains in most eucrites (ALH 85001, ALH 87548, Serra De Magé, BTN 00300, LEW 88009, EET 87542, LEW 88010, EET 90020, GRA 98098, Nuevo Laredo, Pasamonte, Stannern) to anhedral veinlets in Juvinas.

Cumulate Eucrites

Moore County: Moore County is an unbrecciated cumulate eucrite which contains granular to subophitic plagioclase (0.5-1.5 mm long; An₉₀-An₉₃), subhedral to euhedral orthopyroxene with augite exsolution lamellae (0.2-6 mm wide), and minor amounts of tridymite, ilmenite, chromite, troilite, Fe-Ni metal, and apatite (Hess and Henderson, 1949; Mayne et al., 2009). Apatite occurs as euhedral to subhedral grains (15 - 40 μm) included in pyroxene (Figure 2.3b) and as acicular grains (100 μm long) included in interstitial tridymite

grains (Hess and Henderson, 1949). Moore County has a crystallization age of 4.484 Ga (Tera et al., 1997).

ALH 85001: ALH 85001 is a monomict cumulate eucrite with angular lithic fragments up to 6mm across, composed of orthopyroxene with exsolved augite lamellae and plagioclase (An₉₂. 94), with grain sizes up to 3mm (Antarctic Meteorite Newsletter 9-3; Mittlefehldt and Lindstrom, 2003). Minor phases include troilite, ilmenite, and apatite. Apatite is rare and occurs as 1-5 μm crystals along grain boundaries of plagioclase and pyroxene (Figure 2.3a). Mittlefehldt and Lindstrom (2003) provided a bulk rock chemical analyses of ALH 85001.

EET 87548: EET 87548 is a monomict cumulate eucrite which has an ophitic texture; it has orthopyroxene with exsolved augite lamellae (up to 0.6 mm wide), plagioclase (0.7mm long; An₈₆₋₉₂), and minor phases including tridymite, troilite, ilmenite, and apatite (Antarctic Meteorite Newsletter 12-1; Mittlefehldt and Lindstrom, 2003). Apatite is anhedral (~5 μm) and associated with ilmenite and troilite as interstitial phases. We could not analyze apatite in EET 87548 because it was too small/not polished sufficiently. While the petrography of EET 87548 has not been extensively examined, Mittlefehldt and Lindstrom (2003) and Warren et al. (1996) reported on the bulk composition of this meteorite.

Serra de Magé: Serra de Magé is a 4.399 Ga unbrecciated cumulate eucrite with weakly orientated plagioclase grains (An₉₄₋₉₆), orthopyroxene with augite lamellae, pigeonite, and minor phases including chromite, silica, Fe-Ni metal, troilite, ilmenite, apatite and zircon. (Mayne et al., 2009; Prinz et al., 1977; Tera et al., 1997). Apatite occurs as anhedral grains (~30 μm long)

in mesostasis with silica, troilite, and pyroxene (Figures 2.3c & d). The mesostasis is irregularly shaped and \sim 10 µm-1 mm in maximum dimension. Serra de Magé was probably aqueously altered while on its parent body, which produced quartz veining (Treiman et al., 2004). A phase we interpret to be a Fe oxide/hydroxide with \sim 77 wt% Fe₂O₃ occurs in the mesostasis and as veinlets (Figures 2.3c & d). This phase may be a replacement product of troilite because troilite is often rimmed by the Fe oxide/hydroxide, veinlets of Fe oxide/hydroxide often terminate at troilite rimed by the Fe oxide/hydroxide, and material with a composition intermediate between troilite and the Fe oxide/hydroxide occurs with a similar shape as the troilite grains. This intermediate composition material has less S than troilite, and it has the same amount of Fe as the Fe hydroxide.

Basaltic eucrites

BTN 00300: BTN 00300 is an unbrecciated basaltic eucrite, which consists of granular plagioclase (An₈₉₋₉₀) and pyroxene with an average grain size of ~200μm (Antarctic Meteorite Newsletter 24-2; Mayne et al., 2009). Minor phases include chromite, ilmenite, silica, troilite, Fe-Ni metal, merrillite and apatite (Mayne et al., 2009). Apatite occurs as subhedral grains (~20 μm) associated with ilmenite, troilite, and silica in relict mesostasis (Figure 2.3e).

LEW 88009: LEW 88009 is an unbrecciated basaltic eucrite with an ophitic texture; it consists of plagioclase (An₈₁₋₉₄), pyroxene with an average grain size of 0.1mm, and minor phases including chromite, troilite, ilmenite, merrillite, and apatite (Antarctic Meteorite Newsletter 13-2; Mayne et al., 2009). Apatite occurs as interstitial subhedral grains (1-30 μm long) associated with troilite and ilmenite (Figure 2.3f).

EET 87542: EET 87542 is a monomict basaltic eucrite with a relativity coarse ophitic texture containing plagioclase (up to 0.7mm long; An₈₆₋₉₂), pyroxene (a continuous range from pigeonite to augite; up to 0.6mm wide) and minor phases, including Fe-Ni metal, troilite, merrillite, and apatite (Antarctic Meteorite Newsletter 13-1). Apatite occurs as interstitial anhedral grains (<1-20 μm), not visibly associated with merrillite. While the petrography of EET 87542 has not been extensively examined, Mittlefehldt and Lindstrom (2003) examined the bulk composition of EET 87542.

LEW 88010: LEW 88010 is an unbrecciated eucrite with plagioclase (An₇₅₋₈₆) and pyroxene which is 0.6-1.2mm, minor phases include ilmenite, troilite, chromite, merrillite, and apatite (Antarctic Meteorite Newsletter 13-2; Mayne et al., 2009). Apatite is an anhedral interstitial phase ($\sim 10 \ \mu m$) associated with ilmenite, troilite, and merrillite.

EET 90020: EET 90020 is an unbrecciated basaltic eucrite which contains two different lithologies, a coarse-grained lithology and a fine-grained lithology and at the hand sample scale EET 90020 has vugs. These vugs are narrow voids that occur throughout the meteorite and they coated in fusion crust. The vugs which are concentrated in the fine-grained lithology, but they also occur in the coarse grained lithology (Bogard and Garrison, 1997; Yamaguchi et al., 2001). The vugs also provide evidence that EET 90020 was a breccia prior to a metamorphic annealing event (Yamaguchi et al., 2001). The fine-grained lithology has a subophitic texture with plagioclase (250-800 μm long; An₈₈₋₉₂) and anhedral pigeonite (type 5) with augite exsolution lamellae (400-700 μm wide) (Yamaguchi et al., 2001). The coarse-grained lithology has a

granular texture with laths of plagioclase (150-400 µm long; An₈₉₋₉₁) and anhedral to granular pigeonite with augite exsolution lamellae (600-900 µm wide). An area of the coarse grained lithology, about 2 x 1 mm, consists of granular to stubby plagioclase, anhedral pyroxene, interstitial tridymite, and abundant apatite (30 µm-1mm long; Figure 2.4a). The minor phases are similar in the two lithologies, and include ilmenite, spinel, and laths of tridymite associated with each other, troilite, Fe-Ni metal, Fe-rich olivine (sometimes associated with oxides), and Caphosphates (apatite and merrillite) (Yamaguchi et al., 2001). Similar to Yamaguchi et al. (2001), we found only merrillite in the fine-grained lithology and *only apatite* in the coarse-grained lithology, where it is associated with fine-grained stubby plagioclase. A crystallization age of EET 90020 could not be determined due to a strong reheating event it experienced at 4.49 Ga (Yamaguchi et al., 2001).

GRA 98098: GRA 98098 is an unbrecciated basaltic eucrite, which consists of mm sized plagioclase (An₈₃₋₉₃) and orthopyroxene with 1-5 micron thick lamellae of augite; it has distinct white veins that are composed of a sub-equal mixture of euhedral plagioclase (100-500 μm long) and granoblastic silica (~50 μm) with minor pyroxene (Figure 2.4e)(Antarctic Meteorite Newsletter 22-2; Mayne et al., 2009). Minor phases include chromite, ilmenite, troilite, apatite, Fe-rich olivine, and merrillite (Antarctic Meteorite Newsletter 22-2; Mittlefehldt and Lee, 2001). Apatite occurs as subhedral to euhedral interstitial grains (20-300 μm long), and is not associated with merrillite (Figure 2.4c & d). Mittlefehldt and Lee (2001) found phosphates in the silica/plagioclase veins, but they did not specify if the phosphate was apatite or merrillite; we found apatite adjacent to, but not within the silica-rich veins.

Nuevo Laredo: Nuevo Laredo is a monomict basaltic eucrite with lithic clasts (~3mm) in a fine-grained matrix. The lithic clasts have an ophitic texture with laths of plagioclase (100-800 μm; An₈₅), anhedral type 5 pyroxene (50-600 μm), and minor phases including tridymite, cristobalite, Fe-metal, troilite, ilmenite, merrillite, and apatite (Duke and Silver, 1967; Takeda and Graham, 1991). Apatite is subhedral to anhedral (<1-60 μm) and associated with other minor phases in relict mesostasis, which generally occurs between large plagioclase laths. Nuevo Laredo has a crystallization age of 4.555 Ga. (Tatsumoto et al., 1973).

Stannern: Stannern is a monomict basaltic eucrite with lithic fragments (~ 5mm) set in a fine-grained recrystallized matrix of variable size (Duke and Silver, 1967). The lithic fragments consist of euhedral plagioclase (0.2-3 mm long; An₈₀) surrounded by type 5 pigeonite (0.1-2mm wide) with minor silica (Duke and Silver, 1967; Takeda and Graham, 1991). Relict mesostasis occurs at junctions of pyroxene and plagioclase grains, and consists of ilmenite, chromite, troilite, silica, augite, merrillite, and apatite (Takeda et al., 1983). Apatite is 5-50 μm long and occurs as subhedral/euhedral grains associated with other relict mesostasis phases, including merrillite. Stannern has a crystallization age of 4.564 Ga. (Kleine et al., 2005).

Pasamonte: Pasamonte is a polymict basaltic eucrite with fine- to medium-grained lithic fragments set in a granulated eucritic matrix. The lithic fragments consist of type 5 pigeonite (0.1-0.5mm wide), plagioclase (0.1-1mm long; An₈₀₋₉₅), and mesostasis (BVSP, 1981; Takeda and Graham, 1991). Mesostasis consists of tridymite, ilmenite, Fe-Ni metal, troilite, merrillite, apatite, zircon, olivine, baddeleyite, Ca-rich pyroxene, and plagioclase (Miyamoto et al., 1985). Apatite occurs as 1-30 μm subhedral to anhedral grains in the mesostasis. Apatite and merrillite

were not found associated with one another. Pasamonte has a crystallization age of 4.565 Ga (Trinquier et al., 2008), and Scott et al. (2009) argued that Pasamonte was from a different parent body because it has an anomalous Δ^{17} O value for a eucrite. Because Pasamonte may be from a different parent body than the other eucrites studied here, we examined Pasamonte in less detail.

Juvinas: Juvinas is a monomict basaltic eucrite with lithic clasts composed of granular plagioclase (An₉₂), type 5 pigeonite (200 μm-2 mm) with augite lamellae and minor phases including silica, ilmenite, chromite, merrillite, and apatite (Harlow and Klimentidis, 1980; Kitts and Lodders, 1998; Takeda and Graham, 1991). Plagioclase has angular fractures, which often contains minor phases, including apatite. Apatite occurs as anhedral crystals filling the fractures in plagioclase, as veins along grain boundaries and cross cutting plagioclase and pyroxene (Figure 2.4b). Juvinas has a crystallization age of 4.539 Ga. (Manhes et al., 1984).

2.5.2 Apatite composition

Representative apatite analyses are presented in Table 1, and atomic proportions of F-Cl-OH are plotted in Figure 2.5. Most of the tabulated data represent a single analysis of an apatite grain, although some apatites (e.g., apatites in GRA 98098, EET 90020 and cumulate eucrites) were large enough to perform multiple analyses on them. No correlation was seen between apatite composition and whether the eucrite belonged to the Stannern trend or Nuevo Laredo trend/main group; there was also no correlation between apatite composition and metamorphic grade.

Apatites from all eucrites exhibit a range of OH and F, while Cl remains nearly constant within each meteorite. For the EMP data, considerable analytical uncertainty exists in the

calculation of OH by difference, and much of the spread in F/OH is probably due to analytical uncertainty in the F analyses (see Figure 2.5). Apatites from cumulate eucrites generally plot on or near the F-OH join and are essentially Cl-free although apatite from ALH 85001, has up to 0.2 wt% Cl. These apatites range from pure fluorapatite (with minimal Fe and Si) to 80% fluorapatite – 20% hydroxyapatite components (~0.3 wt% calculated OH). Apatites in basaltic eucrites are also F-rich and typically Cl-poor, and thus similar to the apatites from the cumulate eucrites as evidenced by a similar range in composition from pure fluorapatite to 80% fluorapatite-20% hydroxyapatite components. Apatites from Juvinas, Pasamonte, and Moore County are richest in hydroxyapatite component. Apatite from GRA 98098 has a remarkable composition with up to 1.0 wt % Cl and 15% chlorapatite component. Except for apatite from GRA 98098, all apatites analyzed from basaltic eucrites, have 0.33 wt% Cl or less.

SIMS data generally confirm EMP data (Figure 2.5, Table 2.1, Table 2.2). For example, apatite in Moore County has an 82% fluorapatite component measured by EMP and an 18% hydroxyapatite component calculated by difference compared to 81.7% fluorapatite component and 18.1 % hydroxyapatite component measured by SIMS. Apatite in GRA 98098 has an 11% chlorapatite component measured by EMP and an 11% hydroxyapatite component calculated by difference compared to an 11.5% chlorapatite component and a 12.6 % hydroxyapatite component measured by SIMS.

Substitutions in apatite are common and many of them are coupled and/or can involve vacancies (Pan and Fleet, 2002). For example, divalent anions (e.g., O²⁻, CO₃²⁻, or S²⁻) can substitute in the X site coupled with REE³⁺ in the M site (Pan and Fleet, 2002). However, elements which are common in terrestrial apatite (e.g., Na, Mg, S, As, Sr, Y, and Ce) (Pan and Fleet, 2002), were consistently below or near the detection limit in the eucrite apatites. Apatites

from eucrites that are representative of the range of volatile composition we observed (Figure 2.5): GRA 98098 (high Cl content), Juvinas (high OH content), and EET 90020 (low OH, Cl contents), were chosen for an extended analytical routine designed to detect Ce and Y (as a proxy for HREE). Apatites from all three eucrites have similar and low Ce and Y concentrations (Table 2.1). Ce is below detection limit (\sim 0.1 wt%) and Y is \sim 0.1 wt%. The low REE abundance in our apatites is consistent with relatively low REEs in apatite from eucritic clasts in howardites (Barrat et al., submitted). However, measurable Fe (0-3.26 wt%, mean – 0.65 wt%) and Si (0-2.34 wt%, mean – 0.26 wt%) occur in most apatite. Most of the silica, and the high amounts of Fe measured are probably secondary fluorescence of Si and Fe from neighboring silicates, but low amounts of Fe (\sim <1 wt%) probably substitutes, as Fe⁺², for Ca²⁺ (Pan and Fleet, 2002).

2.6 Discussion:

If Vesta accreted with chondritic abundances of volatiles, that signature is not present in eucrites (McSween et al., 2010). The volatiles could have been lost during an asteroid-wide magma ocean (e.g., Righter and Drake, 1997), or the eucrite parent body could have accreted volatile-depleted. Either situation would result in the volatile depletion seen in eucrites. The unique volatile-rich nature of apatite gives us an opportunity to at least infer the volatile content and composition of the eucrite parent magmas, and perhaps infer the volatile content and composition of the asteroid.

Most eucritic apatites have igneous textures, and probably crystallized at high (magmatic) temperatures (Patiño-Douce et al., 2011) similar to terrestrial apatites in basalt (Piccoli and Candela, 2002), but to determine the volatile composition of a melt in equilibrium with apatite, extensive partitioning constraints are needed. Comprehensive data does not exist on

apatite-merrillite-melt assemblages, at the appropriate $f_{\rm O2}$ (one log unit below the iron-wüstite oxygen buffer; Wadhwa, 2008), and bulk compositions, thus calculating an accurate volatile composition of the parent eucrite melt is not simple. Following others (Boyce et al., 2010; McCubbin et al., 2011; McCubbin et al., 2010a; McCubbin et al., 2010b), we used the fluid undersaturated partition coefficient for F ($D_F^{apatite/melt} = 3.4$) and Cl ($D_{Cl}^{apatite/melt} = 1$) of Mathez and Webster (2005) and a calculated partition coefficient for OH ($D_{OH}^{apatite/melt} = 0.2$) after McCubbin et al. (2010a, 2011). Significant uncertainties exist in the use of these partition coefficients (Brenan, 1993; Mathez and Webster, 2005). Therefore, we only report qualitative ratios of the volatiles.

Ratios of volatiles in a melt will allow us to determine the nature of the fluid(s) on/in the eucrite parent body. If the OH:F:Cl ratio does not change considerably during crystallization, then the OH:F:Cl of the late stage melt (when most the apatite crystallized) should be similar to the OH:F:Cl ratio in the initial melt. This assumption is valid assuming OH, F, and Cl have similar compatibilities in a silicate melt and if the magma did not become saturated with a fluid. Hydroxyl, F, and Cl are all incompatible in a basaltic melt, (Workman et al. 2006) thus, the OH:F:Cl ratio should not change considerably during crystallization, unless a degassing event occurs. However, because basaltic eucrites were either flows on the surface or emplaced as shallow sills, most eucrites (Nuevo Laredo, Stannern, LEW 88009, EET 87542, BTN 00300, LEW 88010) probably degassed, and because of the low overburden pressure on Vesta, even magmas that crystallized more slowly probably degassed as well (e.g., Serra de Magé and ALH 85001).

2.6.1 ALH 85001, Serra De Magé, BTN 00300, LEW 88009, EET 87542, LEW 88010, EET 90020, Nuevo Laredo, and Stannern

Apatites in ALH 85001, Serra De Magé, BTN 00300, LEW 88009, EET 87542, LEW 88010, EET 90020, Nuevo Laredo, and Stannern generally occur as small (>1-40 μm) subhedral to euhedral interstitial grains or in mesostasis. These apatites have magmatic textures, are associated with late crystallizing phases, and they are F-rich. This suggests these apatites are primary magmatic phases and crystallized from a melt that degassed, or the melt was intrinsically depleted in Cl and H-species. If the apatites crystallized from a degassed melt, then these apatites can tell us little about the volatile reservoir(s) on Vesta.

2.6.2 Moore County

Moore County contains euhedral apatite included in pyroxene, suggesting that this apatite crystallized early. The apatite is relatively OH-rich and could have sampled the most primitive (least degassed) magma of the eucrites studied here (Sarafian et al., 2012). Figure 2.6 shows the average OH, F, and Cl composition (atomic proportions) of apatite from Moore County by SIMS and EMP, with the inferred ratios of H₂O, F and Cl in a fluid undersaturated melt in equilibrium with the apatite overlain. The melt in equilibrium with apatite in Moore County had more H₂O than F and more F than Cl, suggesting that the source region of the eucrite magmas had significant H₂O. One can estimate a melt H₂O content using a conservative partition coefficient for OH, 0.4 (Boyce et al., 2010); the fluid-undersaturated melt in equilibrium with apatite had 1.52 wt% H₂O. Because apatite in Moore County occurs as inclusions in pyroxene, which suggests the apatite crystallized early, we calculate the original melt H₂O content using two

endmember situations, apatite crystallized after 50% fractional crystallization, and apatite crystalized after 85% fractional crystallization, assuming H₂O behaves as a perfectly incompatible element. With these endmember estimations, the primary melt had 2,200-7,500 ppm H₂O. Assuming the partial melting model of Stolper (1977), using a 15% partial melt to produce Moore County, the vestian mantle would have 330-1130 ppm H₂O. Using the same assumptions as above, the vestian mantle would have 190-650 ppm F and 30-90 ppm Cl. Our estimates of H₂O in the vestian mantle is on the high end of the depleted upper mantle, 58-350 ppm H₂O for the terrestrial depleted mantle, but the vestian mantle had slightly more than one order of magnitude more F, 11 ppm F for the terrestrial depleted mantle, and two orders of magnitude more Cl, 0.51 ppm Cl for the terrestrial depleted mantle (Saal et al., 2002; Salters and Stracke, 2004). The Moore County source region also has more H₂O than the source region for the lunar mare basalt, up to ~130 ppm H₂O (Greenwood et al., 2011; McCubbin et al., 2012; McCubbin et al., 2010a; Saal et al., 2008). Our calculations show with respect to H₂O, Cl, and F, Vesta is *enriched* in volatiles compared to the terrestrial and lunar interiors. These calculated volatile abundances of the Moore County source region are uncertain because the partition coefficients are poorly constrained and the amount of crystallization and partial melting used in the calculations is uncertain. Regardless, these calculations show that vestian basalts could have had significant volatiles prior to degassing, thus D/H and δ^{37} Cl could provide insight into degassing processes on Vesta.

EET 90020 was described as an unbrecciated Nuevo Laredo trend/main group eucrite (Mittlefehldt and Lindstrom, 2003; Scott et al., 2009; Yamaguchi et al., 2001), but EET 90020 is probably a "residual eucrite" (Yamaguchi et al., 2009). Because EET 90020 is highly depleted in LREEs and other incompatible trace elements, Yamaguchi et al. (2009) suggest this eucrite is a residua of a partial melt that has migrated away from EET 90020 on Vesta. EET 90020 has two lithologies, a fine-grained lithology, and a coarse-grained lithology (Yamaguchi et al., 2001). If the apatite-bearing coarse-grained lithology was intrinsically more volatile rich than the merrillite-bearing fine-grained lithology, then the volatiles could explain the presence of apatite instead of merrillite (e.g., Patiño-Douce et al., 2011) and have contributed to the development of coarser grain size in the coarse-grained lithology (Giordano et al., 2004; Hirose and Kawamoto, 1995). During a metamorphic event, which reached temperatures above the solidus of eucrites, >5% of the EET 90020 melted, mostly mesostasis, and left the system through fractures in the rock (Yamaguchi et al. 2001 & 2009). An apatite-rich region of the coarse-grain lithology provides evidence of this partial melting event.

While Yamaguchi et al. (2001) reports modal abundance of apatite in the coarse-grained lithology to be 0.1 (vol. %), the apatite is clearly heterogeneously distributed and located close to fusion crust, which is probably a vug (Figure 2.4a). The apatite-rich region in the coarse-grained lithology has fine-grained stubby plagioclase with interstitial pyroxene (Figure 2.4a). This apatite-rich region is a thin zone, as if melt followed a crack, then broadens to about 2 mm wide. This apatite-rich finer-grained region in the coarse-grained lithology could be a remnant of the partial melt that mostly left EET 90020. One way to test this hypothesis, is to determine the REE pattern of the proposed remnant to determine if the proposed remnant melt compliments the bulk rock REE pattern of EET 90020 (Yamaguchi et al., 2009).

Figure 2.6 shows the average OH, F, and Cl composition (atomic proportions) of apatite from EET 90020 analyzed by SIMS and EMP compared to calculated ratios between H₂O, F and Cl of a fluid-undersaturated equilibrium melt. The estimated melt had sub-equal amounts of H₂O and F, and was depleted in Cl. Because this melt is probably derived by melting of basalt, not the interior of Vesta, it can tell us little about the interior of Vesta. The residua and extracted melt in EET 90020 suggests that complex igneous processes (melting and remelting) occurred on Vesta (Yamaguchi et al., 2009). Thus, the current population of eucrites probably does not sample every lithology of the vestian igneous suit. This contention is consistent with the observations of K-rich eucritic clasts found in howardites (Barrat et al., submitted).

2.6.4 GRA 98098

GRA 98098 is a metamorphosed eucrite with silica and euhedral plagioclase veins (Mittlefehldt and Lee, 2001; Scott et al., 2009). It is slightly more sodic and Cr-rich than most eucrites, and contains ~3-5 times more REEs than a typical eucrite (Mittlefehldt and Lee, 2001). The veins in GRA 98098 have been described as an infiltrating (late stage?) melt, but contrary to expectations, the veins have low REE abundances (Mittlefehldt and Galindo Jr, 2002). Apatite in GRA 98098 is the most Cl-rich, and relatively large compared to most apatites in the eucrites we studied. Two possible scenarios can explain the relatively Cl-rich nature of the apatites in GRA 98098.

One possible scenario to explain the relatively Cl-rich signature in apatite is that the parent magma of GRA 98098 was metasomatized by a relatively Cl-rich fluid, similar to oreforming fluids on Earth (Boudreau and McCallum, 1989; Patiño-Douce et al., 2011; Piccoli and Candela, 2002). This relatively Cl-rich fluid could have exsolved from a melt lower in the crust

on Vesta, rose, and metasomatized a higher area of the magma chamber (Boudreau and McCallum, 1989). This metasomatized rock could be the parent rock of GRA 98098. The fluid could have contributed to the elevated bulk rock Na and REE contents, as Na is soluble in fluids (e.g., Armellini and Tester, 1993) and REEs are slightly soluble in Cl-rich fluids (Boudreau and McCallum, 1989; Flynn and Wayne Burnham, 1978). The veins could be a late stage melt that infiltrated the parent lithology to GRA 98098 on Vesta (Mittlefehldt and Galindo Jr, 2002). If the late-stage melt was saturated with merrillite prior to its infiltration to GRA 98098, this saturation could account for the low abundance of REEs in the vein material (Mittlefehldt and Galindo Jr, 2002), merrillite concentrates the REE and can account for ~90% of the REEs in eucrites (Hsu and Crozaz, 1996).

Another possible scenario to explain the relatively Cl-rich apatites and silica-rich-veins is that GRA 98098 was infiltrated by a volatile-rich fluid post-crystallization, similar to the fluid suggested by Treiman et al. (2004) that crystallized quartz and sealed cracks in Serra de Magé. The crack-seal veins in Serra de Magé are thinner and less pervasive than most veins in GRA 98098, but one vein in GRA 980978 is a similar thickness as the veins in Serra de Magé. If the fluid infiltration in GRA 98098 was more pervasive than the fluid that crystallized veins in Serra de Magé, then more extensive and thicker veins would be expected. Because no hydrous low temperature stable phases (e.g. phyllosilicates) were found in GRA 98098, the fluid that crystallized the SiO₂-rich veins was probably at a higher temperature than the stability field of hydrous minerals, yielding a vein composed of anhydrous minerals (Barrat et al., 2011; McCollom and Shock, 1998; Python et al., 2007).

Both models involve a mobile fluid in the crust of Vesta, although the timing and composition of this fluid is uncertain. Figure 2.6 shows the average OH, F, and Cl composition

of apatite from GRA 98098 by SIMS and EMP compared to ratios between H₂O, F, and Cl for an equilibrium, fluid-undersaturated melt. A fluid-undersaturated melt in equilibrium with the apatites in GRA 98098 would have sub-equal amounts of F, H₂O, and Cl (Figure 2.6). The Clrich nature of the apatites in GRA 98098 suggests that a relatively Cl-rich fluid was present on Vesta. Detailed examination of abundant fluid inclusions in the GRA 98098 veins and the fluid inclusions in the vein found in Serra de Magé could provide key evidence regarding the nature of the hypothesized fluid.

2.6.5 *Juvinas*

Apatite in Juvinas occurs as anhedral grains associated with pyroxene and troilite, and occurs in a remarkable texture coating angular cracks in plagioclase, and pyroxene – we have seen a similar apatite texture in mantle xenoliths from Nunivak Island, AK (Figure 2.4c). While uncommon, veins of phosphates ± Fe-bearing phases occur in terrestrial samples (Broman and Martinsson, 2000; Groat et al., 1990). Broman and Martinsson (2000) found small F-rich apatite/magnetite veins in northern Sweden that crystallized from a high temperature fluid. At Durango, Mexico, F-rich apatite (Durango apatite) occurs in large angular cracks with pyroxene, calcite, and Fe-oxides, in an Fe-ore body that occurs in rhyolitic volcanics (Lyons, 1988). In this case, the apatite, pyroxene, calcite, and Fe-oxides are thought to have formed from a high temperature fluid rich in H₂O, halogens, and CO₂ that infiltrated the surrounding rock and crystallized the vein minerals (Lyons, 1988). While this fluid was H₂O- and Cl-rich, the apatites are F-rich because of the high temperature of the fluid (Patiño-Douce et al., 2011). Similarly, Juvinas has F-rich apatites associated with pyroxene and troilite. Because fluids are probably not stable on Vesta, a high temperature fluid could have formed the thin veined apatite, accessory

pyroxene, and troilite in Juvinas over a short period of time (Barrat et al., 2011). If the fluid was at a temperature higher than the stability field of other hydrous phases (but not F-rich apatite), then a hydrous fluid can form nominally anhydrous veins (Barrat et al., 2011; McCollom and Shock, 1998; Python et al., 2007).

The main differences between Durango apatite and apatite in Juvinas are (1) crystal size/habit, (2) trace element composition, and (3) associated minerals. (1) Durango apatite is generally euhedral and mm-cm sized, and apatite in Juvinas is anhedral and ranges from < 1 to ~100 µm microns in the long direction. Barrat et al. (2011) suggested degassing events were probably short lived on Vesta, whereas degassing in a terrestrial silica-rich magmatic system (i.e., Durango, Mexico) can occur over a relatively long period (Cantagrel and Robin, 1979). On Vesta, the short-lived degassing events may not have allowed time for the apatite to grow as large in Juvinas as the Durango apatite did. (2) Durango apatite has abundant (measurable by EMP) minor elements including, Sr, Na, REEs, and Si (Jarosewich et al., 1980), whereas apatite in Juvinas only has measurable Si (by EMP), most of which is probably due to secondary fluorescence from neighboring silicates. While Juvinas is depleted in Na and REEs compared to typical rhyolites (the host rock of Durango apatite), it has more Sr than rhyolites (Juvinas – 78 ppm Sr, rhyolites ~ 1-10 ppm Sr) (Barrat et al., 2007; Halliday et al., 1991; McCarthy et al., 1973; Sisson, 1991). Because Sr substitutes readily for Ca in apatite (Pan and Fleet, 2002), one would expect a relatively high Sr content in apatite (Watson and Green, 1981), but apatite in Juvinas, as well as the other eucritic apatites we studied has no measurable Sr. Thus, Sr must not have partitioned into apatite in Juvinas as readily as it does in terrestrial systems. (3) The minerals associated with Durango apatite are pyroxene, Fe-oxide, and calcite whereas apatite in Juvinas is associated with pyroxene and troilite. The high temperature fluid that crystallized

Durango apatite was rich in H₂O, the halogens and CO₂ (Lyons, 1988). If apatite in Juvinas did crystallize from a fluid, that fluid could have had lower oxygen fugacity and a higher sulfur fugacity than the fluid that crystallized Durango apatite.

The occurrence of apatite in thin veins in Juvinas is consistent with an active high temperature fluid on Vesta. This means volatiles could have played at least a local role in the near surface environment on Vesta

2.7 Eucrite apatites compared to lunar apatites

The volatile composition of lunar apatite has been extensively studied (e.g., Greenwood et al., 2008; Greenwood et al., 2011; McCubbin et al., 2011; McCubbin and Nekvasil, 2008; McCubbin et al., 2010a; McCubbin et al., 2010b; Patiño-Douce and Roden, 2006; Patiño-Douce et al., 2011), and while lunar apatite is predominately F-rich, subtle differences exist between apatites from various lunar rock types. Apatite from lunar mare basalts is generally more OH-rich and Cl-depleted compared to apatites in KREEP-bearing rocks from the lunar highlands (Figure 2.5). The F-rich apatite from lunar mare basalt has a similar volatile composition as apatite in most eucrites studied here, but apatite from lunar KREEP rocks is similar to the relatively Cl-rich apatite in GRA 98098 (Figure 2.5). Lunar mare basalts underwent varying degrees of degassing during eruption (Hauri et al., 2011; Saal et al., 2008; Sharp et al., 2010), and that is probably also true for most eucrites. Thus, lunar mare apatite and most eucritic apatite probably have similar fluorine-rich apatites due to degassing at the surface/near surface of an airless body.

The evidence for KREEP material in lunar highland breccias is often cryptic, and commonly only a geochemical signature is found. This means little actual KREEP basaltic

material exists in the collection of lunar rocks available (Warren and Wasson, 1979). The KREEP material in highland breccias is thought to be the last residual melt from a magma ocean on the Moon (Warren and Wasson, 1979). Similarly, GRA 98098 or its veins may be a late stage melt. Geochemically, these two materials (lunar KREEP and GRA 98098) are somewhat similar with elevated abundances of volatiles (K or Na), REEs, P (no bulk rock P data exists on GRA 98098, but it is more phosphate-rich than most eucrites), and have relatively Cl-rich apatite.

Most KREEP is restricted to early magmatic rocks on the Moon (4.170 - 4.418 Ga), and predates mare basalts (Arai et al., 2010; Edmunson et al., 2009; Nemchin et al., 2009; Nyquist and Shih, 1992; Palme, 1977). However, some KREEP and mare basalts crystallized contemporaneously (Taylor et al., 1983). Likewise, GRA 98098 and its veins have a crystallization age of ~4.49 Ga (Bogard and Garrison, 2003), which implies GRA 98098 and its veins crystallized at the same time as other basaltic eucrites (Bogard and Garrison, 2003; Manhes et al., 1984). As stated above, KREEP and GRA 98098 have a similar trace element and apatite compositions, but minor differences exist in detail. KREEP has ~10x the amount of REEs as lunar mare basalts (Rhodes and Hubbard, 1973; Warren and Wasson, 1979), whereas GRA 98098 has 3-5x the amount of REEs of typical eucrites (e.g., Consolmango and Drake, 1977; Warren et al., 2009). Compared to terrestrial and lunar basalts, eucrites are depleted in REEs (Consolmango and Drake, 1977; Warren and Wasson, 1979). Because REEs are not as abundant in eucrites, a residual melt on Vesta might not be as rich in the REE as KREEP. Finally, apatite in GRA 98098 is more OH-rich than apatite in KREEP. If these two lithologies were formed in a similar manner, then the difference in OH content of apatite suggests that the GRA 98098 residual melt on Vesta had a higher H₂O/F ratio than the Moon at the time of KREEP crystallization. This means Vesta could have accreted with its H₂O, or H₂O was brought to Vesta

shortly after accretion, whereas the Moon's H₂O could have arrived later (Robinson et al., 2012). In order to make a comprehensive argument that GRA 98098 is a eucritic analog to lunar KREEP and the timing of water addition to Vesta, GRA 98098 needs to be more intensively studied. Thus, we suggest GRA 98098 *could* be analogous to lunar KREEP, and it is possible that more examples of relatively Cl-rich apatites in relatively REE-rich eucritic hosts will be found.

2.8 Conclusions:

We studied apatite from 10 basaltic and 3 cumulate eucrites. The volatile content of most apatites were determined by EMP, with OH calculated by difference. In apatite from three eucrites (Moore County, EET 90020, and GRA 98098) OH was measured directly by SIMS. EMP and SIMS measurements agree within analytical error. All apatites studied are F-rich with minor OH and/or Cl. No resolvable trend exists between volatile content of apatite and trend/group (Stannern vs Nuevo Laredo) or the degree of metamorphism. Because the parental melt of most eucrites (ALH 85001, Serra De Magé, BTN 00300, LEW 88009, EET 87542, LEW 88010, EET 90020, Nuevo Laredo, and Stannern) probably degassed, the apatites are F-rich, and they provide little information on the nature of the volatiles in the interior of Vesta. The volatile composition of apatite from these eucrites closely resemble that of apatites in lunar mare basalts.

Apatite in EET 90020, Moore County, GRA 98098, and Juvinas provide the clearest evidence for an enhanced role of H₂O and Cl on Vesta. While EET 90020 is apatite-rich, the apatite enrichment probably reflects the presence of remnants of a partial melt of the coarse-grained lithology, and indicates the complexity of igneous processes on Vesta. Apatite included in pyroxene in Moore County probably equilibrated with a relatively undegassed magma, and the

apatite composition suggests that the parental melt of Moore County had more H₂O than F and Cl. We suggest that the mantle source for this eucritic magma may have had H₂O contents similar to the upper mantle of the Earth, and higher F and Cl contents. Apatite in GRA 98098 is relatively Cl-rich and occurs near silica-plagioclase veinlets whereas apatite in Juvinas occurs as crack fillings and is associated with pyroxene and troilite. Together these apatites provide evidence for high temperature hydrothermal fluids on Vesta, as suggested by Barrat et al. (2011). Finally, GRA 98098 could have a similar origin to lunar KREEP; if that is the case, further examples of Cl-rich apatites in relatively REE-rich eucrite hosts are likely to be discovered.

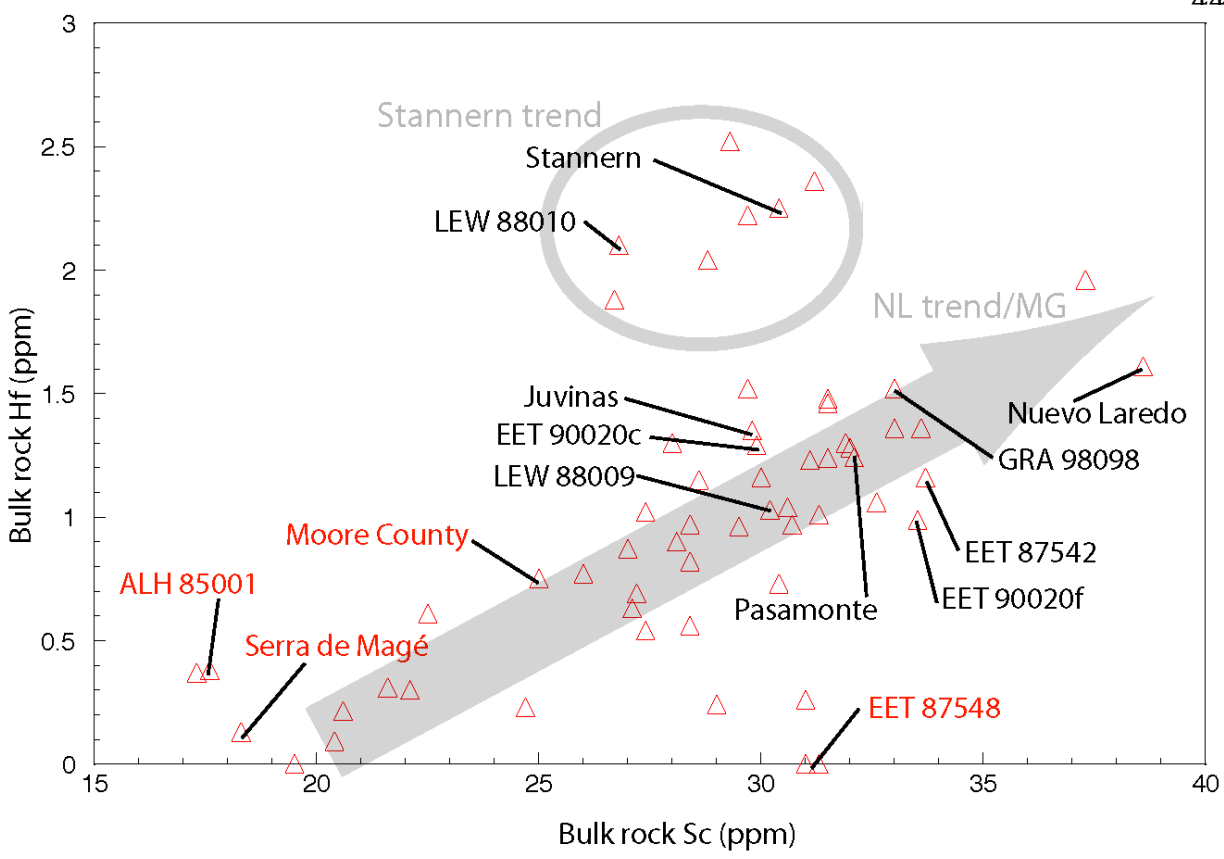


Figure 2.1: Bulk rock Hf vs. Sc for monomict and unbrecciated eucrites and Pasamonte (polymict eucrite). Labeled eucrites were selected for this study. Red labels (Moore County, Serra de Magé, ALH 85001, and EET 87548) are cumulate eucrites. Black labels are basaltic eucrites. EET 90020c is coarse-grained lithology and EET 90020f is fine-grained lithology. Stannern trend is defined by enrichment in incompatible elements that causes an excursion from the linear trend of the Nuevo Laredo trend/main group (NL trend/MG). Data from Kitts and Lodders (1998), Warren et al. (2009), and Mittlefehldt and Lindstrom (2003).

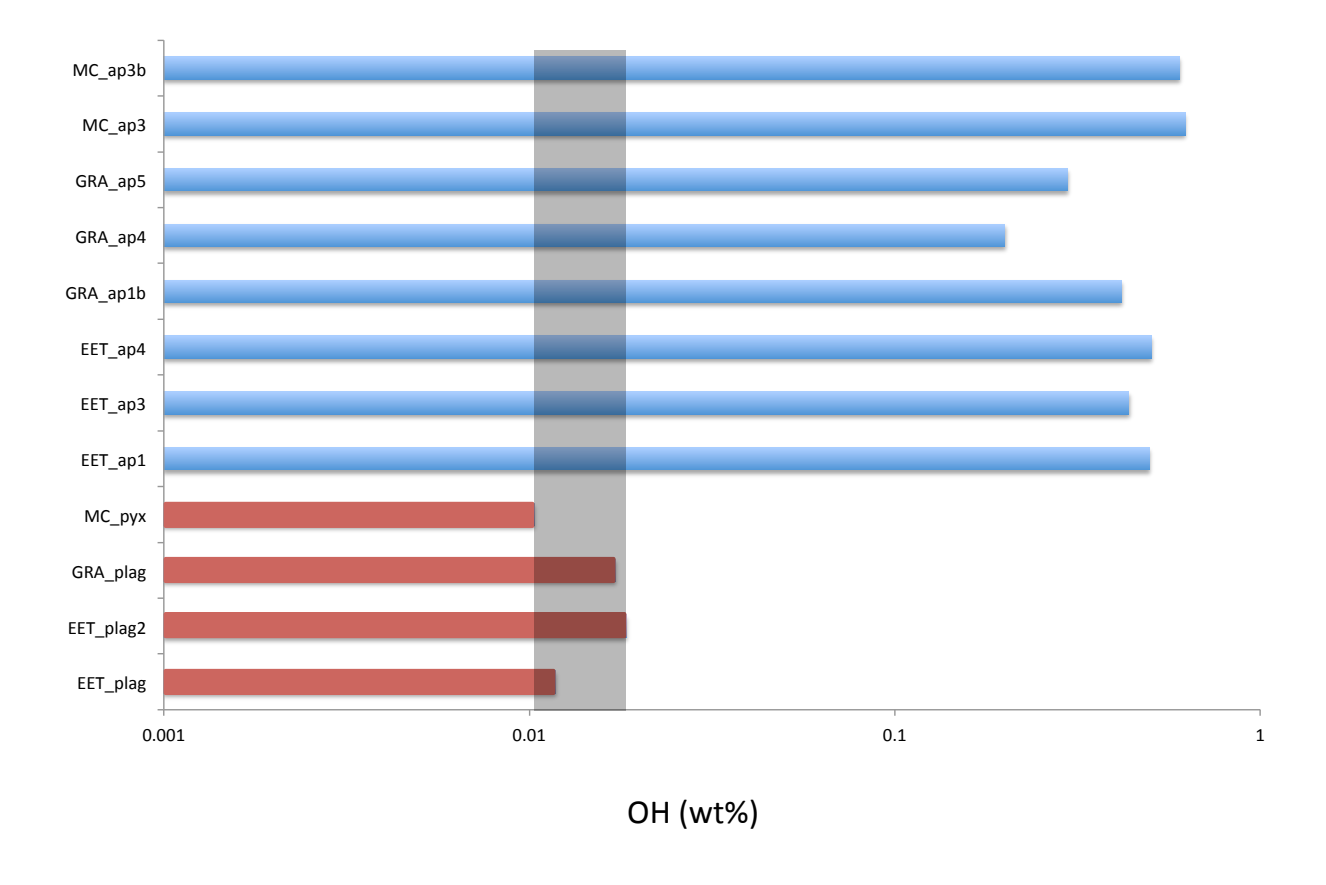


Figure 2.2: Plot of SIMS measurements of OH (wt%) in apatite, plagioclase and pyroxene. Vertical grey bars show the range of values for nominally anhydrous plagioclase and pyroxene for OH.

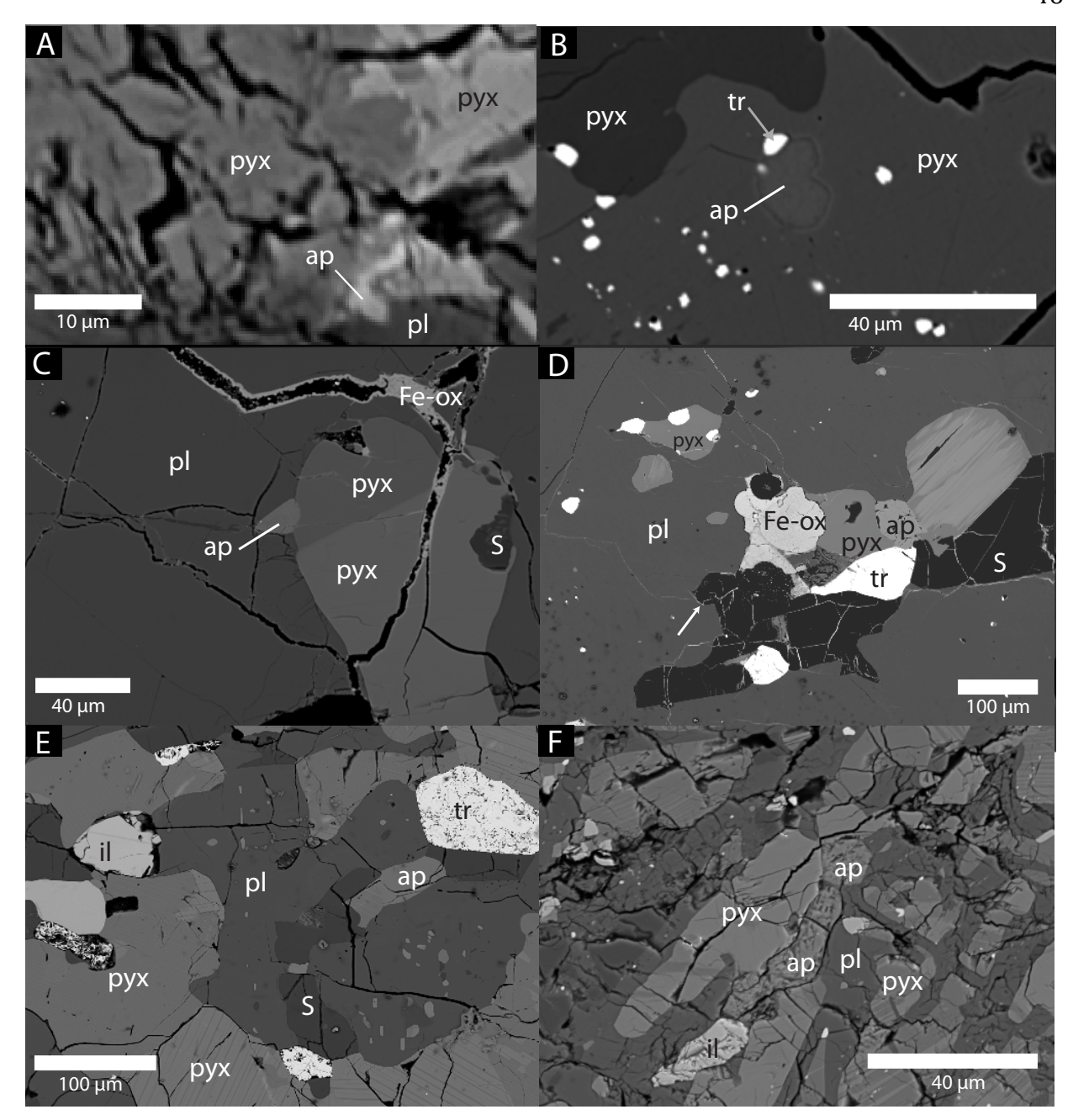


Figure 2.3 – Backscattered electron images of eucrites. (A) ALH 85001, interstitial anhedral apatite. (B) Subhedral apatite included in Moore County pyroxene. (C) Serra De Magé, subhedral apatite near crack with Fe hydroxide. (D) Serra De Magé, subhedral apatite in mesostasis. (E) BTN 00300, subhedral apatite associated with troilite and silica. (F) LEW 88009, apatite associated with ilmenite. Minerals are labeled as: ap (apatite), Fe-ox (Fe hydroxide) pl (plagioclase), pyx (pyroxene), S (silica), and tr (troilite)

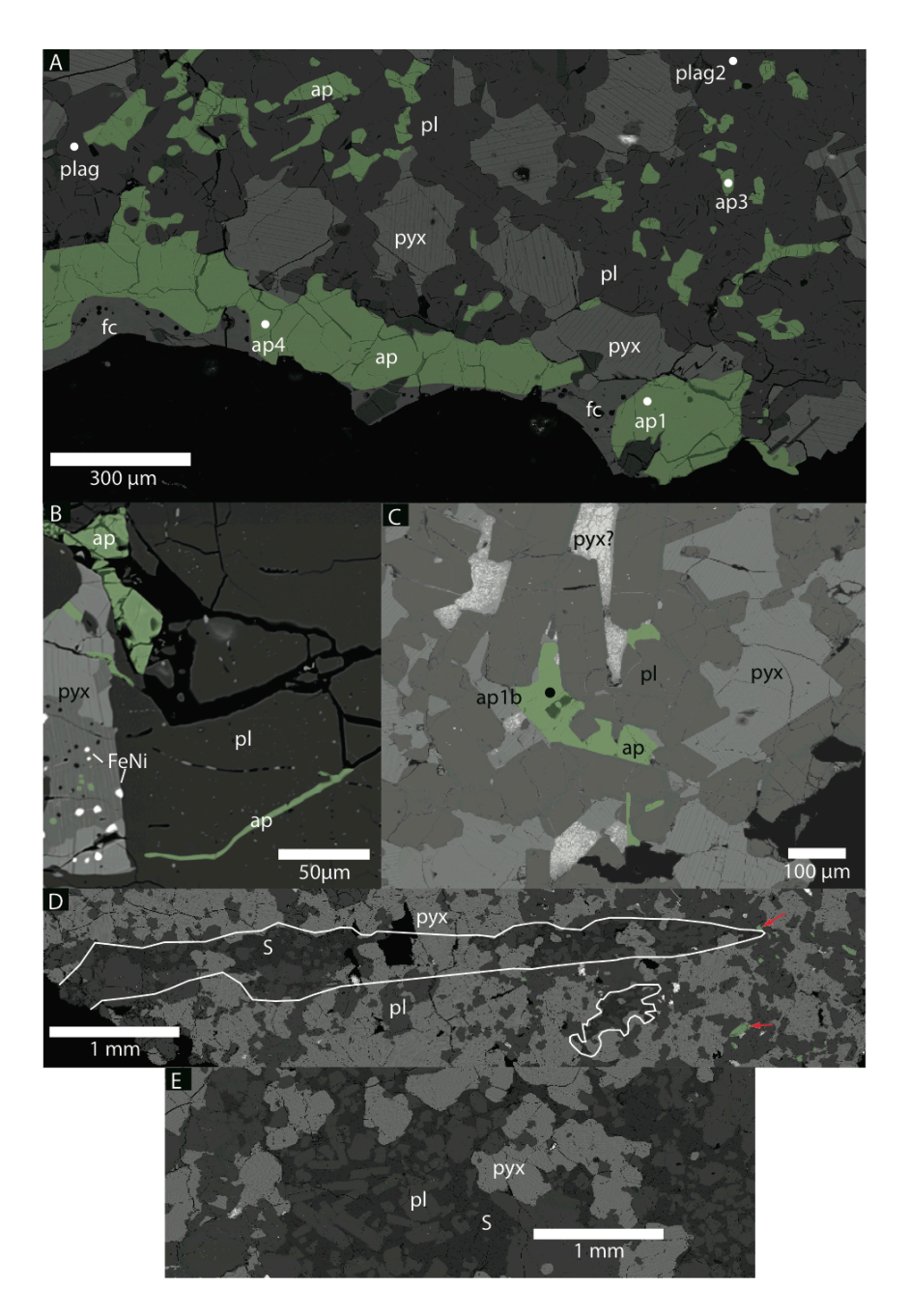


Figure 2.4 – Backscattered electron images of eucrites. Apatite is shaded green for emphasis. (A) EET 90020, apatite-rich region of coarse-grained lithology (B) Juvinas, apatite is anhedral and often occurs along cracks. (C) GRA 98098, poikilitic (white outline) silica and euhedral plagioclase associated with some apatites. Red arrows point at apatites analyzed by SIMS. (D) GRA 98098. (E) SiO₂ rich veins with euhedral plagioclase. Minerals are labeled as: ap (apatite), fc (fusion crust), FeNi (Fe-Ni metal), pl (plagioclase), pyx (pyroxene), S (silica), and tr (troilite). Circles with labels are SIMS spot analyses.

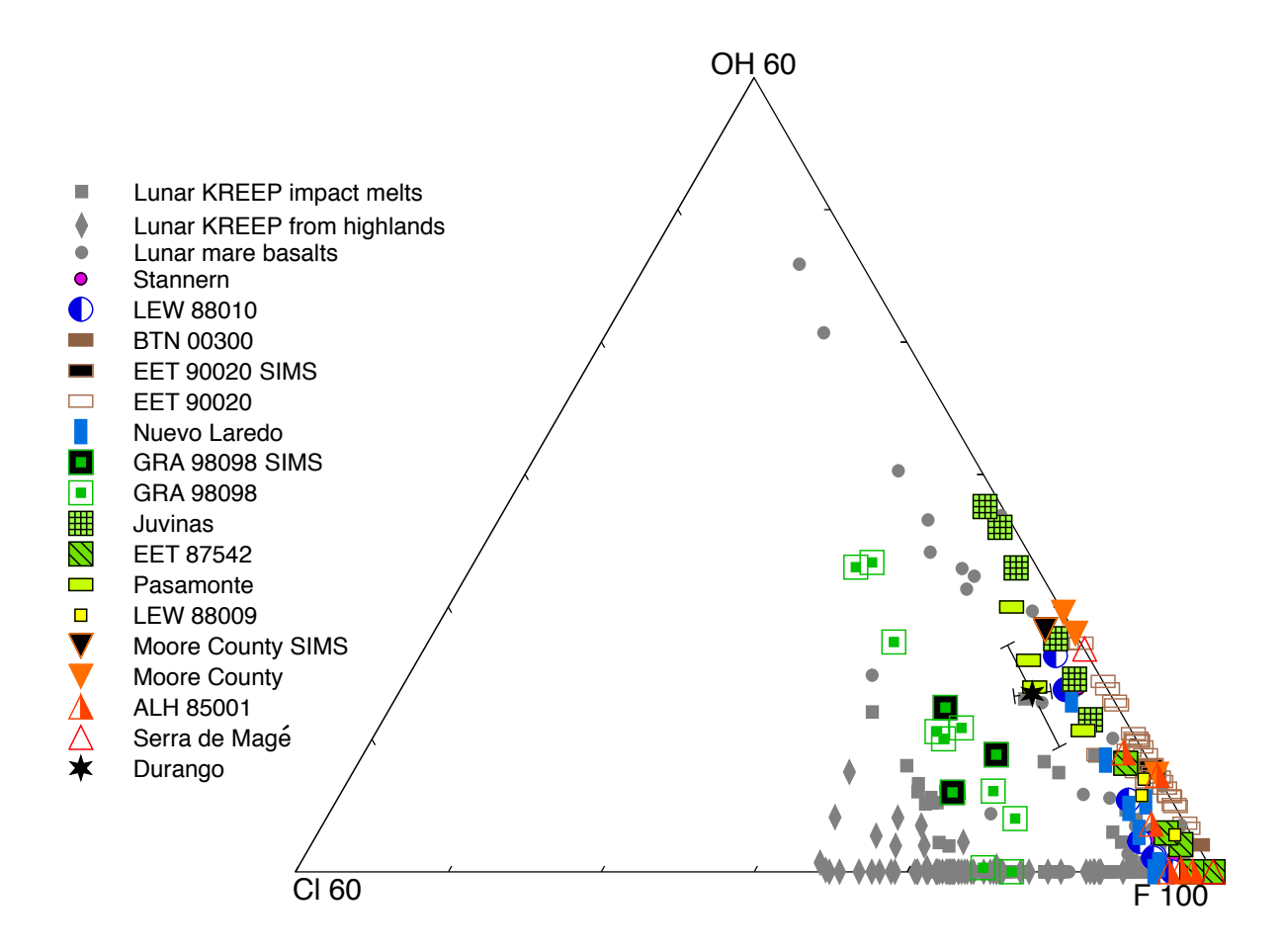


Figure 2.5 – Truncated ternary diagram of atomic proportions of F, Cl, & OH in the X site of apatite. Triangles are cumulate eucrites, squares are Nuevo Laredo trend/main group basaltic eucrites, and circles are Stannern trend basaltic eucrites. Note large variation in F-OH while Cl variation is limited for apatite in individual meteorites. Error bars (1σ) are presented for Durango and SIMS points, if error bars are absent, then the error is smaller than the symbol. Error bars on Durango are representative of error associated with EMP points. Fluorine in GRA 98098 SIMS2* analyses are calculated by difference. Lunar data from McCubbin et al. (2010a & 2011)

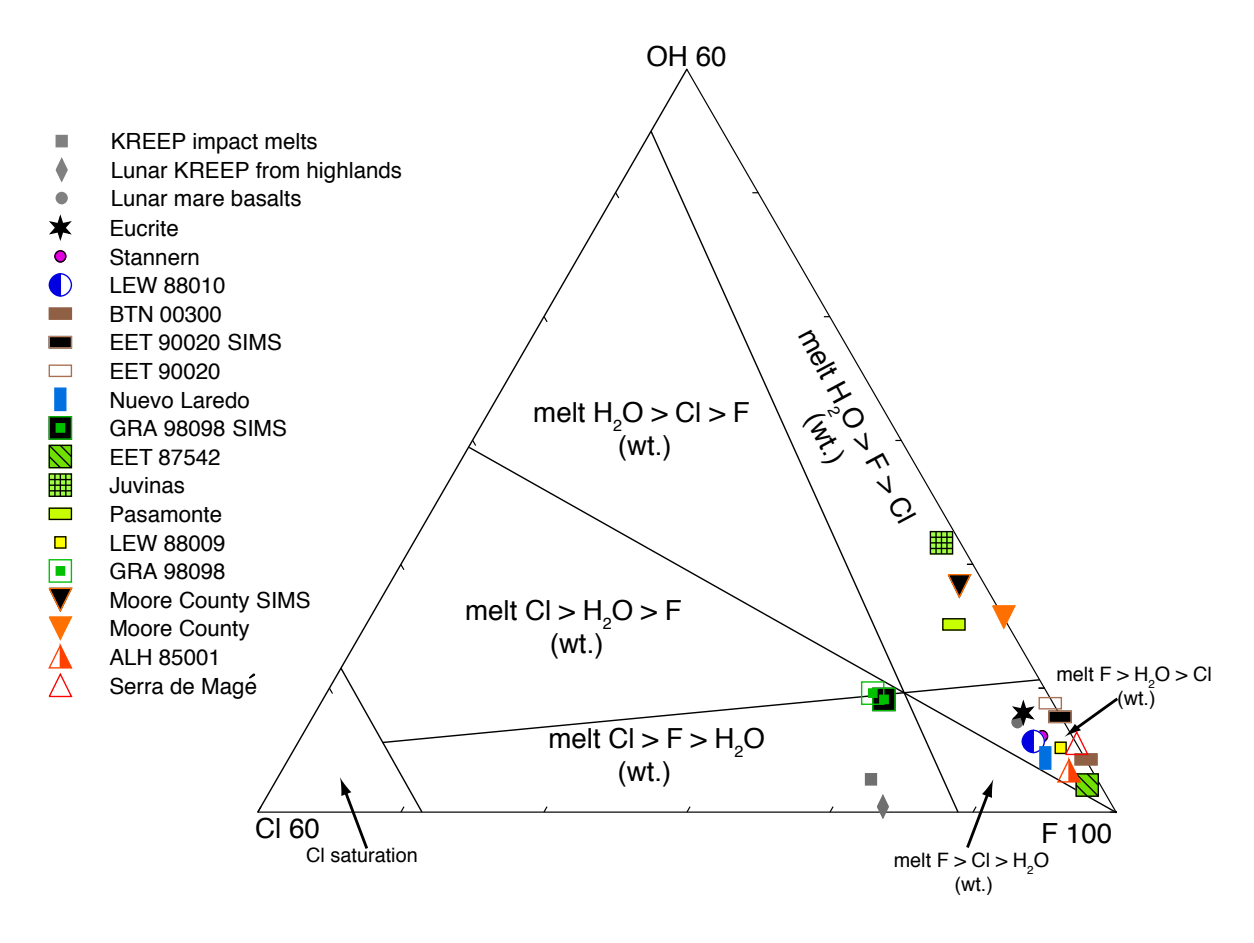


Figure 2.6 – Truncated ternary diagram of atomic proportions of F, Cl, & OH in the X site of apatite. Average composition of apatites for each eucrite, average of all eucrites, average apatite from lunar mare basalt, KREEP impact melt breccias (KREEP) and apatite from the lunar highlands (KREEP) are plotted (lunar data from McCubbin et al., 2010a, 2011). Fields show fluid-undersaturated melt compositions in equilibrium with apatites of variable compositions following McCubbin et al (2011). Triangles are cumulate eucrites, boxes are Nuevo Laredo trend/main group eucrites, and circles are Stannern trend eucrites.

Table 2.1: Representative apatite compositions measured by electron microprobe

	Serra De Magé Cumulate	Moore County Cumulate	ALH 85001 Cumulate	EET 87542 Basaltic	Nuevo Laredo Basaltic	Pasamonte Basaltic	Juvinas Basaltic	Stannern Basaltic	GRA 98098 Basaltic	LEW 88009 Basaltic
Wt%	n=3	n=4	n=6	n=6	n=7	n=4	n=5	n=6	n=11	n=3
P_2O_5	41.56	41.46	41.98	41.57	42.25	41.49	42.40	42.67	41.63	41.26
CaO	54.42	55.40	55.13	54.41	55.06	54.58	54.97	54.11	54.31	55.36
FeO	0.35	0.60	0.24	0.17	0.34	1.20	< 0.16	0.47	1.39	0.35
SiO_2	0.15	0.10	< 0.02	0.26	0.44	0.47	0.92	0.12	0.22	0.23
F	3.77	3.07	3.74	3.73	3.19	3.04	2.88	3.56	2.91	3.58
Cl	< 0.07	< 0.07	0.09	0.10	0.20	0.33	0.10	0.20	0.77	0.08
Total	100.25	100.63	101.18	100.24	101.48	101.11	101.27	101.13	101.23	100.86
O=F+C1	-1.59	-1.29	-1.60	-1.59	-1.39	-1.35	-1.24	-1.54	-1.40	-1.52
Total	98.66	99.34	99.59	98.65	100.09	99.76	100.03	99.58	99.83	99.34
apfu										
P	5.996	5.930	6.003	5.991	5.974	5.946	5.964	6.073	5.983	5.931
Ca	9.937	10.028	9.977	9.924	9.853	9.899	9.785	9.747	9.878	10.071
Fe	0.015	0.077	0.010	0.007	0.043	0.051	0.000	0.020	0.059	0.015
Si	0.025	0.016	0.000	0.045	0.074	0.080	0.153	0.021	0.038	0.039
F	2.032	1.640	1.998	2.008	1.685	1.627	1.513	1.893	1.562	1.922
C1	0.000	0.000	0.027	0.028	0.055	0.094	0.028	0.056	0.221	0.022
F+C1	2.032	1.640	2.025	2.036	1.740	1.721	1.541	1.949	1.783	1.944
Cation Total	15.973	16.051	15.990	15.966	15.944	15.976	15.902	15.860	15.958	16.057
apfu OH wt% OH	0.000 0.00	0.360 0.60	0.000 0.00	0.000 0.00	0.259 0.44	0.279 0.47	0.459 0.78	0.051 0.09	0.217 0.362	0.056 0.09
Total with OH	98.66	99.94	99.59	98.65	100.50	100.23	100.81	99.67	100.196	99.43

Table 2.1 (continued): Representative apatite compositions

	LEW 88010 Basaltic	EET 90020 Basaltic	BTN 00300 Basaltic	Durango Standard	Durango 1SD	Durango ¹ Standard	Average Wilberforce Standard	Wilberforce 1SD	Wilberforce ² Standard
Wt%	n=7	n=26	n=6	n=22		Standaru	n=30		Standard
P_2O_5	41.75	42.58	41.55	41.13	0.57	40.78	40.67	0.48	40.93
CaO	55.10	54.92	55.15	54.75	0.72	54.02	54.96	0.42	54.48
SrO	-	-	-	< 0.08	-	0.07	-	-	0.46
Na_2O	-	-	-	0.36	0.04	0.23	-	-	0.24
Ce_2O_3	-	-	-	< 0.59	-	0.50	-	-	0.31
FeO	0.40	0.19	0.60	< 0.16	-	0.06	-	-	0.5
MgO	-	-	-	< 0.06	-	0.01	-	-	0.10
SO_3	-	-	-	0.33	0.10	0.37	0.48	0.10	0.65
SiO_2	0.12	0.06	0.40	0.34	0.04	0.34	-	-	0.13
F	3.12	3.38	3.28	3.27	0.21	3.53	3.76	0.17	3.70
C1	0.20	0.00	0.00	0.34	0.05	0.41	< 0.07	-	-
Total	100.68	101.14	100.98	100.53	0.58	100.83	101.13	0.57	101.06
O=F+C1	-1.36	-1.42	-1.38	-1.45	0.09	-1.58	-1.58	0.07	-1.57
Total	99.33	99.72	99.60	99.07	0.60	99.25	99.55	0.55	99.49
apfu									
P	5.979	6.042	5.940	5.902	0.060	5.899	5.857	0.040	5.874
Ca	9.987	9.862	9.978	9.943	0.138	9.889	9.957	0.092	9.896
Sr	-	-	_	-	0.005	0.007	-	-	0.045
Na	-	-	-	0.118	0.012	0.076	-	-	0.079
Ce	-	_	-	_	-	0.031	-	-	0.019
Fe	0.017	0.008	0.025	-	-	0.008	-	-	0.002

Mg	-	-	-	-	-	0.003	-	-	0.003
S	-	-	-	0.042	0.014	0.047	0.074	0.012	0.083
Si	0.020	0.011	0.068	0.058	0.008	0.058	-	-	0.022
F	1.669	1.791	1.751	1.753	0.110	1.907	1.905	0.091	1.984
Cl	0.056	0.000	0.000	0.098	0.016	0.119	0.000	0.000	0.014
F+Cl	1.725	1.791	1.751	1.851	0.113	2.026	1.905	0.091	1.998
Cation Total	16.003	15.923	16.010	16.064	0.084	16.018	16.068	0.056	16.028
apfu OH	0.275	0.209	0.249	0.080	0.002	-0.022	0.098	0.086	0.002
wt% OH	0.46	0.35	0.42	0.13	0.003	-0.04	0.16	0.14	0.003
Total with OH	99.79	100.07	100.01	99.20	0.69	99.21	99.56	0.56	99.494

Table 2.1 – - not measured, ¹Durango from Jarosewich et al. (1980)¹. ²Wilberforce from C.M. Taylor, C.M. Taylor Company

Table~2.2-Apatite~volatile~concentrations~(wt%)~determined~by~SIMS

Sample	Spot	ОН	F	Cl
EET 90020	ap1	0.497	3.447	0.005
EET 90020	ap3	0.437	3.557	0.004
EET 90020	ap4	0.503	3.534	0.009
GRA 98098	ap1b	0.418	2.864	0.767
GRA 98098	ap4	0.200	2.975	0.946
GRA 98098	ap5	0.297	3.044	0.661
Moore County	ap3	0.622	3.028	0.126
Moore County	ap3b	0.602	2.931	0.123

REFERENCES:

Arai, T., Yoshitake, M., Tomiyama, T., Niihara, T., Yokoyama, T., Kaiden, H., Misawa, K., Irving, A., 2010. Support for a Prolonged KREEP Magmatism: U-Pb Age Dating of Zircon and Baddeleyite in Lunar Meteorite NWA 4485, 41st Lunar and Planetary Science Conference, p. 2379.

Armellini, F.J., Tester, J.W., 1993. Solubility of sodium chloride and sulfate in sub-and supercritical water vapor from 450-550 C and 100-250 bar. Fluid phase equilibria 84, 123-142.

Asmar, S., Konopliv, A., Park, R., Bills, B., Gaskell, R., Raymond, C., Russell, C., Smith, D., Toplis, M., Zuber, M., 2012. The Gravity Field of Vesta and Implications for Interior Structure, 42nd Lunar and Planetary Science Conference, p. 2600.

Barrat, J., Yamaguchi, A., Greenwood, R., Bohn, M., Cotten, J., Benoit, M., Franchi, I., 2007. The Stannern trend eucrites: Contamination of main group eucritic magmas by crustal partial melts. Geochimica et Cosmochimica Acta 71, 4108-4124.

Barrat, J.A., Yamaguchi, A., Bollinger, C., Boudouma, O., submitted. Low-Mg rock debris in howardites: Evidence for KREEPy lithologies on Vesta? Geochimica et Cosmochimica Acta.

Barrat, J.A., Yamaguchi, A., Bunch, T., Bohn, M., Bollinger, C., Ceuleneer, G., 2011. Possible fluid-rock interactions on differentiated asteroids recorded in eucritic meteorites. Geochimica et Cosmochimica Acta, 3839–3852.

Bogard, D., Garrison, D., 1997. 39Ar-40Ar ages of igneous non-brecciated eucrites, 28th Lunar and Planetary Science Conference, pp. 127-128.

Bogard, D.D., Garrison, D.H., 2003. 39Ar-40Ar ages of eucrites and thermal history of asteroid 4 Vesta. Meteoritics & Planetary Science 38, 669-710.

Boudreau, A.E., McCallum, I.S., 1989. Investigations of the Stillwater Complex: Part V. Apatites as indicators of evolving fluid composition. Contributions to Mineralogy and Petrology 102, 138-153.

Boyce, J.W., Eiler, J.M., Channon, M.B., in press. An inversion-based self-calibration for SIMS measurements: Application to H, F, and Cl in apatite. American Mineralogist.

Boyce, J.W., Liu, Y., Rossman, G.R., Guan, Y., Eiler, J.M., Stolper, E.M., Taylor, L.A., 2010. Lunar apatite with terrestrial volatile abundances. Nature 466, 466-469.

Brenan, J.M., 1993. Partitioning of fluorine and chlorine between apatite and aqueous fluids at high pressure and temperature: implications for the F and Cl content of highP-T fluids. Earth and Planetary Science Letters 117, 251-263.

Broman, C., Martinsson, O., 2000. Fluid inclusions in epigenetic Fe-Cu-Au ores in northern Norrbotten, 2nd annual GEODE-Fennoscandian shield field workshop on Palaeoproterozoic and Archaean greenstone belts and VMS districts in the Fennoscandian Shield, pp. 6-7.

BVSP, 1981. Basaltic Volcanism on the Terrestrial Planets. Pergam Press Inc., New York.

Cantagrel, J.M., Robin, C., 1979. K-Ar dating on eastern Mexican volcanic rocks--Relations between the andesitic and the alkaline provinces. Journal of Volcanology and Geothermal Research 5, 99-114.

Carroll, M.R., Webster, J.D., 1994. Solubilities of sulfur, noble gases, nitrogen, chlorine, and fluorine in magmas, in: Carroll, M.R., Holloway, J.R. (Eds.), Volatiles in Magmas, Reviews in Mineralogy, Washington, DC, pp. 231-279.

Clayton, R.N., 1993. Oxygen isotopes in meteorites. Annual Review of Earth and Planetary Sciences 21, 115-149.

Clayton, R.N., 1996. Oxygen isotope studies of achondrites. Geochimica et Cosmochimica Acta 60, 1999-2017.

Clayton, R.N., 2003. Oxygen isotopes in the solar system. Space Science Reviews 106, 19-32.

Clayton, R.N., Mayeda, T.K., 1983. Oxygen isotopes in eucrites, shergottites, nakhlites, and chassignites. Earth and Planetary Science Letters 62, 1-6.

Clayton, R.N., Onuma, N., Mayeda, T.K., 1976. A classification of meteorites based on oxygen isotopes. Earth and Planetary Science Letters 30, 10-18.

Consolmango, G.J., Drake, M.J., 1977. Composition and evolution of the eucrite parent body: Evidence from rare earth elements. Geochimica et Cosmochimica Acta 41, 1271-1282.

Delaney, J.S., O'Neill, C., Prinz, M., 1984. Phosphate minerals in eucrites, 15th Lunar and Planetary Science Conference, p. 208.

Drake, M.J., Horton, N.E., Capobianco, C.J., 1989. V, Cr, and Mn in the Earth, Moon, EPB, and SPB and the origin of hte Moon: Experimental studies. Geochimica et Cosmochimica Acta 53, 2101-2111.

Duke, M.B., Silver, L.T., 1967. Petrology of eucrites, howardites and mesosiderites. Geochimica et Cosmochimica Acta 31, 1637-1665.

Edmunson, J., Borg, L., Nyquist, L., Asmerom, Y., 2009. A combined Sm-Nd, Rb-Sr, and U-Pb isotopic study of Mg-suite norite 78238: Further evidence for early differentiation of the Moon. Geochimica et Cosmochimica Acta 73, 514-527.

Flynn, R.T., Wayne Burnham, C., 1978. An experimental determination of rare earth partition coefficients between a chloride containing vapor phase and silicate melts. Geochimica et Cosmochimica Acta 42, 685-701.

Giordano, D., Romano, C., Dingwell, D., Poe, B., Behrens, H., 2004. The combined effects of water and fluorine on the viscosity of silicic magmas. Geochimica et Cosmochimica Acta 68, 5159-5168.

Goodrich, C.A., Delaney, J.S., 2000. Fe/Mg–Fe/Mn relations of meteorites and primary heterogeneity of primitive achondrite parent bodies. Geochimica et Cosmochimica Acta 64, 149-160.

Greenwood, J.P., Itoh, S., Sakamoto, N., Vicenzi, E.P., Yurimoto, H., 2008. Hydrogen isotope evidence for loss of water from Mars through time. Geophysical Research Letters 35, L05203.

Greenwood, J.P., Itoh, S., Sakamoto, N., Warren, P., Taylor, L., Yurimoto, H., 2011. Hydrogen isotope ratios in lunar rocks indicate delivery of cometary water to the Moon. Nature Geoscience 4, 79-82.

Greenwood, R., Franchi, I., Jambon, A., Barrat, J., Burbine, T., 2006. Oxygen isotope variation in stony-iron meteorites. Science 313, 1763-1765.

Greenwood, R.C., Franchi, I.A., Jambon, A., Buchanan, P.C., 2005. Widespread magma oceans on asteroidal bodies in the early Solar System. Nature 435, 916-918.

Groat, L.A., Raudsepp, M., Hawthorne, F.C., Ercit, T.S., Sherriff, B.L., Hartman, J.S., 1990. The amblygonite-montebrasite series: Characterization by single-crystal structure refinement, infrared spectroscopy, and multinuclear MAS-NMR spectroscopy. American Mineralogist 75, 992-1008.

Halliday, A., Davidson, J.P., Hildreth, W., Holden, P., 1991. Modelling the petrogenesis of high Rb/Sr silicic magmas. Chemical Geology 92, 107-114.

Harlow, G., Klimentidis, R., 1980. Clouding of pyroxene and plagioclase in eucrites-Implications for post-crystallization processing, 11th Lunar and Planetary Science Conference, pp. 1131-1143.

Hauri, E., Wang, J., Dixon, J.E., King, P.L., Mandeville, C., Newman, S., 2002. SIMS analysis of volatiles in silicate glasses: 1. Calibration, matrix effects and comparisons with FTIR. Chemical Geology 183, 99-114.

Hauri, E.H., Weinreich, T., Saal, A.E., Rutherford, M.C., Van Orman, J.A., 2011. High preeruptive water contents preserved in lunar melt inclusions. Science 333, 213-215.

Henderson, C., 2011. Protocals and pitfalls of electron microprobe analysis of apatite, Geological Sciences. University of Michigan thesis, p. 68.

Hess, H.H., Henderson, F.P., 1949. The Moore County meteorite: A further study with comment on its primordial environment. American Mineralogist 34, 494-507.

Hiroi, T., Pieters, C.M., Takeda, H., 1994. Grain size of the surface regolith of asteroid 4 Vesta estimated from its reflectance spectrum in comparison with HED meteorites. Meteoritics 29, 394-396.

Hirose, K., Kawamoto, T., 1995. Hydrous partial melting of lherzolite at 1 GPa: the effect of H2O on the genesis of basaltic magmas. Earth and Planetary Science Letters 133, 463-473.

Hsu, W., Crozaz, G., 1996. Mineral chemistry and the petrogenesis of eucrites: I. Noncumulate eucrites. Geochimica et Cosmochimica Acta 60, 4571-4591.

Jarosewich, E., Nelen, J.A., Norberg, J.A., 1980. Reference samples for electron microprobe analysis. Geostandards Newsletter 4, 43-47.

Jones, R.H., McCubbin, F.M., Dreeland, L., Guan, Y., 2011. Phosphate minerals in type 4-5 LL chondrites: The nature of fluids on the LL chondrite parent body, 42nd Lunar and Planetary Science Confrence, p. 2464.

Karner, J., Papike, J., Shearer, C., 2006. Comparative planetary mineralogy: Pyroxene major-and minor-element chemistry and partitioning of vanadium between pyroxene and melt in planetary basalts. American Mineralogist 91, 1574—1582.

Kitts, K., Lodders, K., 1998. Survey and evaluation of eucrite bulk compositions. Meteoritics & Planetary Science 33, A197-A213.

Kleine, T., Mezger, K., Palme, H., Scherer, E., Munker, C., 2005. The W isotope composition of eucrite metals: Constraints on the timing and cause of the thermal metamorphism of basaltic eucrites. Earth and Planetary Science Letters 231, 41-52.

Lodders, K., 2003. Solar system abundances and condensation temperatures of the elements. The Astrophysical Journal 591, 1220.

Lyons, J.I., 1988. Volcanogenic iron oxide deposits, Cerro de Mercado and vicinity, Durango. Economic Geology 83, 1886-1906.

Manhes, G., Allègre, C., Provost, A., 1984. U--Th--Pb systematics of the eucrite "Juvians": Precise age determination and evidence for exotic lead Geochimica et Cosmochimica Acta 48, 2247-2264.

Mathez, E.A., Webster, J.D., 2005. Partitioning behavior of chlorine and fluorine in the system apatite–silicate melt–fluid. Geochimica et Cosmochimica Acta 69, 1275-1286.

Mayne, R.G., McSween Jr., H.Y., McCoy, T.J., Gale, A., 2009. Petrology of the unbrecciated eucrites. Geochimica et Cosmochimica Acta 73, 794-819.

McCarthy, T.S., Erlank, A.J., Willis, J.P., 1973. On the origin of eucrites and diogenites. Earth and Planetary Science Letters 18, 433-442.

McCollom, T.M., Shock, E.L., 1998. Fluid-rock interactions in the lower oceanic crust: Thermodynamic models of hydrothermal alteration. Journal of Geophysical Research 103, 547-575.

McCubbin, F., Hauri, E., Elardo, S., Vander Kaaden, K., Wang, J., Shearer, C., 2012. Hydrous Melting of the Martian Mantle Produced Both Depleted and Enriched Shergottites, 43rd Lunar and Planetary Science Confrence, p. 1121.

McCubbin, F.M., Jolliff, B.L., Nekvasil, H., Carpenter, P.K., Zeigler, R.A., Steele, A., Elardo, S.M., Lindsley, D.H., 2011. Fluorine and chlorine abundances in lunar apatite: Implications for heterogeneous distributions of magmatic volatiles in the lunar interior. Geochimica et Cosmochimica Acta 75, 5073-5093.

McCubbin, F.M., Nekvasil, H., 2008. Maskelynite-hosted apatite in the Chassigny meteorite: Insights into late-stage magmatic volatile evolution in martian magmas. American Mineralogist 93, 676-684.

McCubbin, F.M., Steele, A., Hauri, E.H., Nekvasil, H., Yamashita, S., Hemley, R., 2010a.

Nominally hydrous magmatism on the Moon. Procedings of the National Academy of Sciences of the United States of America 107, 11223-11228.

McCubbin, F.M., Steele, A., Nekvasil, H., Schnieders, A., Rose, T., Fries, M., Carpenter, P.K., Jolliff, B.L., 2010b. Detection of structurally bound hydroxyl in fluorapatite from Apollo Mare basalt 15058, 128 using TOF-SIMS. American Mineralogist 95, 1141.

McSween, H.Y., Mittlefehldt, D.W., Beck, A.W., Mayne, R.G., McCoy, T.J., 2010. HED meteorites and their relationship to the geology of Vesta and the Dawn Mission. Space Science Reviews, 1-34.

Misawa, K., Yamaguchi, A., Hiroshi, K., 2005. U-Pb and 207Pb-206Pb ages of zircons from basaltic eucrites: Implications for early basaltic volcanism on the eucrite parent body.

Geochimica et Cosmochimica Acta 69, 5847-5861.

Mittlefehldt, D., Galindo Jr, C., 2002. Petrology and Geochemistry of Unbrecciated, Metamorphosed Eucrites. Meteoritics and Planetary Science Supplement 37, 101.

Mittlefehldt, D., Lee, M., 2001. Petrology and geochemistry of unusual eucrite GRA 98098. Meteoritics and Planetary Science Supplement 36, 136.

Mittlefehldt, D.W., 1979. Petrographic and chemical characterization of igneous lithic clasts from mesosiderites and howardites and comparison with eucrites and diogenites. Geochimica et Cosmochimica Acta 43, 1917-1936.

Mittlefehldt, D.W., 1987. Volatile degassing of basaltic achondrite parent bodies: Evidence from alkali elements and phosphorus. Geochimica et Cosmochimica Acta 51, 267-278.

Mittlefehldt, D.W., 2005. Ibitira: A basaltic achondrite from a distinct parent asteroid and implications for the Dawn Mission. Meteoritics & Planetary Science 40, 665–677.

Mittlefehldt, D.W., Lindstrom, M.M., 2003. Geochemistry of eucrites: genesis of basaltic eucrites, and Hf and Ta as petrogenetic indicators for altered antarctic eucrites. Geochimica et Cosmochimica Acta 67, 1911-1934.

Miyamoto, M., Duke, M.B., McKay, D.S., 1985. Chemical zoning and homogenization of Pasamonte-type pyroxene and their bearing on thermal metamorphism of a howardite parent body. Journal of Geophysical Research 90, C629-C635.

Nemchin, A., Timms, N., Pidgeon, R., Geisler, T., Reddy, S., Meyer, C., 2009. Timing of crystallization of the lunar magma ocean constrained by the oldest zircon. Nature Geoscience 2, 133-136.

Newsom, H.E., 1995. Composition of the solar system, planets, meteorites, and major terrestrial reservoirs, in: Ahrens, T.J. (Ed.), Global Earth Physics: A Handbook of Physical Constrants AGU, pp. 159-189.

Newsom, H.E., Taylor, S.R., 1989. Geochemical implications of the formation of the Moon by a single giant impact. Nature 338, 29-34.

Nyquist, L., Shih, C.Y., 1992. The isotopic record of lunar volcanism. Geochimica et Cosmochimica Acta 56, 2213-2234.

O'Reilly, S.Y., Griffin, W., 2000. Apatite in the mantle: Implications for metasomatic processes and high heat production in Phanerozoic mantle. Lithos 53, 217-232.

Palme, H., 1977. On the age of KREEP. Geochimica et Cosmochimica Acta 41, 1791-1801.

Pan, Y., Fleet, M.E., 2002. Compositions of the apatite-group Minerals: Substitution mechanisms and controlling factors. Reviews in Mineralogy & Geochemistry 48, 13-49.

Papike, J.J., 1998. in: Papike, J.J. (Ed.), Reviews in Mineralogy: Planetary Materials. Mineralogical Society of America, Washington, D.C., pp. 7-01-07-10.

Papike, J.J., Karner, J.M., Shearer, C.K., 2003. Determination of planetary basalt parentage: A simple technique using the electron microprobe. American Mineralogist 88, 469-472.

Patiño-Douce, A.E., Roden, M., 2006. Apatite as a probe of halogen and water fugacities in the terrestrial planets. Geochimica et Cosmochimica Acta 70, 3173-3196.

Patiño-Douce, A.E., Roden, M.F., Chaumba, J., Fleisher, C., Yogodzinski, G., 2011.

Compositional variability of terrestrial mantle apatites, thermodynamic modeling of apatite volatile contents, and the halogen and water budgets of planetary mantles. Chemical Geology.

Peplowski, P.N., Evans, L.G., Hauck II, S.A., McCoy, T.J., Boynton, W.V., Gillis-Davis, J.J., Ebel, D.S., Goldsten, J.O., Hamara, D.K., Lawrence, D.J., 2011. Radioactive elements on Mercuryis surface from MESSENGER: Implications for the planetis formation and evolution. Science 333, 1850-1852.

Piccoli, P., Candela, P., 1994. Apatite in felsic rocks: A model for the estimation of inital halogen concentrations in the Biship Tuff (Long Vally) and Tuolumne Intrusive Suite (Sierra Nevada Batholith) magmas. American Journal of Science 294, 92-135.

Piccoli, P.M., Candela, P.A., 2002. Apatite in igneous systems. Reviews in Mineralogy & Geochemistry 48, 255-292.

Prinz, M., Nehru, C., Berkley, J., Keil, K., Jarosewich, E., Gomes, C., 1977. Petrogenesis of the Serra de Mage cumulate eucrite. Meteoritics and Planetary Science Supplement 12, 341.

Python, M., Ceuleneer, G., Ishida, Y., Barrat, J.A., Arai, S., 2007. Oman diopsidites: A new lithology diagnostic of very high temperature hydrothermal circulation in mantle peridotite below oceanic spreading centres. Earth and Planetary Science Letters 255, 289-305.

Rayman, M.D., C., F.T., Raymond, C.A., Russell, C.T., 2006. Dawn: A mission in development for exploration of main belt asteroids Vesta and Ceres. Acta Astronautica 58, 605-616.

Rhodes, J., Hubbard, N., 1973. Chemistry, classification, and petrogenesis of Apollo 15 mare basalts, 4th Lunar and Planetart Sciecne Conference, p. 1127.

Righter, K., Drake, M.J., 1997. A magma ocean on Vesta: Core formation and petrogenesis of eucrites and diogenites. Meteoritics & Planetary Science 32, 929-944.

Robinson, K., Taylor, G., Hellebrand, E., Nagashima, K., 2012. Water in evolved lunar rocks: Implications for water distribution in the lunar mantle, 43rd Lunar and Planetary Science Confrence, p. 1727.

Russell, C., Raymond, C., Jaumann, R., McSween, H., 2012. Dawn at Vesta: Accomplishments and Plans, p. 1633.

Saal, A.E., Hauri, E.H., Cascio, M.L., Van Orman, J.A., Rutherford, M.C., Cooper, R.F., 2008. Volatile content of lunar volcanic glasses and the presence of water in the Moonis interior. Nature 454, 192-195.

Saal, A.E., Hauri, E.H., Langmuir, C.H., Perfit, M.R., 2002. Vapour undersaturation in primitive mid-ocean-ridge basalt and the volatile content of Earth's upper mantle. Nature 419, 451-455.

Salters, V.J.M., Stracke, A., 2004. Composition of the depleted mantle. Geochemistry Geophysics Geosystems 5, Q05B07.

Sarafian, A.R., Roden, M.F., Patiño-Douce, A.E., 2012. The nature of volatiles in vesta: Clues from apatite in eucrites, 43nd Lunar and Planetary Science Conference, p. 1175.

Scott, E.R.D., Greenwood, R.C., Franchi, I.A., Sanders, I.S., 2009. Oxygen isotopic constraints on the origin and parent bodies of eucrites, diogenites, and howardites. Geochimica et Cosmochimica Acta 73, 5835-5853.

Sharp, Z., Shearer, C., McKeegan, K., Barnes, J., Wang, Y., 2010. The chlorine isotope composition of the moon and implications for an anhydrous mantle. Science 329, 1050-1053.

Sisson, T., 1991. Pyroxene-high silica rhyolite trace element partition coefficients measured by ion microprobe. Geochimica et Cosmochimica Acta 55, 1575-1585.

Stolper, E., 1977. Experimental petrology of eucritic meteorites. Geochimica et Cosmochimica Acta 41, 587-611.

Stormer, J., Pierson, M., Tacker, R., 1993. Variation of F and Cl X-ray intensity due to anisotropic diffusion in apatite. American Mineralogist 78, 641-664S.

Takeda, H., 1997. Mineralogical records of early planetary processes on the howardite, eucrite, diogenite parent body with reference to Vesta. Meteoritics & Planetary Science 32, 841-853.

Takeda, H., Graham, A., 1991. Degree of equilibration of eucritic pyroxenes and thermal metamorphism of the earliest planetary crust. Meteoritics 26, 129-134.

Takeda, H., Mori, H., Delaney, J., Prinz, M., Harlow, G., 1983. Mineralogical comparison of Antarctic and non-Antarctic HED (howardites-eucrites-diogenites) achondrites. National Institute Polar Research Memoirs 30, 181-205.

Tatsumoto, M., Knight, R.J., Allegre, C.J., 1973. Time differences in the formation of meteorites as determined from the ratio of lead-207 to lead-206. Science 180, 1279.

Taylor, L.A., Shervais, J.W., Hunter, R.H., Shih, C.Y., Bansal, B., Wooden, J., Nyquist, L., Laul, L., 1983. Pre-4.2 AE mare-basalt volcanism in the lunar highlands. Earth and Planetary Science Letters 66, 33-47.

Tera, F., Carlson, R.W., Boctor, N.Z., 1997. Radiometric ages of basaltic achondrites and their relation to the early history of the solar system. Geochimica et Cosmochimica Acta 61, 1713-1731.

Treiman, A.H., Lanzirotti, A., Xirouchakis, D., 2004. Ancient water on asteroid 4 Vesta: Evidence from a quartz veinlet in the Serra de Magé eucrite meteorite. Earth and Planetary Science Letters 219, 189-199.

Trinquier, A., Birck, J.L., Allègre, C., Göpel, C., Ulfbeck, D., 2008. 53Mn-53Cr systematics of the early solar system revisited. Geochimica et Cosmochimica Acta 72, 5146-5163.

Wadhwa, M., 2008. Redox conditions on small bodies, the Moon and Mars. Reviews in Mineralogy and Geochemistry 68, 493-510.

Warren, H., Kallemeyn, W., 2001. A correlation between erupted lava compositions and degree of subsequent thermal metamorphism for the HED-meteroritic basalts, 32nd Lunar and Planetart Science Conference, p. 154.

Warren, P., 1997. Magnesium oxide-iron oxide mass balance constraints and a more detailed model for the relationship between eucrites and diogenites. Meteoritics & Planetary Science 32, 945-963.

Warren, P.H., Jerde, E.A., 1987. Composition and origin of Nuevo Laredo trend eucrites. Geochimica et Cosmochimica Acta 51, 713-725.

Warren, P.H., Kallemeyn, G.W., Huber, H., Ulff-Møller, F., Choe, W., 2009. Siderophile and other geochemical constraints on mixing relationships among HED-meteoritic breccias.

Geochimica et Cosmochimica Acta 73, 5918–5943.

Warren, P.H., Kallemeyn, W., Arai, T., Kaneda, K., 1996. Compositional-petrologic investigation of eucrites and the QUE94201 Shergottite, 21st symposium on Antarctic meteorites, p. 195.

Warren, P.H., Wasson, J.T., 1979. The origin of KREEP. Reviews of Geophysics 17, 73-88.

Watson, E.B., Green, T.H., 1981. Apatite/liquid partition coefficients for the rare earth elements and strontium. Earth and planetary Science Letters 56, 405-421.

Wiechert, U., Halliday, A., Palme, H., Rumble, D., 2004. Oxygen isotope evidence for rapid mixing of the HED meteorite parent body. Earth and Planetary Science Letters 221, 373-382.

Wyllie, P., Cox, K., Biggar, G., 1962. The habit of apatite in synthetic systems and igneous rocks. Journal of Petrology 3, 238-243.

Yamaguchi, A., Barrat, J., Greenwood, R., Shirai, N., Okamoto, C., Setoyanagi, T., Ebihara, M., Franchi, I., Bohn, M., 2009. Crustal partial melting on Vesta: Evidence from highly metamorphosed eucrites. Geochimica et Cosmochimica Acta 73, 7162-7182.

Yamaguchi, A., Taylor, G.J., Keil, K., 1996. Global crustal metamorphism of the eucrite parent body. Icarus 124, 97-112.

Yamaguchi, A., Taylor, G.J., Keil, K., Floss, C., Crozaz, G., Nyquist, L.E., Bogard, D.D., Garrison, D.H., Reese, Y.D., Wiesmann, H., 2001. Post-crystallization reheating and partial melting of eucrite EET90020 by impact into the hot crust of asteroid 4Vesta 4.50 Ga ago. Geochimica et Cosmochimica Acta 65, 3577-3599.

APPENDIX

	cumulate	cumulate	cumulate	cumulate
Pt#	Serra dé Mage	Serra dé Mage	Serra dé Mage	Moore County
P2O5	41.72	41.91	41.56	42.24
CaO	54.78	54.48	54.42	56.26
SrO	< 0.08	-	-	<0.08
Na2O	< 0.10	-	-	< 0.10
Ce2O3	< 0.59	-	-	< 0.59
FeO	1.35	0.27	0.35	0.21
MgO	0.15	-	-	< 0.06
SO3	< 0.06	-	-	< 0.06
Y2O3	< 0.21	-	-	< 0.21
As	< 0.9	-	-	< 0.9
SiO2	1.18	0.13	0.15	< 0.02
F	3.18	3.80	3.77	3.11
Cl	< 0.07	< 0.07	< 0.07	< 0.07
Total	102.36	100.59	100.25	101.82
F + CL equiv	-1.34	-1.60	-1.59	-1.31
New total	101.02	98.99	98.66	100.51
apfu	Serra dé Mage	Serra dé Mage	Serra dé Mage	Moore County
Р	5.844	6.016	5.996	5.963
Ca	9.711	9.898	9.937	10.052
Sr	0.000	0.000	0.000	0.000
Na	0.000	0.000	0.000	0.000
Ce	0.000	0.000	0.000	0.000
Fe	0.168	0.011	0.015	0.027
Mg	0.038	0.000	0.000	0.000
S	0.000	0.000	0.000	0.000
Υ	0.000	0.000	0.000	0.000
As	0.000	0.000	0.000	0.000
Si	0.194	0.023	0.025	0.000
F	1.664	2.038	2.032	1.640
Cl	0.000	0.000	0.000	0.000
F+cl	1.664	2.038	2.032	1.640
total cations	15.956	15.948	15.973	16.042
ОН	0.336	0.000	0.000	0.360
OH wt%	0.57	0.00	0.00	0.61
Total with OH	101.59	98.99	98.66	101.13
P-site	6.0	6.0	6.0	6.0
Ca-Site	9.7	9.9	9.9	10.1

cumulate	cumulate	cumulate	cumulate	cumulate
Moore County	Moore County	Moore County	ALH 85001	ALH 85001
41.81	41.95	41.46	41.98	41.51
56.17	54.21	55.40	55.13	55.36
< 0.08	< 0.08	< 0.08	-	-
0.29	< 0.10	< 0.10	-	-
< 0.59	< 0.59	< 0.59	-	-
< 0.16	0.58	0.60	0.24	0.22
< 0.06	< 0.06	< 0.06	-	-
< 0.06	< 0.06	< 0.06	-	-
< 0.21	< 0.21	< 0.21	-	-
< 0.9	< 0.9	< 0.9	-	-
< 0.02	0.06	0.10	< 0.02	0.04
3.03	3.46	3.07	3.74	3.51
< 0.07	< 0.07	< 0.07	0.09	0.16
101.30	100.26	100.63	101.18	100.79
-1.28	-1.46	-1.29	-1.60	-1.51
100.02	98.80	99.34	99.59	99.28
Moore County	Moore County	Moore County	ALH 85001	ALH 85001
5.941	6.013	5.930	6.003	5.963
10.101	9.835	10.028	9.977	10.065
0.000	0.000	0.000	0.000	0.000
0.093	0.000	0.000	0.000	0.000
0.000	0.000	0.000	0.000	0.000
0.000	0.074	0.077	0.010	0.009
0.000	0.000	0.000	0.000	0.000
0.000	0.000	0.000	0.000	0.000
0.000	0.000	0.000	0.000	0.000
0.000	0.000	0.000	0.000	0.000
0.000	0.011	0.016	0.000	0.006
1.608	1.853	1.640	1.998	1.884
0.000	0.000	0.000	0.027	0.045
1.608	1.853	1.640	2.025	1.928
16.135	15.932	16.051	15.990	16.044
0.392	0.147	0.360	0.000	0.072
0.66	0.25	0.60	0.00	0.12
100.68	99.05	99.94	99.59	99.39
5.9	6.0	5.9	6.0	6.0
10.1	9.8	10.0	10.0	10.1

cumulate ALH 85001	cumulate ALH 85001	cumulate ALH 85001	cumulate ALH 85001	basaltic EET 87542
41.30	42.99	41.36	41.90	40.52
55.15	54.29	55.27	54.49	53.19
-	-	-	-	-
-	-	-	-	-
-	-	-	-	-
0.22	0.17	0.16	<0.16	2.34
-	-	-	-	-
-	-	-	-	-
-	-	-	-	-
-	-	-	-	-
0.04	<0.02	<0.02	< 0.02	0.85
3.65	3.50	3.33	3.64	3.76
0.20	< 0.07	0.10	0.14	< 0.07
100.55	100.95	100.22	100.17	100.66
-1.58	-1.47	-1.42	-1.56	-1.58
98.97	99.48	98.79	98.61	99.08
ALH 85001	ALH 85001	ALH 85001	ALH 85001	EET 87542
5.960	6.097	5.962	6.030	5.901
10.073	9.745	10.084	9.925	9.804
0.000	0.000	0.000	0.000	0.000
0.000	0.000	0.000	0.000	0.000
0.000	0.000	0.000	0.000	0.000
0.009	0.007	0.007	0.000	0.101
0.000	0.000	0.000	0.000	0.000
0.000	0.000	0.000	0.000	0.000
0.000	0.000	0.000	0.000	0.000
0.000	0.000	0.000	0.000	0.000
0.006	0.000	0.000	0.000	0.146
1.968	1.854	1.793	1.957	2.045
0.058	0.000	0.028	0.040	0.000
2.026	1.854	1.821	1.997	2.045
16.049	15.850	16.053	15.955	15.952
0.000	0.146	0.179	0.003	0.000
0.00	0.25	0.30	0.003	0.00
98.97	99.72	99.09	98.61	99.08
6.0	99.72 6.1	6.0	6.0	99.08 6.0
			9.9	
10.1	9.8	10.1	9.9	9.9

basaltic	basaltic	basaltic	basaltic	basaltic
EET 87542				
41.57	39.74	42.58	41.23	40.60
54.41	53.31	55.09	53.82	54.15
-	-	-	-	-
-	-	-	-	-
-	-	-	-	-
0.17	3.26	0.45	3.12	3.11
-	-	-	-	-
-	-	-	-	-
-	-	-	-	-
-	-	-	-	-
0.26	0.61	0.28	0.13	0.07
3.73	3.47	3.42	3.77	3.56
0.10	0.11	0.11	< 0.07	0.07
100.24	100.49	101.94	102.07	101.57
-1.59	-1.49	-1.47	-1.59	-1.52
98.65	99.01	100.47	100.48	100.05
EET 87542				
5.991	5.854	6.013	5.962	5.915
9.924	9.939	9.845	9.850	9.985
0.000	0.000	0.000	0.000	0.000
0.000	0.000	0.000	0.000	0.000
0.000	0.000	0.000	0.000	0.000
0.007	0.142	0.019	0.134	0.134
0.000	0.000	0.000	0.000	0.000
0.000	0.000	0.000	0.000	0.000
0.000	0.000	0.000	0.000	0.000
0.000	0.000	0.000	0.000	0.000
0.045	0.106	0.047	0.021	0.012
2.008	1.909	1.804	2.037	1.937
0.028	0.032	0.032	0.000	0.022
2.036	1.942	1.836	2.037	1.959
15.966	16.042	15.924	15.968	16.047
0.000	0.058	0.164	0.000	0.041
0.00	0.09	0.28	0.00	0.07
98.65	99.10	100.75	100.48	100.12
6.0	6.0	6.1	6.0	5.9
9.9	10.1	9.9	9.9	10.0

basaltic	basaltic	basaltic	basaltic	basaltic
Stannern	Stannern	Stannern	Stannern	Stannern
41.92	41.52	42.53	42.67	42.92
54.39	54.98	53.57	54.11	54.01
0.08	< 0.08	-	-	-
<0.10	< 0.10	-	-	-
<0.59	< 0.59	-	-	-
0.43	0.41	0.47	0.47	0.30
<0.06	< 0.06	-	-	-
< 0.06	< 0.06	-	-	-
<0.21	<0.21	-	-	-
<0.9	<0.9	-	-	-
0.08	0.06	0.08	0.12	0.09
3.15	3.12	3.62	3.56	3.46
0.13	0.16	0.14	0.20	0.19
100.19	100.25	100.40	101.13	100.96
-1.36	-1.35	-1.55	-1.54	-1.50
98.83	98.90	98.84	99.58	99.46
Stannern	Stannern	Stannern	Stannern	Stannern
6.007	5.963	6.093	6.073	6.097
9.864	9.993	9.713	9.747	9.710
0.008	0.000	0.000	0.000	0.000
0.000	0.000	0.000	0.000	0.000
0.000	0.000	0.000	0.000	0.000
0.055	0.052	0.020	0.020	0.012
0.000	0.000	0.000	0.000	0.000
0.000	0.000	0.000	0.000	0.000
0.000	0.000	0.000	0.000	0.000
0.000	0.000	0.000	0.000	0.000
0.014	0.011	0.013	0.021	0.014
1.686	1.674	1.937	1.893	1.836
0.037	0.045	0.039	0.056	0.054
1.723	1.719	1.976	1.949	1.890
15.948	16.019	15.838	15.860	15.834
0.277	0.281	0.024	0.051	0.110
0.46	0.47	0.04	0.09	0.18
99.29	99.37	98.88	99.67	99.65
6.0	6.0	6.1	6.1	6.1
9.9	10.0	9.7	9.8	9.7

basaltic	basaltic	basaltic	basaltic	basaltic
Nuevo Laredo				
40.72	40.94	42.25	43.11	43.45
55.66	55.56	55.06	53.99	54.38
< 0.08	< 0.08	< 0.08	-	-
< 0.10	< 0.10	< 0.10	-	-
< 0.59	< 0.59	< 0.59	-	-
< 0.16	0.20	0.34	0.22	< 0.16
< 0.06	< 0.06	< 0.06	-	-
< 0.06	0.12	< 0.06	-	-
< 0.21	< 0.21	< 0.21	-	-
< 0.9	< 0.9	< 0.9	-	-
0.86	0.45	0.44	0.09	< 0.02
3.59	3.62	3.19	3.48	3.56
0.23	0.27	0.20	0.22	0.24
101.06	101.16	101.48	101.11	101.63
-1.56	-1.59	-1.39	-1.51	-1.55
99.50	99.58	100.09	99.60	100.08
Nuevo Laredo				
5.841	5.872	5.974	6.109	6.121
10.105	10.085	9.853	9.683	9.696
0.000	0.000	0.000	0.000	0.000
0.000	0.000	0.000	0.000	0.000
0.000	0.000	0.000	0.000	0.000
0.000	0.026	0.043	0.009	0.000
0.000	0.000	0.000	0.000	0.000
0.000	0.015	0.000	0.000	0.000
0.000	0.000	0.000	0.000	0.000
0.000	0.000	0.000	0.000	0.000
0.146	0.077	0.074	0.016	0.000
1.924	1.939	1.685	1.842	1.873
0.066	0.078	0.055	0.062	0.067
1.990	2.017	1.740	1.904	1.941
16.092	16.074	15.944	15.816	15.818
0.010	0.000	0.259	0.096	0.059
0.02	0.00	0.44	0.16	0.10
99.51	99.56	100.50	99.76	100.18
6.0	6.0	6.0	6.1	6.1
10.1	10.1	9.9	9.7	9.7
10.1	10.1	5.5	5.7	J. /

basaltic	basaltic	basaltic	basaltic	basaltic
Nuevo Laredo	Nuevo Laredo	Nuevo Laredo	Pasamonte	Pasamonte
42.92	42.42	42.80	40.54	40.40
54.45	54.55	54.55	54.30	54.71
-	-	-	-	-
-	-	-	-	-
-	-	-	-	-
<0.16	<0.16	0.20	1.43	2.32
-	-	-	-	-
-	-	-	-	-
-	-	-	-	-
-	-	-	-	-
0.04	0.04	0.10	1.59	0.56
3.51	3.33	3.78	3.22	2.84
0.12	0.20	0.09	0.22	0.22
101.04	100.53	101.52	101.30	101.05
-1.51	-1.45	-1.61	-1.41	-1.25
99.53	99.09	99.91	99.89	99.81
Nuevo Laredo	Nuevo Laredo	Nuevo Laredo	Pasamonte	Pasamonte
6.086	6.054	6.067	5.809	5.852
9.772	9.853	9.786	9.848	10.029
0.000	0.000	0.000	0.000	0.000
0.000	0.000	0.000	0.000	0.000
0.000	0.000	0.000	0.000	0.000
0.000	0.000	0.008	0.061	0.100
0.000	0.000	0.000	0.000	0.000
0.000	0.000	0.000	0.000	0.000
0.000	0.000	0.000	0.000	0.000
0.000	0.000	0.000	0.000	0.000
0.006	0.006	0.017	0.269	0.096
1.859	1.775	2.001	1.724	1.537
0.035	0.056	0.026	0.063	0.064
1.894	1.831	2.027	1.787	1.600
15.865	15.913	15.879	15.987	16.077
0.106	0.169	0.000	0.213	0.400
0.18	0.28	0.00	0.36	0.66
99.71	99.37	99.91	100.25	100.47
6.1	6.1	6.1	6.1	5.9
9.8	9.9	9.8	9.8	10.0

basaltic	basaltic	basaltic	basaltic	basaltic
Pasamonte	Pasamonte	Juvinas	Juvinas	Juvinas
41.49	39.06	41.27	42.95	43.67
54.58	54.81	56.20	55.47	54.85
-	-	< 0.08	-	-
-	-	< 0.10	-	-
-	-	< 0.59	-	-
1.20	2.33	0.42	0.15	< 0.16
-	-	< 0.06	-	-
-	-	< 0.06	-	-
-	-	< 0.21	-	-
-	-	< 0.9	-	-
0.47	1.54	0.62	0.04	0.14
3.04	2.94	3.16	3.08	2.80
0.33	0.28	0.13	0.11	0.07
101.11	100.96	101.80	101.80	101.53
-1.35	-1.30	-1.36	-1.32	-1.19
99.76	99.66	100.44	100.48	100.34
Pasamonte	Pasamonte	Juvinas	Juvinas	Juvinas
5.946	5.687	5.851	6.041	6.101
9.899	10.100	10.084	9.874	9.699
0.000	0.000	0.000	0.000	0.000
0.000	0.000	0.000	0.000	0.000
0.000	0.000	0.000	0.000	0.000
0.051	0.100	0.053	0.006	0.000
0.000	0.000	0.000	0.000	0.000
0.000	0.000	0.000	0.000	0.000
0.000	0.000	0.000	0.000	0.000
0.000	0.000	0.000	0.000	0.000
0.080	0.265	0.104	0.007	0.024
1.627	1.599	1.674	1.618	1.461
0.094	0.082	0.036	0.030	0.019
1.721	1.681	1.709	1.648	1.480
15.976	16.153	16.093	15.928	15.824
0.279	0.319	0.291	0.352	0.520
0.47	0.53	0.49	0.60	0.89
100.23	100.18	100.93	101.07	101.23
6.0	6.0	6.0	6.0	6.1
9.9	10.1	10.1	9.9	9.7

basaltic	basaltic	basaltic	basaltic	basaltic
Juvinas	Juvinas	GRA 98098	GRA 98098	GRA 98098
42.40	42.93	41.63	41.57	42.27
54.97	55.25	55.60	55.20	54.93
-	-	< 0.08	-	-
-	-	< 0.10	-	-
- <0.16	<0.16	<0.59 0.37	0.40	0.20
<0.16	<0.10	< 0.06	0.40	0.29
-	-	< 0.06	-	-
-	-	<0.06	-	-
-	-	<0.21 <0.9	-	-
0.02	0.09	0.33	0.20	0.12
0.92			2.89	0.12 2.65
2.88	2.71 0.08	2.48 0.75	0.88	2.65 0.86
0.10 101.27			101.14	101.12
	101.06	101.15	-1.42	
-1.24	-1.16	-1.21		-1.31
100.03	99.90	99.94	99.73	99.81
Juvinas	Juvinas	GRA 98098	GRA 98098	GRA 98098
5.964 9.785	6.048	5.934 10.030	5.958 10.012	6.018 9.897
0.000	9.850 0.000	0.000	0.000	0.000
0.000	0.000	0.000	0.000	0.000
0.000	0.000	0.000	0.000	0.000
0.000	0.000	0.015	0.017	0.012
0.000	0.000	0.000	0.000	0.000
	0.000	0.000	0.000	0.000
0.000 0.000	0.000	0.000	0.000	0.000
0.000	0.000	0.000 0.056	0.000	0.000
0.153	0.015		0.034	0.020
1.513	1.426	1.320	1.547	1.409
0.028	0.023	0.213	0.252	0.244
1.541	1.449	1.533	1.799	1.653
15.902	15.913	16.035	16.021	15.947
0.459	0.551	0.467	0.201	0.347
0.78	0.94	0.78	0.34	0.58
100.81	100.84	100.73	100.06	100.39
6.1	6.1	6.0	6.0	6.0
9.8	9.9	10.0	10.0	9.9

basaltic GRA 98098 43.00	basaltic GRA 98098 42.99	basaltic GRA 98098 42.67	basaltic GRA 98098 41.63	basaltic GRA 98098 41.41
53.97	53.72	53.73	54.31	54.88
-	-	-	-	-
-	-	-	-	-
-	-	-	-	-
0.21	0.35	0.32	1.39	0.57
-	-	-	-	-
-	-	-	-	-
-	-	-	-	-
-	-	-	-	-
0.14	0.17	0.20	0.22	0.40
3.21	2.89	3.10	2.91	2.43
0.77	0.90 101.02	0.79	0.77	0.83
101.30 -1.53		100.82	101.23 -1.40	100.51
-1.53 99.78	-1.42 99.60	-1.48 99.33	-1.40 99.83	-1.21 99.30
99.76 GRA 98098	GRA 98098	99.33 GRA 98098	99.63 GRA 98098	GRA 98098
6.100	6.105	6.086	5.983	5.944
9.690	9.656	9.699	9.878	9.970
0.000	0.000	0.000	0.000	0.000
0.000	0.000	0.000	0.000	0.000
0.000	0.000	0.000	0.000	0.000
0.009	0.015	0.014	0.059	0.024
0.000	0.000	0.000	0.000	0.000
0.000	0.000	0.000	0.000	0.000
0.000	0.000	0.000	0.000	0.000
0.000	0.000	0.000	0.000	0.000
0.024	0.029	0.033	0.038	0.067
1.701	1.533	1.652	1.562	1.303
0.219	0.255	0.227	0.221	0.237
1.920	1.788	1.878	1.783	1.540
15.822	15.805	15.831	15.958	16.005
0.080	0.212	0.122	0.217	0.460
0.14	0.36	0.20	0.36	0.77
99.91	99.96	99.54	100.20	100.07
6.1	6.1	6.1	6.0	6.0
9.7	9.7	9.7	9.9	10.0

basaltic GRA 98098 41.62	basaltic GRA 98098 41.91	basaltic GRA 98098 41.91	basaltic EET 87542 40.52	basaltic EET 87542 41.57
55.00	53.54	53.54	53.19	54.41
-	-	-	-	-
-	-	-	-	-
-	-	-	-	-
0.28	1.46	1.46	2.34	0.17
-	-	-	-	-
-	-	-	-	-
-	-	-	-	-
-	-	-	-	-
0.31	0.19	0.19	0.85	0.26
3.17	3.24	3.24	3.76	3.73
1.04	0.92	0.92	< 0.07	0.10
101.42	101.25	101.25	100.66	100.24
-1.57	-1.57	-1.57	-1.58	-1.59
99.85	99.68	99.68	99.08	98.65
GRA 98098	GRA 98098	GRA 98098	EET 87542	EET 87542
5.962	6.034	6.034	5.901	5.991
9.972	9.757	9.757	9.804	9.924
0.000	0.000	0.000	0.000	0.000
0.000	0.000	0.000	0.000	0.000
0.000	0.000	0.000	0.000	0.000
0.012	0.062	0.062	0.101	0.007
0.000	0.000	0.000	0.000	0.000
0.000	0.000	0.000	0.000	0.000
0.000	0.000	0.000	0.000	0.000
0.000	0.000	0.000	0.000	0.000
0.052	0.032	0.032	0.146	0.045
1.696	1.743	1.743	2.045	2.008
0.298	0.264	0.264	0.000	0.028
1.994	2.007	2.007	2.045	2.036
15.998	15.885	15.885	15.952	15.966
0.006	0.000	0.000	0.000	0.000
0.01	0.00	0.00	0.00	0.00
99.86	99.68	99.68	99.08	98.65
6.0	6.1	6.1	6.0	6.0
10.0	9.8	9.8	9.9	9.9

basaltic EET 87542 39.74 53.31	basaltic EET 87542 42.58 55.09	basaltic EET 87542 41.23 53.82	basaltic EET 87542 40.60 54.15	basaltic LEW 88009 41.26 55.36
33.31	33.09	33.62	34.13	33.30
_	_	_	-	_
_		_	_	_
3.26	0.45	3.12	3.11	0.35
5.20	-	5.12	J.11 -	0.55
_	_	_	_	_
_	_	_	_	_
_	-	_	_	_
0.61	0.28	0.13	0.07	0.23
3.47	3.42	3.77	3.56	3.58
0.11	0.11	< 0.07	0.07	0.08
100.49	101.94	102.07	101.57	100.86
-1.49	-1.47	-1.59	-1.52	-1.52
99.01	100.47	100.48	100.05	99.34
EET 87542	EET 87542	EET 87542	EET 87542	LEW 88009
5.854	6.013	5.962	5.915	5.931
9.939	9.845	9.850	9.985	10.071
0.000	0.000	0.000	0.000	0.000
0.000	0.000	0.000	0.000	0.000
0.000	0.000	0.000	0.000	0.000
0.142	0.019	0.134	0.134	0.015
0.000	0.000	0.000	0.000	0.000
0.000	0.000	0.000	0.000	0.000
0.000	0.000	0.000	0.000	0.000
0.000	0.000	0.000	0.000	0.000
0.106	0.047	0.021	0.012	0.039
1.909	1.804	2.037	1.937	1.922
0.032	0.032	0.000	0.022	0.022
1.942	1.836	2.037	1.959	1.944
16.042	15.924	15.968	16.047	16.057
0.058	0.164	0.000	0.041	0.056
0.09	0.28	0.00	0.07	0.09
99.10	100.75	100.48	100.12	99.43
6.0	6.1	6.0	5.9	6.0
10.1	9.9	9.9	10.0	10.1

basaltic LEW 88009 42.51	basaltic LEW 88009 39.73	basaltic LEW 88010 41.90	basaltic LEW 88010 42.02	basaltic LEW 88010 42.70
54.55	54.19	53.98	54.56	54.48
-	-	-	-	-
-	-	-	-	-
-	-	-	-	-
0.25	0.60	0.48	0.65	0.66
-	-	-	-	-
-	-	-	-	-
-	-	-	-	-
-	-	-	-	- 0.24
0.09	2.34	0.21	0.11	0.24
3.46	3.44	3.50	3.05	3.47
0.07 100.93	0.12	0.26	0.15	0.20
-1.47	100.42 -1.48	100.32 -1.53	100.54 -1.32	101.75 -1.51
-1.47 99.46	-1.46 98.95	-1.53 98.79	-1.32 99.22	100.25
99.46 LEW 88009	98.95 LEW 88009	98.79 LEW 88010	199.22 LEW 88010	LEW 88010
6.051	5.718	6.028	6.015	6.046
9.827	9.871	9.829	9.884	9.763
0.000	0.000	0.000	0.000	0.000
0.000	0.000	0.000	0.000	0.000
0.000	0.000	0.000	0.000	0.000
0.011	0.026	0.021	0.028	0.028
0.000	0.000	0.000	0.000	0.000
0.000	0.000	0.000	0.000	0.000
0.000	0.000	0.000	0.000	0.000
0.000	0.000	0.000	0.000	0.000
0.015	0.398	0.035	0.018	0.041
1.840	1.849	1.881	1.631	1.835
0.021	0.036	0.074	0.043	0.057
1.860	1.885	1.955	1.674	1.892
15.903	16.012	15.913	15.945	15.877
0.140	0.115	0.045	0.326	0.108
0.24	0.19	0.08	0.55	0.18
99.69	99.14	98.87	99.77	100.43
6.1	6.1	6.1	6.0	6.1
9.8	9.9	9.8	9.9	9.8

basaltic LEW 88010	basaltic LEW 88010	basaltic LEW 88010	basaltic LEW 88010	basaltic EET 90020
41.00	41.74	41.75	41.07	42.52
54.47	54.58	55.10	53.76	54.46
-	-	-	-	<0.08
-	-	-	-	< 0.10
-	-	-	-	< 0.59
0.88	0.35	0.40	1.32	< 0.16
-	-	-	-	< 0.06
-	-	-	-	0.07
-	-	-	-	< 0.21
-	-	-	-	< 0.9
0.32	0.11	0.12	0.49	0.15
3.68	3.56	3.12	3.53	3.46
0.19	0.23	0.20	0.23	< 0.07
100.54	100.57	100.68	100.41	100.67
-1.59	-1.55	-1.36	-1.54	-1.46
98.95	99.02	99.33	98.87	99.21
LEW 88010	LEW 88010	LEW 88010	LEW 88010	EET 90020
5.939	6.003	5.979	5.954	6.047
9.986	9.934	9.987	9.863	9.802
0.000	0.000	0.000	0.000	0.000
0.000	0.000	0.000	0.000	0.000
0.000	0.000	0.000	0.000	0.000
0.038	0.015	0.017	0.057	0.000
0.000	0.000	0.000	0.000	0.000
0.000	0.000	0.000	0.000	0.009
0.000	0.000	0.000	0.000	0.000
0.000	0.000	0.000	0.000	0.000
0.055	0.019	0.020	0.084	0.026
1.991	1.912	1.669	1.911	1.838
0.055	0.065	0.056	0.068	0.000
2.046	1.977	1.725	1.979	1.838
16.018	15.970	16.003	15.957	15.885
0.000	0.023	0.275	0.021	0.162
0.00	0.04	0.46	0.03	0.27
98.95	99.05	99.79	98.90	99.48
6.0	6.0	6.0	6.0	6.1
10.0	9.9	10.0	9.9	9.8

| basaltic
EET 90020 |
|-----------------------|-----------------------|-----------------------|-----------------------|-----------------------|
| 42.04 | 42.38 | 42.58 | 42.84 | 42.81 |
55.51	54.46	54.92	54.45	54.58
_	_	_	_	-
_	_	_	_	-
0.15	0.00	0.19	0.00	0.00
-	-	-	-	_
-	-	-	-	-
-	-	-	-	-
-	-	-	-	-
0.06	< 0.02	0.06	0.07	0.00
3.79	3.30	3.38	3.44	3.40
< 0.07	< 0.07	< 0.07	< 0.07	< 0.07
101.55	100.35	101.14	100.80	100.79
-1.60	-1.44	-1.42	-1.45	-1.43
99.95	98.92	99.72	99.35	99.36
EET 90020				
5.987	6.059	6.042	6.079	6.077
10.005	9.853	9.862	9.779	9.806
0.000	0.000	0.000	0.000	0.000
0.000	0.000	0.000	0.000	0.000
0.000	0.000	0.000	0.000	0.000
0.006	0.000	0.008	0.000	0.000
0.000	0.000	0.000	0.000	0.000
0.000	0.000	0.000	0.000	0.000
0.000	0.000	0.000	0.000	0.000
0.000	0.000	0.000	0.000	0.000
0.010	0.000	0.011	0.012	0.000
2.016	1.762	1.791	1.823	1.803
0.000	0.061	0.000	0.000	0.000
2.016	1.823	1.791	1.823	1.803
16.007	15.912	15.923	15.870	15.884
0.000	0.177	0.209	0.177	0.197
0.00	0.30	0.35	0.30	0.33
99.95	99.21	100.07	99.65	99.69
6.0	6.1	6.1	6.1	6.1
10.0	9.9	9.9	9.8	9.8

basaltic EET 90020 41.76 54.85	basaltic EET 90020 42.89 53.69	basaltic EET 90020 42.88 54.61	basaltic EET 90020 43.30 54.56	basaltic EET 90020 42.43 55.01
-	-	-	-	-
_	_	_	_	_
_	_	_	_	_
0.00	0.19	0.19	0.18	0.19
-	-	-	-	<u>-</u>
-	-	-	_	_
-	-	-	_	_
-	-	-	-	-
0.05	0.09	0.09	0.09	0.04
3.19	3.62	3.13	3.42	3.51
< 0.07	< 0.07	< 0.07	< 0.07	< 0.07
99.85	100.48	100.90	101.55	101.18
-1.34	-1.52	-1.32	-1.44	-1.48
98.51	98.96	99.58	100.11	99.70
EET 90020				
6.002	6.111	6.070	6.095	6.031
9.978	9.682	9.783	9.720	9.897
0.000	0.000	0.000	0.000	0.000
0.000	0.000	0.000	0.000	0.000
0.000	0.000	0.000	0.000	0.000
0.000	0.008	0.008	0.007	0.008
0.000	0.000	0.000	0.000	0.000
0.000	0.000	0.000	0.000	0.000
0.000	0.000	0.000	0.000	0.000
0.000	0.000	0.000	0.000	0.000
0.008	0.014	0.016	0.015	0.006
1.713	1.927	1.655	1.798	1.864
0.000	0.000	0.000	0.000	0.000
1.713	1.927	1.655	1.798	1.864
15.988	15.815	15.876	15.838	15.943
0.287	0.073	0.345	0.202	0.136
0.48	0.12	0.58	0.34	0.23
98.99	99.08	100.17	100.45	99.93
6.0	6.1	6.1	6.1	6.0
10.0	9.7	9.8	9.7	9.9

basaltic EET 90020 42.17	basaltic EET 90020 42.62	basaltic EET 90020 42.70	basaltic EET 90020 42.38	basaltic EET 90020 42.14
54.86	55.77	54.32	54.88	54.31
-	-	-	-	-
-	-	-	-	-
-	-	-	-	-
0.00	0.00	0.00	0.19	0.30
-	-	-	-	-
-	-	-	-	-
-	-	-	-	-
-	-	-	-	-
0.05	0.07	0.09	0.06	0.06
3.23	3.42	3.55	3.57	3.55
< 0.07	< 0.07	< 0.07	< 0.07	<0.07
100.31	101.88	100.66	101.07	100.36
-1.36	-1.44	-1.49	-1.50	-1.49
98.95	100.44	99.17	99.57	98.86
EET 90020				
6.025	6.010	6.075	6.033	6.042
9.920	9.952	9.781	9.887	9.856
0.000	0.000	0.000	0.000	0.000
0.000	0.000	0.000	0.000	0.000
0.000	0.000	0.000	0.000	0.000
0.000	0.000	0.000	0.008	0.013
0.000	0.000	0.000	0.000	0.000
0.000	0.000	0.000	0.000	0.000
0.000	0.000	0.000	0.000	0.000
0.000	0.000	0.000	0.000	0.000
0.009	0.012	0.015	0.009	0.009
1.724	1.801	1.887	1.898	1.901
0.000	0.000	0.000	0.000	0.000
1.724	1.801	1.887	1.898	1.901
15.954	15.974	15.872	15.937	15.921
0.276	0.199	0.113	0.102	0.099
0.46	0.34	0.19	0.17	0.16
99.42	100.78	99.36	99.74	99.03
6.0	6.0	6.1	6.0	6.1
9.9	10.0	9.8	9.9	9.9
5.5	10.0	5.0	5.5	J.J

basaltic EET 90020 42.46 55.30	basaltic EET 90020 42.31 54.29	basaltic EET 90020 42.76 54.57	basaltic EET 90020 42.96 54.40	basaltic EET 90020 43.46 54.14
-	-	-	-	-
_	_	_	_	_
_	_	_	_	_
0.14	0.22	0.36	0.25	0.00
-	-	-	-	_
-	-	-	-	-
-	-	-	-	_
-	-	-	-	-
0.06	0.08	0.11	0.04	0.20
3.56	3.39	3.09	3.54	3.68
< 0.07	< 0.07	< 0.07	< 0.07	< 0.07
101.52	100.29	100.96	101.18	101.48
-1.50	-1.43	-1.32	-1.49	-1.55
100.02	98.86	99.64	99.69	99.93
EET 90020				
6.019	6.052	6.061	6.087	6.116
9.922	9.829	9.789	9.755	9.643
0.000	0.000	0.000	0.000	0.000
0.000	0.000	0.000	0.000	0.000
0.000	0.000	0.000	0.000	0.000
0.006	0.009	0.015	0.010	0.000
0.000	0.000	0.000	0.000	0.000
0.000	0.000	0.000	0.000	0.000
0.000	0.000	0.000	0.000	0.000
0.000	0.000	0.000	0.000	0.000
0.011	0.013	0.018	0.006	0.033
1.885	1.811	1.636	1.874	1.935
0.000	0.000	0.020	0.000	0.000
1.885	1.811	1.656	1.874	1.935
15.957	15.904	15.883	15.858	15.792
0.115	0.189	0.344	0.126	0.065
0.19	0.32	0.58	0.21	0.11
100.22	99.18	100.22	99.91	100.04
6.0	6.1	6.1	6.1	6.1
9.9	9.8	9.8	9.8	9.6

basaltic EET 90020 42.13 54.90	basaltic EET 90020 41.97 54.81	basaltic EET 90020 43.08 54.10	basaltic EET 90020 43.22 54.22	basaltic EET 90020 43.25 54.67
-	_	-	_	-
-	-	-	_	-
-	-	-	_	-
0.16	0.28	0.00	0.00	0.34
-	-	-	_	-
-	-	-	_	-
-	-	-	-	-
-	-	-	-	-
0.04	0.24	0.06	0.07	0.03
3.48	3.37	3.29	3.31	3.51
< 0.07	< 0.07	< 0.07	< 0.07	< 0.07
100.71	100.74	100.53	100.82	101.86
-1.47	-1.43	-1.39	-1.39	-1.49
99.25	99.30	99.14	99.42	100.37
EET 90020				
6.019	5.996	6.109	6.110	6.090
9.927	9.910	9.709	9.701	9.744
0.000	0.000	0.000	0.000	0.000
0.000	0.000	0.000	0.000	0.000
0.000	0.000	0.000	0.000	0.000
0.007	0.012	0.000	0.000	0.014
0.000	0.000	0.000	0.000	0.000
0.000	0.000	0.000	0.000	0.000
0.000	0.000	0.000	0.000	0.000
0.000	0.000	0.000	0.000	0.000
0.007	0.041	0.010	0.011	0.004
1.857	1.798	1.743	1.748	1.846
0.000	0.018	0.000	0.000	0.018
1.857	1.817	1.743	1.748	1.864
15.960	15.959	15.827	15.823	15.853
0.143	0.183	0.257	0.252	0.136
0.24	0.31	0.43	0.43	0.23
99.49	99.61	99.58	99.85	100.60
6.0	6.0	6.1	6.1	6.1
9.9	9.9	9.7	9.7	9.8

basaltic BTN 00300 42.88	basaltic BTN 00300 41.55	basaltic BTN 00300 41.59	basaltic BTN 00300 41.79	basaltic BTN 00300 41.53
54.22	55.15	54.48	54.80	54.97
-	-	-	-	-
-	-	-	-	-
-	-	-	-	-
0.27	0.60	0.24	0.26	0.18
-	-	-	-	-
-	-	-	-	-
-	-	-	-	-
- 0.17	- 0.40	- 0.12	- 0.12	-
0.17	0.40	0.13	0.12	0.08
3.70 <0.07	3.28 <0.07	3.47 <0.07	3.62 <0.07	3.77 <0.07
101.24	100.98	99.91	100.59	100.53
-1.56	-1.38	-1.46	-1.52	-1.59
99.68	99.60	98.45	99.07	98.94
BTN 00300				
6.079	5.940	5.999	5.996	5.978
9.729	9.978	9.945	9.951	10.015
0.000	0.000	0.000	0.000	0.000
0.000	0.000	0.000	0.000	0.000
0.000	0.000	0.000	0.000	0.000
0.011	0.025	0.010	0.011	0.008
0.000	0.000	0.000	0.000	0.000
0.000	0.000	0.000	0.000	0.000
0.000	0.000	0.000	0.000	0.000
0.000	0.000	0.000	0.000	0.000
0.028	0.068	0.022	0.021	0.014
1.959	1.751	1.869	1.940	2.027
0.000	0.000	0.000	0.000	0.000
1.959	1.751	1.869	1.940	2.027
15.847	16.010	15.975	15.979	16.015
0.041	0.249	0.131	0.060	0.000
0.07	0.42	0.22	0.10	0.00
99.75	100.01	98.66	99.17	98.94
6.1	6.0	6.0	6.0	6.0
9.7	10.0	10.0	10.0	10.0

BTN 00300 WHOI durango WHOI durango WHOI durango 41.38 40.63 41.15 41.29 42.15 55.11 55.64 55.22 55.53 53.60 - 0.07 0.07 0.07 0.07 - 0.23 0.23 0.23 0.23 - 0.50 0.50 0.50 0.50 0.44 0.06 0.06 0.06 0.06 0.06 - 0.01 0.01 0.01 0.01 0.01 - 0.036 0.30 0.29 0.20 - 0.00 0.00 0.00 0.00 0.00 - 0.00 0.00 0.00 0.00 0.00 0.00 0.04 0.34 0.34 0.34 0.34 0.34 0.34 0.34 0.34 0.34 0.34 0.34 0.34 0.35 0.03 0.05 0.05 0.05 0.05 0.05 0.05 0.05 0.05 0.05	basaltic	Standard	Standard	Standard	Standard
41.38 40.63 41.15 41.29 42.15 55.11 55.64 55.22 55.53 53.60 - 0.07 0.07 0.07 0.07 - 0.50 0.50 0.50 0.50 0.44 0.06 0.06 0.06 0.06 - 0.01 0.01 0.01 0.01 - 0.36 0.30 0.29 0.20 - 0.00 0.00 0.00 0.00 - 0.00 0.00 0.00 0.00 - 0.00 0.00 0.00 0.00 - 0.00 0.00 0.00 0.00 0.04 0.34 0.34 0.34 0.34 3.66 2.74 3.13 3.05 3.03 <0.07	BTN 00300	WHOI durango	WHOI durango	WHOI durango	WHOI durango
- 0.07 0.07 0.07 0.07 - 0.23 0.23 0.23 0.23 - 0.50 0.50 0.50 0.50 0.44 0.06 0.06 0.06 0.06 - 0.01 0.01 0.01 0.01 - 0.36 0.30 0.29 0.20 - 0.00 0.00 0.00 0.00 - 0.00 0.00 0.00 0.00 - 0.00 0.00 0.00 0.00 - 0.00 0.00 0.00 0.00 0.04 0.34 0.34 0.34 0.34 0.34 3.66 2.74 3.13 3.05 3.03 100.63 100.90 101.34 101.72 100.55 -1.54 -1.22 -1.39 -1.36 99.19 BTN 00300 WHOI durango WHOI durango WHOI durango WHOI durango MHOI durango 0.00 0.00 <td>41.38</td> <td></td> <td></td> <td>_</td> <td>_</td>	41.38			_	_
- 0.23 0.23 0.23 0.23 - 0.50 0.50 0.50 0.50 0.44 0.06 0.06 0.06 0.06 - 0.01 0.01 0.01 0.01 - 0.00 0.00 0.00 0.00 - 0.00 0.00 0.00 0.00 0.04 0.34 0.34 0.34 0.34 3.66 2.74 3.13 3.05 3.03 <0.07	55.11	55.64	55.22	55.53	53.60
- 0.50 0.50 0.50 0.50 0.44 0.06 0.06 0.06 0.06 - 0.01 0.01 0.01 0.01 - 0.36 0.30 0.29 0.20 - 0.00 0.00 0.00 0.00 - 0.00 0.00 0.00 0.00 0.04 0.34 0.34 0.34 0.34 3.66 2.74 3.13 3.05 3.03 <0.07	-				
- 0.50 0.50 0.50 0.50 0.44 0.06 0.06 0.06 0.06 - 0.01 0.01 0.01 0.01 - 0.36 0.30 0.29 0.20 - 0.00 0.00 0.00 0.00 - 0.00 0.00 0.00 0.00 0.04 0.34 0.34 0.34 0.34 3.66 2.74 3.13 3.05 3.03 <0.07	-			0.23	
0.44 0.06 0.06 0.06 0.06 - 0.01 0.01 0.01 0.01 - 0.36 0.30 0.29 0.20 - 0.00 0.00 0.00 0.00 - 0.00 0.00 0.00 0.00 0.04 0.34 0.34 0.34 0.34 3.66 2.74 3.13 3.05 3.03 0.07 0.32 0.33 0.35 0.35 100.63 100.90 101.34 101.72 100.55 -1.54 -1.22 -1.39 -1.36 -1.36 99.09 99.67 99.95 100.35 99.19 BTN 00300 WHOI durango WHOI durango WHOI durango WHOI durango 5.963 5.821 5.875 5.871 6.012 10.050 10.089 9.978 9.994 9.675 0.000 0.007 0.007 0.007 0.007 0.000 0.	-	0.50		0.50	0.50
- 0.01 0.01 0.01 0.01 - 0.36 0.30 0.29 0.20 - 0.00 0.00 0.00 0.00 - 0.00 0.00 0.00 0.00 0.04 0.34 0.34 0.34 0.34 3.66 2.74 3.13 3.05 3.03 <0.07	0.44				
- 0.36 0.30 0.29 0.20 - 0.00 0.00 0.00 0.00 - 0.00 0.00 0.00 0.00 0.04 0.34 0.34 0.34 0.34 3.66 2.74 3.13 3.05 3.03 <0.07	-				
- 0.00 0.00 0.00 0.00 0.04 0.34 0.34 0.34 0.34 3.66 2.74 3.13 3.05 3.03 <0.07	-				
- 0.00 0.00 0.00 0.00 0.04 0.34 0.34 0.34 0.34 3.66 2.74 3.13 3.05 3.03 <0.07	-				
0.04 0.34 0.34 0.34 3.66 2.74 3.13 3.05 3.03 <0.07	-				
<0.07	0.04	0.34		0.34	0.34
<0.07					
100.63 100.90 101.34 101.72 100.55 -1.54 -1.22 -1.39 -1.36 -1.36 99.09 99.67 99.95 100.35 99.19 BTN 00300 WHOI durango WHOI durango WHOI durango WHOI durango 5.963 5.821 5.875 5.871 6.012 10.050 10.089 9.978 9.994 9.675 0.000 0.007 0.007 0.007 0.007 0.000 0.075 0.075 0.075 0.075 0.000 0.031 0.031 0.031 0.031 0.019 0.008 0.008 0.008 0.008 0.000 0.003 0.003 0.003 0.003 0.000 0.046 0.038 0.036 0.026 0.000 0.000 0.000 0.000 0.000 0.000 0.000 0.000 0.000 0.000 0.008 0.058 0.057 0.057 0.057					
-1.54-1.22-1.39-1.36-1.3699.0999.6799.95100.3599.19BTN 00300WHOI durangoWHOI durangoWHOI durango5.9635.8215.8755.8716.01210.05010.0899.9789.9949.6750.0000.0070.0070.0070.0070.0000.0750.0750.0750.0750.0000.0310.0310.0310.0310.0190.0080.0080.0080.0080.0000.0030.0030.0030.0030.0000.0460.0380.0360.0260.0000.0000.0000.0000.0000.0000.0000.0000.0000.0000.0080.0580.0570.0570.0571.9701.4661.6691.6201.6140.0000.0910.0940.0990.1011.9701.5561.7631.7191.71516.03916.13716.07216.08115.8930.0300.4440.2370.2810.2850.050.740.400.470.4899.14100.41100.34100.8399.676.05.96.06.06.06.1					
99.09 99.67 99.95 100.35 99.19 BTN 00300 WHOI durango WHOI durango WHOI durango 5.963 5.821 5.875 5.871 6.012 10.050 10.089 9.978 9.994 9.675 0.000 0.007 0.007 0.007 0.007 0.000 0.075 0.075 0.075 0.075 0.000 0.031 0.031 0.031 0.031 0.031 0.019 0.008 0.008 0.008 0.008 0.008 0.000 0.003 0.003 0.003 0.003 0.003 0.000 0.0046 0.038 0.036 0.026 0.000 0.000 0.000 0.000 0.000 0.000 0.000 0.000 0.000 0.000 0.008 0.058 0.057 0.057 0.057 1.970 1.466 1.669 1.620 1.614 0.000 0.091 0.094 0.0	-1.54				
BTN 00300 WHOI durango WHOI durango WHOI durango 5.963 5.821 5.875 5.871 6.012 10.050 10.089 9.978 9.994 9.675 0.000 0.007 0.007 0.007 0.007 0.000 0.075 0.075 0.075 0.075 0.000 0.031 0.031 0.031 0.031 0.019 0.008 0.008 0.008 0.008 0.000 0.003 0.003 0.003 0.003 0.000 0.046 0.038 0.036 0.026 0.000 0.000 0.000 0.000 0.000 0.000 0.000 0.000 0.000 0.000 0.008 0.058 0.057 0.057 0.057 1.970 1.466 1.669 1.620 1.614 0.000 0.091 0.094 0.099 0.101 1.970 1.556 1.763 1.719 1.715 16.039 <td></td> <td></td> <td></td> <td></td> <td></td>					
5.963 5.821 5.875 5.871 6.012 10.050 10.089 9.978 9.994 9.675 0.000 0.007 0.007 0.007 0.007 0.000 0.075 0.075 0.075 0.075 0.000 0.031 0.031 0.031 0.031 0.019 0.008 0.008 0.008 0.008 0.000 0.003 0.003 0.003 0.003 0.000 0.046 0.038 0.036 0.026 0.000 0.000 0.000 0.000 0.000 0.000 0.000 0.000 0.000 0.000 0.008 0.058 0.057 0.057 0.057 1.970 1.466 1.669 1.620 1.614 0.000 0.091 0.094 0.099 0.101 1.970 1.556 1.763 1.719 1.715 16.039 16.137 16.072 16.081 15.893 0.05 </td <td></td> <td></td> <td></td> <td>WHOI durango</td> <td></td>				WHOI durango	
10.050 10.089 9.978 9.994 9.675 0.000 0.007 0.007 0.007 0.007 0.000 0.075 0.075 0.075 0.075 0.000 0.031 0.031 0.031 0.031 0.019 0.008 0.008 0.008 0.008 0.000 0.003 0.003 0.003 0.003 0.000 0.046 0.038 0.036 0.026 0.000 0.000 0.000 0.000 0.000 0.000 0.000 0.000 0.000 0.000 0.008 0.058 0.057 0.057 0.057 1.970 1.466 1.669 1.620 1.614 0.000 0.091 0.094 0.099 0.101 1.970 1.556 1.763 1.719 1.715 16.039 16.137 16.072 16.081 15.893 0.05 0.74 0.40 0.47 0.48 99.14 100.41 100.34 100.83 99.67 6.0 5.9 <td></td> <td></td> <td></td> <td>_</td> <td></td>				_	
0.000 0.007 0.007 0.007 0.007 0.000 0.075 0.075 0.075 0.075 0.000 0.031 0.031 0.031 0.031 0.019 0.008 0.008 0.008 0.008 0.000 0.003 0.003 0.003 0.003 0.000 0.046 0.038 0.036 0.026 0.000 0.000 0.000 0.000 0.000 0.000 0.000 0.000 0.000 0.000 0.008 0.058 0.057 0.057 0.057 1.970 1.466 1.669 1.620 1.614 0.000 0.091 0.094 0.099 0.101 1.970 1.556 1.763 1.719 1.715 16.039 16.137 16.072 16.081 15.893 0.05 0.74 0.40 0.47 0.48 99.14 100.41 100.34 100.83 99.67 6.0	10.050	10.089		9.994	
0.000 0.031 0.031 0.031 0.031 0.019 0.008 0.008 0.008 0.008 0.000 0.003 0.003 0.003 0.003 0.000 0.046 0.038 0.036 0.026 0.000 0.000 0.000 0.000 0.000 0.000 0.000 0.000 0.000 0.000 0.008 0.058 0.057 0.057 0.057 1.970 1.466 1.669 1.620 1.614 0.000 0.091 0.094 0.099 0.101 1.970 1.556 1.763 1.719 1.715 16.039 16.137 16.072 16.081 15.893 0.030 0.444 0.237 0.281 0.285 0.05 0.74 0.40 0.47 0.48 99.14 100.41 100.34 100.83 99.67 6.0 5.9 6.0 6.0 6.1	0.000	0.007	0.007	0.007	0.007
0.019 0.008 0.008 0.008 0.008 0.000 0.003 0.003 0.003 0.003 0.000 0.046 0.038 0.036 0.026 0.000 0.000 0.000 0.000 0.000 0.000 0.000 0.000 0.000 0.000 0.008 0.058 0.057 0.057 0.057 1.970 1.466 1.669 1.620 1.614 0.000 0.091 0.094 0.099 0.101 1.970 1.556 1.763 1.719 1.715 16.039 16.137 16.072 16.081 15.893 0.030 0.444 0.237 0.281 0.285 0.05 0.74 0.40 0.47 0.48 99.14 100.41 100.34 100.83 99.67 6.0 5.9 6.0 6.0 6.1	0.000	0.075	0.075	0.075	0.075
0.000 0.003 0.003 0.003 0.003 0.000 0.046 0.038 0.036 0.026 0.000 0.000 0.000 0.000 0.000 0.000 0.000 0.000 0.000 0.000 0.008 0.058 0.057 0.057 0.057 1.970 1.466 1.669 1.620 1.614 0.000 0.091 0.094 0.099 0.101 1.970 1.556 1.763 1.719 1.715 16.039 16.137 16.072 16.081 15.893 0.030 0.444 0.237 0.281 0.285 0.05 0.74 0.40 0.47 0.48 99.14 100.41 100.34 100.83 99.67 6.0 5.9 6.0 6.0 6.1	0.000	0.031	0.031	0.031	0.031
0.000 0.003 0.003 0.003 0.003 0.000 0.046 0.038 0.036 0.026 0.000 0.000 0.000 0.000 0.000 0.000 0.000 0.000 0.000 0.000 0.008 0.058 0.057 0.057 0.057 1.970 1.466 1.669 1.620 1.614 0.000 0.091 0.094 0.099 0.101 1.970 1.556 1.763 1.719 1.715 16.039 16.137 16.072 16.081 15.893 0.030 0.444 0.237 0.281 0.285 0.05 0.74 0.40 0.47 0.48 99.14 100.41 100.34 100.83 99.67 6.0 5.9 6.0 6.0 6.1			0.008	0.008	
0.000 0.000 0.000 0.000 0.000 0.000 0.000 0.000 0.000 0.000 0.008 0.058 0.057 0.057 0.057 1.970 1.466 1.669 1.620 1.614 0.000 0.091 0.094 0.099 0.101 1.970 1.556 1.763 1.719 1.715 16.039 16.137 16.072 16.081 15.893 0.030 0.444 0.237 0.281 0.285 0.05 0.74 0.40 0.47 0.48 99.14 100.41 100.34 100.83 99.67 6.0 5.9 6.0 6.0 6.1	0.000	0.003		0.003	
0.000 0.000 0.000 0.000 0.000 0.008 0.058 0.057 0.057 0.057 1.970 1.466 1.669 1.620 1.614 0.000 0.091 0.094 0.099 0.101 1.970 1.556 1.763 1.719 1.715 16.039 16.137 16.072 16.081 15.893 0.030 0.444 0.237 0.281 0.285 0.05 0.74 0.40 0.47 0.48 99.14 100.41 100.34 100.83 99.67 6.0 5.9 6.0 6.0 6.1	0.000	0.046	0.038	0.036	0.026
0.008 0.058 0.057 0.057 0.057 1.970 1.466 1.669 1.620 1.614 0.000 0.091 0.094 0.099 0.101 1.970 1.556 1.763 1.719 1.715 16.039 16.137 16.072 16.081 15.893 0.030 0.444 0.237 0.281 0.285 0.05 0.74 0.40 0.47 0.48 99.14 100.41 100.34 100.83 99.67 6.0 5.9 6.0 6.0 6.1	0.000	0.000	0.000	0.000	0.000
1.970 1.466 1.669 1.620 1.614 0.000 0.091 0.094 0.099 0.101 1.970 1.556 1.763 1.719 1.715 16.039 16.137 16.072 16.081 15.893 0.030 0.444 0.237 0.281 0.285 0.05 0.74 0.40 0.47 0.48 99.14 100.41 100.34 100.83 99.67 6.0 5.9 6.0 6.0 6.1	0.000	0.000	0.000	0.000	0.000
0.000 0.091 0.094 0.099 0.101 1.970 1.556 1.763 1.719 1.715 16.039 16.137 16.072 16.081 15.893 0.030 0.444 0.237 0.281 0.285 0.05 0.74 0.40 0.47 0.48 99.14 100.41 100.34 100.83 99.67 6.0 5.9 6.0 6.0 6.1	0.008	0.058	0.057	0.057	0.057
1.970 1.556 1.763 1.719 1.715 16.039 16.137 16.072 16.081 15.893 0.030 0.444 0.237 0.281 0.285 0.05 0.74 0.40 0.47 0.48 99.14 100.41 100.34 100.83 99.67 6.0 5.9 6.0 6.0 6.1	1.970	1.466	1.669	1.620	1.614
1.970 1.556 1.763 1.719 1.715 16.039 16.137 16.072 16.081 15.893 0.030 0.444 0.237 0.281 0.285 0.05 0.74 0.40 0.47 0.48 99.14 100.41 100.34 100.83 99.67 6.0 5.9 6.0 6.0 6.1	0.000	0.091	0.094	0.099	0.101
0.030 0.444 0.237 0.281 0.285 0.05 0.74 0.40 0.47 0.48 99.14 100.41 100.34 100.83 99.67 6.0 5.9 6.0 6.0 6.1	1.970	1.556	1.763	1.719	
0.05 0.74 0.40 0.47 0.48 99.14 100.41 100.34 100.83 99.67 6.0 5.9 6.0 6.0 6.1	16.039	16.137	16.072	16.081	15.893
0.05 0.74 0.40 0.47 0.48 99.14 100.41 100.34 100.83 99.67 6.0 5.9 6.0 6.0 6.1					
99.14 100.41 100.34 100.83 99.67 6.0 5.9 6.0 6.0 6.1	0.030	0.444	0.237	0.281	0.285
6.0 5.9 6.0 6.0 6.1	0.05	0.74	0.40	0.47	0.48
	99.14	100.41	100.34	100.83	99.67
10.1 10.1 10.0 10.0 9.7	6.0	5.9	6.0	6.0	6.1
	10.1	10.1	10.0	10.0	9.7

Standard	Standard	Standard	Standard	Standard
WHOI durango				
40.90	41.99	41.07	40.99	41.06
54.67	54.21	54.90	54.76	55.60
0.07	0.07	0.07	0.07	0.07
0.23	0.23	0.23	0.23	0.23
0.50	0.50	0.50	0.50	0.50
0.06	0.06	0.06	0.06	0.06
0.01	0.01	0.01	0.01	0.01
0.26	0.36	0.29	0.23	0.25
0.00	0.00	0.00	0.00	0.00
0.00	0.00	0.00	0.00	0.00
0.34	0.34	0.34	0.34	0.34
3.07	3.22	2.76	2.94	2.95
0.42	0.29	0.45	0.37	0.36
100.53	101.28	100.68	100.50	101.43
-1.39	-1.42	-1.26	-1.32	-1.32
99.14	99.86	99.42	99.18	100.10
WHOI durango				
5.887	5.962	5.885	5.892	5.859
9.959	9.742	9.956	9.962	10.040
0.007	0.007	0.007	0.007	0.007
0.076	0.075	0.075	0.076	0.075
0.031	0.031	0.031	0.031	0.031
0.008	0.008	0.008	0.008	0.008
0.003	0.003	0.003	0.003	0.003
0.034	0.045	0.037	0.029	0.031
0.000	0.000	0.000	0.000	0.000
0.000	0.000	0.000	0.000	0.000
0.058	0.057	0.058	0.058	0.057
1.651	1.708	1.478	1.581	1.571
0.120	0.083	0.129	0.106	0.103
1.771	1.791	1.607	1.687	1.674
16.062	15.928	16.059	16.064	16.111
0.229	0.209	0.393	0.313	0.326
0.38	0.35	0.66	0.52	0.55
99.53	100.21	100.08	99.70	100.65
6.0	6.1	6.0	6.0	5.9
10.0	9.8	10.0	10.0	10.1

Standard	Standard	Standard	Standard	Standard
WHOI durango	WHOI durango	WHOI durango	WHOI wilberforce	WHOI wilberforce
40.58	41.55	41.27	39.97	40.71
55.09	53.47	53.94 0.07	54.48	53.98
0.07	0.07 0.23		0.46	0.46
0.23		0.23	0.24	0.24
0.50	0.50	0.50	0.32	0.32
0.06	0.06	0.06	0.05	0.05
0.01	0.01	0.01	0.01	0.01
0.24	0.27	0.19	0.47	0.50
0.00	0.00	0.00	0.05	0.05
0.00	0.00	0.00	0.00	0.00
0.34	0.34	0.34	0.13	0.13
3.23	3.22	3.15	3.61	3.62
0.39	0.44	0.32	0.00	0.00
100.74	100.16	100.08	99.79	100.07
-1.45	-1.46	-1.40	-1.52	-1.52
99.29	98.71	98.68	98.27	98.55
WHOI durango	WHOI durango	WHOI durango	WHOI wilberforce	WHOI wilberforce
5.853	5.977	5.947	5.831	5.894
10.056	9.734	9.838	10.059	9.892
0.007	0.007	0.007	0.046	0.046
0.076	0.076	0.076	0.080	0.080
0.031	0.031	0.031	0.020	0.020
0.008	0.008	0.008	0.006	0.006
0.003	0.003	0.003	0.003	0.003
0.030	0.035	0.024	0.061	0.064
0.000	0.000	0.000	0.005	0.005
0.000	0.000	0.000	0.000	0.000
0.058	0.058	0.058	0.022	0.022
1.740	1.730	1.696	1.967	1.958
0.113	0.127	0.093	0.000	0.000
1.853	1.858	1.789	1.967	1.958
16.121	15.927	15.991	16.133	16.032
0.147	0.142	0.211	0.033	0.042
0.24	0.24	0.35	0.05	0.07
99.53	98.94	99.03	98.33	98.62
5.9	6.1	6.0	5.9	6.0
10.1	9.8	9.9	10.1	10.0

Standard	Standard	Standard	Standard	Standard
WHOI wilberforce				
40.20	40.09	40.42	40.10	40.82
53.87	54.28	54.24	54.10	54.33
0.46	0.46	0.46	0.46	0.46
0.24	0.24	0.24	0.24	0.24
0.32	0.32	0.32	0.32	0.32
0.05	0.05	0.05	0.05	0.05
0.01	0.01	0.01	0.01	0.01
0.56	0.61	0.70	0.54	0.67
0.05	0.05	0.05	0.05	0.05
0.00	0.00	0.00	0.00	0.00
0.13	0.13	0.13	0.13	0.13
3.73	3.72	3.37	3.48	3.80
0.00	0.00	0.00	0.00	0.00
99.62	99.96	99.99	99.48	100.88
-1.57	-1.57	-1.42	-1.47	-1.60
98.05	98.39	98.57	98.01	99.28
WHOI wilberforce				
5.863	5.834	5.848	5.850	5.870
9.944	9.998	9.932	9.988	9.888
0.046	0.046	0.046	0.046	0.045
0.080	0.080	0.080	0.080	0.079
0.020	0.020	0.020	0.020	0.020
0.006	0.006	0.006	0.006	0.006
0.003	0.003	0.003	0.003	0.003
0.072	0.079	0.089	0.069	0.086
0.005	0.005	0.005	0.005	0.005
0.000	0.000	0.000	0.000	0.000
0.022	0.022	0.022	0.022	0.022
2.032	2.022	1.821	1.896	2.041
0.000	0.000	0.000	0.000	0.000
2.032	2.022	1.821	1.896	2.041
16.062	16.093	16.051	16.089	16.025
0.000	0.000	0.179	0.104	0.000
0.00	0.00	0.30	0.17	0.00
98.05	98.39	98.86	98.18	99.28
6.0	5.9	6.0	5.9	6.0
10.0	10.1	10.0	10.1	10.0

Standard	Standard	Standard	Standard	Standard
WHOI wilberforce				
41.29	40.44	40.39	40.71	40.48
55.85	54.52	55.05	54.12	54.42
0.46	0.46	0.46	0.46	0.46
0.24	0.24	0.24	0.24	0.24
0.32	0.32	0.32	0.32	0.32
0.05	0.05	0.05	0.05	0.05
0.01	0.01	0.01	0.01	0.01
0.63	0.68	0.47	0.46	0.55
0.05	0.05	0.05	0.05	0.05
0.00	0.00	0.00	0.00	0.00
0.13	0.13	0.13	0.13	0.13
3.38	3.48	3.48	3.51	3.54
0.00	0.00	0.00	0.00	0.00
102.41	100.38	100.65	100.06	100.25
-1.42	-1.47	-1.47	-1.48	-1.49
100.99	98.91	99.18	98.58	98.76
WHOI wilberforce				
5.838	5.839	5.833	5.892	5.858
9.993	9.963	10.061	9.913	9.966
0.045	0.045	0.045	0.046	0.046
0.078	0.079	0.079	0.080	0.080
0.020	0.020	0.020	0.020	0.020
0.006	0.006	0.006	0.006	0.006
0.002	0.003	0.003	0.003	0.003
0.079	0.087	0.060	0.059	0.070
0.004	0.005	0.005	0.005	0.005
0.000	0.000	0.000	0.000	0.000
0.022	0.022	0.022	0.022	0.022
1.785	1.877	1.877	1.898	1.913
0.000	0.000	0.000	0.000	0.000
1.785	1.877	1.877	1.898	1.913
16.087	16.070	16.134	16.046	16.075
0.215	0.123	0.123	0.102	0.087
0.36	0.20	0.20	0.17	0.14
101.35	99.12	99.38	98.75	98.90
5.9	5.9	5.9	6.0	6.0
10.1	10.0	10.1	10.0	10.0

Standard	Standard	Standard	Standard	Standard
WHOI wilberforce				
40.15	39.86	41.46	41.52	40.51
55.08	54.82	55.47	54.85	55.43
0.46	0.46	0.46	0.46	0.46
0.24	0.24	0.24	0.24	0.24
0.32	0.32	0.32	0.32	0.32
0.05	0.05	0.05	0.05	0.05
0.01	0.01	0.01	0.01	0.01
0.73	0.61	0.69	0.44	0.55
0.05	0.05	0.05	0.05	0.05
0.00	0.00	0.00	0.00	0.00
0.13	0.13	0.13	0.13	0.13
3.68	3.58	3.37	3.32	3.75
0.00	0.00	0.00	0.00	0.00
100.90	100.13	102.25	101.39	101.50
-1.55	-1.51	-1.42	-1.40	-1.58
99.35	98.62	100.83	99.99	99.92
WHOI wilberforce				
5.794	5.797	5.859	5.910	5.816
10.059	10.091	9.921	9.882	10.072
0.045	0.046	0.045	0.045	0.045
0.079	0.080	0.078	0.078	0.079
0.020	0.020	0.020	0.020	0.020
0.006	0.006	0.006	0.006	0.006
0.003	0.003	0.002	0.003	0.003
0.093	0.079	0.086	0.055	0.070
0.005	0.005	0.004	0.004	0.005
0.000	0.000	0.000	0.000	0.000
0.022	0.022	0.022	0.022	0.022
1.984	1.945	1.779	1.765	2.011
0.000	0.000	0.000	0.000	0.000
1.984	1.945	1.779	1.765	2.011
16.126	16.149	16.042	16.026	16.138
0.016	0.055	0.221	0.235	0.000
0.03	0.09	0.37	0.39	0.00
99.37	98.71	101.20	100.39	99.92
5.9	5.9	6.0	6.0	5.9
10.1	10.2	10.0	10.0	10.1

Standard	Standard	Standard	Standard	Standard
WHOI wilberforce				
40.48	41.49	40.28	41.13	39.97
53.57	54.59	54.26	54.43	54.16
0.46	0.46	0.46	0.46	0.46
0.24	0.24	0.24	0.24	0.24
0.32	0.32	0.32	0.32	0.32
0.05	0.05	0.05	0.05	0.05
0.01	0.01	0.01	0.01	0.01
0.74	0.67	0.55	0.50	0.59
0.05	0.05	0.05	0.05	0.05
0.00	0.00	0.00	0.00	0.00
0.13	0.13	0.13	0.13	0.13
3.49	3.49	3.84	3.22	3.64
0.00	0.00	0.00	0.00	0.00
99.54	101.50	100.19	100.54	99.62
-1.47	-1.47	-1.62	-1.36	-1.53
98.07	100.03	98.58	99.18	98.09
WHOI wilberforce				
5.876	5.899	5.852	5.900	5.834
9.842	9.823	9.977	9.882	10.005
0.046	0.045	0.046	0.045	0.046
0.080	0.078	0.080	0.079	0.080
0.020	0.020	0.020	0.020	0.020
0.006	0.006	0.006	0.006	0.006
0.003	0.003	0.003	0.003	0.003
0.096	0.084	0.071	0.063	0.077
0.005	0.004	0.005	0.005	0.005
0.000	0.000	0.000	0.000	0.000
0.022	0.022	0.022	0.022	0.022
1.893	1.854	2.084	1.725	1.985
0.000	0.000	0.000	0.000	0.000
1.893	1.854	2.084	1.725	1.985
15.996	15.985	16.082	16.025	16.098
0.107	0.146	0.000	0.275	0.015
0.18	0.25	0.00	0.46	0.03
98.25	100.28	98.58	99.64	98.12
6.0	6.0	5.9	6.0	5.9
9.9	9.9	10.0	10.0	10.1

Standard	Standard	Standard	Standard	Standard
WHOI wilberforce				
40.42	40.67	40.05	40.45	41.23
54.77	54.96	54.92	54.90	54.44
0.46	0.46	0.46	0.46	0.46
0.24	0.24	0.24	0.24	0.24
0.32	0.32	0.32	0.32	0.32
0.05	0.05	0.05	0.05	0.05
0.01	0.01	0.01	0.01	0.01
0.64	0.48	0.50	0.50	0.73
0.05	0.05	0.05	0.05	0.05
0.00	0.00	0.00	0.00	0.00
0.13	0.13	0.13	0.13	0.13
3.38	3.76	3.62	3.45	3.45
0.00	0.00	0.00	0.00	0.00
100.47	101.13	100.35	100.56	101.11
-1.42	-1.58	-1.52	-1.45	-1.45
99.05	99.55	98.83	99.11	99.66
WHOI wilberforce				
5.831	5.852	5.814	5.840	5.885
9.999	10.008	10.091	10.031	9.834
0.045	0.045	0.046	0.045	0.045
0.079	0.079	0.080	0.079	0.078
0.020	0.020	0.020	0.020	0.020
0.006	0.006	0.006	0.006	0.006
0.003	0.003	0.003	0.003	0.003
0.082	0.062	0.065	0.064	0.093
0.005	0.005	0.005	0.005	0.004
0.000	0.000	0.000	0.000	0.000
0.022	0.022	0.022	0.022	0.022
1.821	2.021	1.963	1.860	1.839
0.000	0.000	0.000	0.000	0.000
1.821	2.021	1.963	1.860	1.839
16.092	16.101	16.151	16.115	15.990
0.179	0.000	0.037	0.140	0.161
0.30	0.00	0.06	0.23	0.27
99.34	99.55	98.89	99.34	99.93
5.9	5.9	5.9	5.9	6.0
10.1	10.1	10.2	10.1	9.9

Standard	Standard	Standard	Standard	Standard
WHOI wilberforce				
41.37	41.04	39.97	40.85	40.29
54.97	54.50	54.23	53.30	54.77
0.46	0.46	0.46	0.46	0.46
0.24	0.24	0.24	0.24	0.24
0.32	0.32	0.32	0.32	0.32
0.05	0.05	0.05	0.05	0.05
0.01	0.01	0.01	0.01	0.01
0.56	0.52	0.44	0.53	0.47
0.05	0.05	0.05	0.05	0.05
0.00	0.00	0.00	0.00	0.00
0.13	0.13	0.13	0.13	0.13
3.81	3.58	3.67	3.69	3.56
0.00	0.00	0.00	0.00	0.00
101.97	100.90	99.57	99.63	100.35
-1.60	-1.51	-1.55	-1.55	-1.50
100.36	99.39	98.03	98.08	98.85
WHOI wilberforce				
5.886	5.890	5.844	5.930	5.838
9.898	9.899	10.036	9.792	10.045
0.045	0.045	0.046	0.046	0.046
0.078	0.079	0.080	0.080	0.080
0.020	0.020	0.020	0.020	0.020
0.006	0.006	0.006	0.006	0.006
0.003	0.003	0.003	0.003	0.003
0.070	0.066	0.057	0.068	0.060
0.004	0.005	0.005	0.005	0.005
0.000	0.000	0.000	0.000	0.000
0.022	0.022	0.022	0.022	0.022
2.025	1.919	2.005	2.001	1.927
0.000	0.000	0.000	0.000	0.000
2.025	1.919	2.005	2.001	1.927
16.032	16.035	16.120	15.971	16.124
0.000	0.081	0.000	0.000	0.073
0.00	0.13	0.00	0.00	0.12
100.36	99.53	98.03	98.08	98.97
6.0	6.0	5.9	6.0	5.9
10.0	10.0	10.1	9.9	10.1

Standard	Standard	Standard	Standard	Standard
WHOI wilberforce				
40.39	39.90	39.95	40.28	41.65
53.85	54.32	54.43	54.24	54.60
0.46	0.46	0.46	0.46	0.46
0.24	0.24	0.24	0.24	0.24
0.32	0.32	0.32	0.32	0.32
0.05	0.05	0.05	0.05	0.05
0.01	0.01	0.01	0.01	0.01
0.68	0.70	0.59	0.52	0.66
0.05	0.05	0.05	0.05	0.05
0.00	0.00	0.00	0.00	0.00
0.13	0.13	0.13	0.13	0.13
3.18	3.76	3.62	3.77	3.64
0.00	0.00	0.00	0.00	0.00
99.36	99.94	99.85	100.07	101.81
-1.34	-1.58	-1.52	-1.59	-1.53
98.02	98.36	98.33	98.48	100.28
WHOI wilberforce				
5.865	5.813	5.821	5.856	5.908
9.897	10.016	10.037	9.980	9.803
0.046	0.046	0.046	0.046	0.045
0.080	0.080	0.080	0.080	0.078
0.020	0.020	0.020	0.020	0.020
0.006	0.006	0.006	0.006	0.006
0.003	0.003	0.003	0.003	0.002
0.087	0.091	0.077	0.067	0.084
0.005	0.005	0.005	0.005	0.004
0.000	0.000	0.000	0.000	0.000
0.022	0.022	0.022	0.022	0.022
1.725	2.046	1.970	2.047	1.929
0.000	0.000	0.000	0.000	0.000
1.725	2.046	1.970	2.047	1.929
16.030	16.101	16.117	16.084	15.972
0.275	0.000	0.030	0.000	0.071
0.45	0.00	0.05	0.00	0.12
98.47	98.36	98.38	98.48	100.40
6.0	5.9	5.9	5.9	6.0
10.0	10.1	10.1	10.1	9.9
	-	-	-	-

Standard	Standard	Standard	Standard	Standard
WHOI wilberforce				
40.50	40.01	41.12	41.41	40.48
55.23	55.21	54.15	54.57	54.81
0.46	0.46	0.46	0.46	0.46
0.24	0.24	0.24	0.24	0.24
0.32	0.32	0.32	0.32	0.32
0.05	0.05	0.05	0.05	0.05
0.01	0.01	0.01	0.01	0.01
0.69	0.71	0.54	0.46	0.62
0.05	0.05	0.05	0.05	0.05
0.00	0.00	0.00	0.00	0.00
0.13	0.13	0.13	0.13	0.13
3.76	3.42	3.57	3.74	3.59
0.00	0.00	0.00	0.00	0.00
101.44	100.61	100.64	101.44	100.76
-1.58	-1.44	-1.50	-1.57	-1.51
99.85	99.17	99.14	99.87	99.24
WHOI wilberforce				
5.812	5.781	5.908	5.914	5.835
10.031	10.096	9.846	9.863	9.999
0.045	0.046	0.045	0.045	0.045
0.079	0.079	0.079	0.078	0.079
0.020	0.020	0.020	0.020	0.020
0.006	0.006	0.006	0.006	0.006
0.003	0.003	0.003	0.003	0.003
0.087	0.091	0.069	0.058	0.079
0.005	0.005	0.005	0.004	0.005
0.000	0.000	0.000	0.000	0.000
0.022	0.022	0.022	0.022	0.022
2.016	1.846	1.916	1.995	1.933
0.000	0.000	0.000	0.000	0.000
2.016	1.846	1.916	1.995	1.933
16.110	16.149	16.002	16.014	16.092
0.000	0.154	0.084	0.005	0.067
0.00	0.26	0.14	0.01	0.11
99.85	99.42	99.28	99.87	99.36
5.9	5.9	6.0	6.0	5.9
10.1	10.2	9.9	9.9	10.1
10.1	10.2	٠.5	٠. ٠	10.1

Standard	Standard	Standard	Standard	Standard
WHOI wilberforce				
39.74	41.07	40.61	41.22	40.62
54.45	54.02	54.91	55.27	55.27
0.46	0.46	0.46	0.46	0.46
0.24	0.24	0.24	0.24	0.24
0.32	0.32	0.32	0.32	0.32
0.05	0.05	0.05	0.05	0.05
0.01	0.01	0.01	0.01	0.01
0.45	0.75	0.48	0.50	0.59
0.05	0.05	0.05	0.05	0.05
0.00	0.00	0.00	0.00	0.00
0.13	0.13	0.13	0.13	0.13
3.72	3.55	3.71	3.22	3.85
0.00	0.00	0.00	0.00	0.00
99.62	100.65	100.97	101.47	101.59
-1.57	-1.49	-1.56	-1.36	-1.62
98.06	99.16	99.41	100.11	99.97
WHOI wilberforce				
5.820	5.892	5.850	5.870	5.826
10.092	9.807	10.011	9.961	10.032
0.046	0.045	0.045	0.045	0.045
0.080	0.079	0.079	0.078	0.079
0.020	0.020	0.020	0.020	0.020
0.007	0.006	0.006	0.006	0.006
0.003	0.003	0.003	0.003	0.003
0.059	0.095	0.062	0.063	0.076
0.005	0.005	0.005	0.004	0.005
0.000	0.000	0.000	0.000	0.000
0.022	0.022	0.022	0.022	0.022
2.035	1.902	1.996	1.713	2.063
0.000	0.000	0.000	0.000	0.000
2.035	1.902	1.996	1.713	2.063
16.154	15.974	16.103	16.072	16.113
0.000	0.098	0.004	0.287	0.000
0.00	0.16	0.01	0.48	0.00
98.06	99.32	99.42	100.59	99.97
5.9	6.0	5.9	6.0	5.9
10.2	9.9	10.1	10.0	10.1

Standard	Standard	Standard	Standard	Standard
WHOI wilberforce				
40.80	40.75	41.24	40.56	40.62
54.45	53.63	54.12	54.34	55.22
0.46	0.46	0.46	0.46	0.46
0.24	0.24	0.24	0.24	0.24
0.32	0.32	0.32	0.32	0.32
0.05	0.05	0.05	0.05	0.05
0.01	0.01	0.01	0.01	0.01
0.59	0.52	0.59	0.55	0.58
0.05	0.05	0.05	0.05	0.05
0.00	0.00	0.00	0.00	0.00
0.13	0.13	0.13	0.13	0.13
3.86	3.53	3.24	3.45	3.73
0.00	0.00	0.00	0.00	0.00
100.96	99.69	100.45	100.16	101.41
-1.63	-1.49	-1.36	-1.45	-1.57
99.34	98.21	99.09	98.70	99.84
WHOI wilberforce				
5.871	5.910	5.911	5.866	5.829
9.917	9.844	9.818	9.946	10.029
0.045	0.046	0.045	0.046	0.045
0.079	0.080	0.079	0.079	0.079
0.020	0.020	0.020	0.020	0.020
0.006	0.006	0.006	0.006	0.006
0.003	0.003	0.003	0.003	0.003
0.076	0.067	0.075	0.070	0.073
0.005	0.005	0.005	0.005	0.005
0.000	0.000	0.000	0.000	0.000
0.022	0.022	0.022	0.022	0.022
2.075	1.912	1.735	1.864	2.000
0.000	0.000	0.000	0.000	0.000
2.075	1.912	1.735	1.864	2.000
16.044	16.002	15.984	16.063	16.111
0.000	0.088	0.265	0.136	0.000
0.00	0.14	0.44	0.23	0.00
99.34	98.35	99.53	98.93	99.84
6.0	6.0	6.0	6.0	5.9
10.0	9.9	9.9	10.0	10.1

WHOI wilberforce WHOI wilberforce WHOI wilberforce WHOI wilberforce WHOI wilberforce 41.72 40.70 40.35 40.88 40.69 54.93 55.43 55.50 55.12 55.02 0.46 0.46 0.46 0.46 0.46 0.24 0.24 0.24 0.24 0.24 0.32 0.32 0.32 0.32 0.32 0.05 0.05 0.05 0.05 0.05
54.93 55.43 55.50 55.12 55.02 0.46 0.46 0.46 0.46 0.46 0.24 0.24 0.24 0.24 0.24 0.32 0.32 0.32 0.32 0.32 0.05 0.05 0.05 0.05 0.05
0.46 0.46 0.46 0.46 0.46 0.24 0.24 0.24 0.24 0.24 0.32 0.32 0.32 0.32 0.32 0.05 0.05 0.05 0.05 0.05
0.24 0.24 0.24 0.24 0.24 0.32 0.32 0.32 0.32 0.32 0.05 0.05 0.05 0.05 0.05
0.32 0.32 0.32 0.32 0.32 0.05 0.05 0.05 0.05
0.05 0.05 0.05 0.05
0.01 0.01 0.01 0.01
0.53
0.05 0.05 0.05 0.05
0.00 0.00 0.00 0.00 0.00
0.13
3.48 3.32 3.68 3.90 3.77
0.00 0.00 0.00 0.00
101.92 101.24 101.52 101.77 101.42
-1.47 -1.40 -1.55 -1.64 -1.59
100.46 99.84 99.97 100.13 99.83
WHOI wilberforce WHOI wilberforce WHOI wilberforce WHOI wilberforce
5.910 5.829 5.788 5.846 5.833
9.849 10.048 10.075 9.976 9.982
0.045 0.045 0.045 0.045 0.045
0.078 0.079 0.079 0.079 0.079
0.020 0.020 0.020 0.020 0.020
0.006 0.006 0.006 0.006 0.006
0.002 0.003 0.003 0.003 0.003
0.067 0.067 0.093 0.077 0.086
0.004 0.005 0.005 0.004 0.005
$0.000 \qquad 0.000 \qquad 0.000 \qquad 0.000 \qquad 0.000$
0.022 0.022 0.022 0.022 0.022
1.842 1.776 1.972 2.083 2.019
$0.000 \qquad 0.000 \qquad 0.000 \qquad 0.000 \qquad 0.000$
1.842 1.776 1.972 2.083 2.019
16.003 16.123 16.135 16.078 16.080
0.158
0.27 0.37 0.05 0.00 0.00
100.72 100.22 100.02 100.13 99.83
6.0 5.9 5.9 5.9 5.9
9.9 10.1 10.1 10.0 10.1